Development of a One-Dimensional Code for the Initial Design of a Micro Gas Turbine Compressor Stage

by
Hano van Eck

Thesis presented in partial fulfilment of the requirements for the degree of Master of Engineering (Mechanical) in the Faculty of Engineering at Stellenbosch University

Supervisor: Prof S.J. van der Spuy
Co-supervisor: Prof T.W. von Backström

December 2020

Declaration

By submitting this thesis electronically, I declare that the entirety of the work contained therein is my own, original work, that I am the sole author thereof (save to the extent explicitly otherwise stated), that reproduction and publication thereof by Stellenbosch University will not infringe any third party rights and that I have not previously in its entirety or in part submitted it for obtaining any qualification.

Date: …………………………..

Abstract

Development of a One-Dimensional Code for the Initial Design of a Micro Gas Turbine Compressor Stage

H. van Eck

Department of Mechanical and Mechatronic Engineering,

University of Stellenbosch,

Private Bag X1, Matieland 7602, South Africa.

Thesis: MEng (Mech)

December 2020

The use of micro gas turbines for once-off and often unique applications means that a generic, rapid turnaround design and performance evaluation process is required. This thesis aims at developing an application based One Dimensional (1D) design and flow analysis program to be used as an initial design tool for radial and mixed flow compressors. The application was developed in MATLAB®. The code is primarily based on the mean line flow and loss models developed by Aungier (2000). For verification, 18 test compressors were developed using the 1D Application (App). These test compressors cover a wide range of design velocities, mass flow rates, as well as meridional exit angles (mixed flow compressors). Predicted performance results were validated using Numeca/FINE™ Turbo software. Initial comparisons between 1D and CFD results did not match very well. The 1D software generally over-predicted compressor performance, i.e. total-to-total efficiency and pressure ratio. The 1D software further provided fairly poor compressor choke prediction. Consequently, empirical models to correct these deviations were derived and implemented into the 1D software. Following these corrections, the results predicted by the modified 1D application compared well with the CFD results obtained. Initial 1D mean line results presented a mean choke prediction difference of 14.98% for the 18 test compressors, with a maximum difference of 39.88%. In the updated 1D App code the mean difference was reduced to 1.59% with a maximum difference of 4.97%. Initial 1D mean line results presented a mean total-to-total pressure ratio prediction difference of 9.31%, with a maximum difference of 17.27%. In the updated 1D App code the mean difference was reduced to 1.24% with a maximum difference of 5.01%. Total-to-total efficiency predicted by the initial 1D mean line code presented a mean difference of 11.23%, with a maximum difference of 15.09%. In the updated 1D App code the mean difference was reduced to 0.74% with a maximum difference of 1.57%. As a final means of validation, two more test compressors were designed using the 1D App. Performance results compared well with the CFD results.

Keywords: micro gas turbine, mixed-flow impeller, crossover diffuser, 1D mean line code, 1D App.

Uittreksel

Ontwikkeling van 'n Een Dimensionele Kode vir die Aanvanklike Ontwerp van 'n Mikro Gasturbine Kompressor Stadium

("Development of a One-Dimensional Code for the Initial Design of a Micro Gas Turbine Compressor Stage")

H. van Eck

Departement Meganiese en Megatroniese Ingenieurswese,

Universiteit van Stellenbosch,

Privaatsak X1, Matieland 7602, Suid Afrika.

Tesis: MIng (Meg)

Desember 2020

Die eenmalige en soms unieke gebruik en aanwending van mikro gasturbine enjins vereis dikwels 'n generiese en spoedige ontwerps en werkverrigting evaluasie proses. Hierdie tesis beoog om 'n toepassings gebaseerde Een Dimensionele (1D) ontwerps en vloei analise kode te ontwikkel wat sal dien as 'n aanvanklike hulpmiddel vir die ontwerp van radiale en gemengde vloei kompressors. Die toepassing is in MATLAB® ontwikkel. Die kode is primêr gebaseer op Aungier (2000) se 1D vloei en verlies modelle. Die 1D Toepassing (Toep) is gebruik om 18 toets kompressors te ontwerp wat sou dien as bewys van konsep. Hierdie 18 toets kompressors is ontwikkel om 'n wye verskeidenheid ontwerps snelhede, massavloeitempos en meridionale uitlaat hoeke (gemengde vloei kompressors) te dek. Voorspelde resultate is geverifieer deur gebruik te maak van Numeca/FINE™ Turbo. Aanvanklike vergelykings tussen die 1D en Berekenings Vloeimeganika (BVM) resultate het nie goed ooreengestem nie. Die aanvanklike 1D sagteware het die kompressor werkverrigting (totaal-tot-totale isentropiese doeltreffendheid en drukverhouding) oor die algemeen te hoog voorspel. Die aanvanklike 1D sagteware het verder gebrekkige wurging voorspelling verskaf. Daarom is empiriese modelle afgelei om hierdie afwykings te kwantifiseer en korrigeer. Hierdie korreksies is in die 1D Toepassing kode geïmplimenteer. Die opgedateerde 1D Toepassing kode het resultate tot gevolg gehad wat goed ooreengestem het met die BVM resultate. Aanvanklike 1D kode wurgings resultate het 'n gemiddelde afwyking met betrekking tot BVM resultate getoon van 14.98% vir die 18 toets kompressors, met 'n maksimum afwyking van 39.88%. Hierdie afwyking is met die opgedateerde 1D Toepassing verlaag tot 'n gemiddelde van 1.59% met 'n maksimum afwyking van 4.97%. Die aanvanklike 1D kode het verder 'n gemiddelde totaal-tot-totale drukverhouding afwyking getoon van 9.31% met 'n maksimum afwyking van 17.27%. Die opgedateerde 1D Toepassing kode het hiedie afwyking verlaag tot 'n gemiddelde waarde van 1.24% met 'n maksimum verskil van 5.01%. Die aanvanklike 1D kode het 'n gemiddelde totaal-tot-totale isentropiese doeltreffendheid afwyking getoon van 11.23% met 'n maksimum

afwyking van 15.09%. Die opgedateerde 1D Toepassing kode het hierdie afwyking verlaag tot 'n gemiddelde waarde van 0.74% met 'n maksimum verskil van 1.57%. As finale validasie is twee addisionele toets kompressors ontwerp met behulp van die 1D Toepassing. Die werksverrigting resultate van hierdie twee kompressors het goed ooreengestem met die toepaslike BVM resultate.

Sleutelwoorde: mikro gasturbine, gemengde vloei rotor, oorgangsdiffusor, 1D vloei kode, 1D Toepassing.

Acknowledgements

"No man is an island" (John Donne, 1624). My sincere thanks and appreciation go to:

1.   My foremost anchor and compass in life, my Lord and Saviour, Jesus Christ. "Geseënd is die wat weet hoe afhanklik hulle van God is, want aan hulle behoort die koninkryk van die hemel" (Matthew 5:3, Afrikaans Bible 1983).

2.   My voice of reason and best friend. My wife, Ronel. I love you more than anything in life.

3.   My two sons, Johan and Evert. Keep on making me proud. I love you very much.

4.   My supervisors, Prof S.J. van der Spuy and Prof T.W. von Backström. Your professional guidance and inputs made it a pleasant journey and learning process. You are both legends in your own right.

5.   David Krige from Cape Aerospace Technologies for his time and effort in my Numeca/FINE™ Turbo learning process.

6.   Mr Patrick Shoemaker from Numeca International, Nürnberg, for his support and assistance.

7.   The Military Academy and its members for their support and for creating a positive research and learning environment.

Dedication

Manne…

Table of Contents

Page

TABLE OF CONTENTS ix

TABLE OF CONTENTS   x

List of Figures

LIST OF FIGURES xiii

List of Tables

Page

Nomenclature

Abbreviations

App	Application
APU	Auxiliary Power Unit
CFD	Computational Fluid Dynamics
CoG	Centre of Gravity
GTS	Gas Turbine Starter
GUI	Graphical User Interface
ISA	International Standard Atmosphere
MB	Megabyte
MGT	Micro Gas Turbine
NACA	National Advisory Committee for Aeronautics
QN	Quasi Normal
RPM	Revolutions Per Minute
SOW	Stand-off Weapon
UAV	Unmanned Aerial Vehicle
1D	One-dimensional
3D	Three-dimensional

Symbols

A	Area	$[m^2]$
AR	Area ratio	$[-]$
b	Blade height	$[m]$
C	Absolute fluid velocity	$[m/s]$
c	Blade chord length	$[m]$
c_p	Specific heat at constant pressure	$[J/kg \cdot K]$
D_{eq}	Equivalent diffusion factor	$[-]$
DR	Diffusion ratio	$[-]$
g	Gravitational constant	$[m/s^2]$
h	Specific enthalpy	$[kJ/kg]$
I_R	Rothalpy	$[J/kg]$
i	Angle of incidence	$[°]$
K	Impeller lean angle parameter, Diffuser blade camber line parameter	$[-,-]$
L	Length, Blade loading parameter	$[m,-]$
L_B	Blade passage length	$[m]$
$\dot{m}$	Mass flow rate	$[kg/s]$
M	Mach number	$[-]$
N	Rotational velocity	$[RPM]$

p	Pressure	[Pa]
PR	Pressure ratio	$[\,-\,]$
$\dot{Q}$	Rate of heat transfer	[kJ/kg]
R	Gas constant, Radius ratio	$[\text{J/kg·K}, -\,]$
r	Radius	[m]
s	Specific entropy	[J/kg·K]
SM	Stall margin	$[\,-\,]$
T	Temperature	[K]
t	Blade thickness	[m]
U	Blade tangential velocity	[m/s]
u	Specific internal energy	[J/kg]
V	Velocity	[m/s]
v	Specific volume	[m^3/kg]
W	Relative fluid velocity	[m/s]
$\dot{W}$	Work rate (Power)	[W]
Z	Number of blades, Height	$[\,-\,,\text{m}]$
z	Axial length	[m]

Greek Symbols

α	Absolute flow angle from vertical	[°]
α_C	Meridional angle from axial direction	[°]
β	Blade angle from vertical	[°]
β'	Relative flow angle from vertical	[°]
Δ	Difference (delta)	$[\,-\,]$
ϕ_2	Impeller tip flow coefficient	$[\,-\,]$
γ	Specific heat ratio	$[\,-\,]$
ϵ	Deviation of quasi-normal from true normal	[°]
η	Isentropic efficiency, meridional length ratio along camber line	$[\,-\,,-\,]$
ν	Kinematic viscosity	[m^2/s]
μ	Dynamic viscosity	[Pa·s]
κ	Inlet velocity distribution constant	$[\,-\,]$
θ_C	Equivalent diffuser discharge angle	[°]
θ_R	Blade rake angle from vertical	[°]
ρ	Density	[kg/m^3]
σ_s	Slip factor	$[\,-\,]$
τ	Torque	[Nm]
ψ	Alternative flow parameter	$[\,-\,]$
ω	Rotational velocity	[rad/s]
$\overline{\omega}$	Loss coefficient	$[\,-\,]$

ζ Normalised meridional distance .... [−]

Subscripts

$0n$	Total (stagnation) conditions at compressor station (n)
abs	Absolute
B	Blade
$diff$	Diffuser
eff	Effective
FB	Full Blade
h	Hub contour
i	Increment, Incidence condition
$i0$	Off incidence condition
imp	Impeller
m	Meridional
MSL	Mean Streamline
n	Normal
o	Operating point
$pass$	Passage
$pres$	Pressure side
QN	Quasi Normal
r	Radial
ref	Reference value
s	Shroud contour / Stall point
SB	Splitter Blade
SF	Skin Friction
SS	Static-to-Static quantity
suc	Suction side
t	Tangential
th	Throat position
TT	Total-to-Total quantity
U	Tangential velocity component
z	Axial

Superscripts

$^{-}$	Mean value
$+$	Dimensionless wall distance indicator

Compressor Stations

Note: These are typically also used as subscripts.

1	Impeller inlet
2	Impeller outlet, vaneless gap inlet
3	Vaneless gap outlet, diffuser vaned section inlet
4	Diffuser vaned section outlet

Chapter 1:

Introduction

1.1   Background

The Gas Turbine engine has become the de facto powerplant used in the aviation industry today, with only the smaller and lighter general aviation aircraft still utilising reciprocating engines. The majority of aircraft make use of some configuration of the gas turbine engine, be it in the form of a turbojet engine, a low or high bypass turbofan engine or a fixed or free turboprop engine.

In the Radio-Controlled aircraft and Unmanned Aerial Vehicle (UAV) environments (both civilian and military), gas turbines have been making a significant contribution as propulsion systems in the form of Micro Gas Turbine (MGT) engines (Trebunskikh *et al.*, 2012) (Figure 1.1). MGTs are also extensively utilised as Auxiliary Power Systems (APUs) or Gas Turbine Starters (GTSs) on modern fighter and transport aircraft. Additionally, MGTs have wide application in the military aeronautical sector, particularly in the propulsion of UAVs, target drone propulsion systems, as well as long range stand-off weapons (SOWs). Marcellan *et al.* (2016) predicts the extensive future use of UAVs (and MGTs as propulsion systems) in areas of transport, telecommunication, search and rescue and disaster management.

Figure 1.1: Micro Gas Turbine Engine (Cape Aerospace Technologies)

The general configuration and sizing parameters of Gas Turbine engines are determined by their operational envelope, purpose and platform parameters. Axial flow engines in general provide higher mass flow rates with lower per stage

pressure ratios compared to similar radial flow compressor engines (Dixon and Hall, 2014). Axial flow engines also tend to be longer and more slender, while centrifugal engines tend to be shorter and bulkier. Small radial engines typically display higher efficiencies than comparable axial engines. This is due to the short blade chord lengths of small axial compressors resulting in reduced Reynolds numbers and low flow deflection and blade efficiency. For these reasons, radial and mixed flow compressors are generally preferred in MGT engines due to space/size and Centre of Gravity (CoG) restrictions.

A disadvantage of a pure radial flow MGT is its relatively large frontal area. Modern UAVs and Stand-off Weapons (SOWs) require smaller engines with ideally no reduction in power-to-weight ratios. Large frontal areas increase overall drag which affects overall performance. Mixed flow compressor MGTs could typically be utilised to reduce the frontal area of an engine while still meeting the performance requirements of the engine.

1.2   Motivation

With modern military focus moving more and more towards UAVs and SOWs, propulsion systems need to keep abreast with ever changing weapon systems (Harris *et al*., 2003). Design and sizing parameters might vary drastically from one platform to the next, with associated propulsion systems having to be readily available.

In many of these applications (i.e. target drone and SOW propulsion systems) very accurate and finely optimised design principles might not be a requirement, as the platform may require only a once-off use. In many instances platforms also undergo regular structural modifications for specific testing and operational purposes. Such modifications lead to alterations of the basic housing and thus geometric parameters of the propulsion system. In such cases a generic, rapid turnaround design and performance evaluation process is required.

The mean line, one dimensional flow analysis theory, based on the work of Aungier (2000), forms the ideal basis for such a rapid turnaround, first order design and performance evaluation tool. Since 2012, numerous research projects at Stellenbosch University have focused on the development of an in-house 1D MATLAB® based code for exactly this purpose.

De Wet (2012) developed a MATLAB® based 1D mean line code for the purpose of investigating the performance of a centrifugal turbocharger compressor. Van der Merwe (2012) made use of the basic 1D code developed by De Wet (2012) as an initial design tool for the development of a centrifugal impeller for a 200 N MGT engine. De Villiers (2014) designed a centrifugal compressor stage (impeller and diffuser) for an MGT engine. De Villiers (2014) used the 1D code developed by Van der Merwe (2012) as an initial design tool for the impeller. He added an adapted 1D code for the initial design of the diffuser, which was a conventional

radial vaned configuration with a vaneless bend and de-swirler vanes. Burger (2016) designed a crossover diffuser to be matched to the impeller designed by Van der Merwe (2012). This diffuser configuration featured single, continuous vanes aimed at replacing the conventional radial vane, vaneless bend and de-swirler configuration. The advantage of the crossover design was that the sharp, vaneless bend was eliminated, which minimised the typical recirculation pattern that often exist in vaneless bends. Burger (2016) modified the 1D code used by Van der Merwe (2012) and De Villiers (2014) for the initial design of the crossover diffuser. Diener (2016) developed a mixed flow compressor impeller for use in an MGT engine. He attempted to adapt the already available 1D code to do the initial design of the mixed flow impeller. This attempt was however discarded in favour of using the already available software of CFTurbo®. Kock (2017) developed a crossover diffuser to be matched with the mixed flow impeller developed by Diener (2016). He made use of the 1D code developed by Burger (2014) for the initial design of the crossover diffuser.

Although significant effort has been spent on the development of the in-house 1D code, the code in its form towards the end of 2019 presented the following challenges:

    i.   The MATLAB® based 1D code was only available in the form of basic script files, which limited its intuitive use for a new user.

    ii.   The 1D code was developed and modified for very specific design purposes. The code was thus not usable as a generic design tool.

    iii.   Due to the 1D code being used for specific design requirements, it did not provide very good performance predictions across a wide range of compressor designs, rotational velocities and mass flows.

1.3 Objectives and Methodology

This project aimed to develop an application based One-Dimensional (1D) design and flow analysis program (1D App) to be used as an initial design tool for radial and mixed flow compressors used in MGT engines. To overcome the challenges with the in-house code available at the time, the project firstly focused on developing a user-friendly, intuitive Graphical User Interface (GUI) for simple compressor design. This was achieved by utilising the MATLAB® App Designer Environment. This meant that the core of the 1D code developed by the previous research projects could still be used as background functions.

The 1D App developed during this project caters for the initial design of compressors for use in MGT engines. These compressors consist of a centrifugal or mixed flow impeller, with or without splitter blades, and a vaned crossover diffuser. The 1D App does not cater for vaneless or conventional vaned diffusers.

It was tested for mixed flow compressors with a meridional exit angle as low as 60°.

In order to test and evaluate the accuracy of the performance predictions for the compressors designed with the 1D App, Numeca/FINE™ Turbo CFD software was used to conduct 3D flow analyses of these compressors. Results for each compressor were compared to the 1D App performance prediction and the data was used to update the 1D code accordingly.

Based on the above, the scope for the development of the 1D App is summarised as follows:

i.   The development of a user-friendly, intuitive, front-end GUI.

ii.   A baseline impeller design code had to be developed in the form of a function running in support of the front-end GUI.

iii. Code for the generic design of a crossover diffuser was developed in the form of a function running in support of the front-end GUI.

iv.   The previously developed 1D performance prediction code for both the impeller and diffuser was modified to run as core functions in support of the front-end GUI.

v.   The 1D App includes a feature for the creation of a .geomTurbo file to be used by the Numeca/FINE™ Turbo CFD software.

vi.   To evaluate the validity of the 1D App, 18 test compressors, covering as wide a design range as possible, were designed in the 1D App. The predicted performance for each were recorded and a .geomTurbo file for each were produced.

vii. CFD analysis for each of the 18 test compressors was conducted using Numeca/FINE™ Turbo CFD software. A suitable mesh was created in the AutoGrid5™ Environment and the flow analysis for each was conducted in the FINE™/Turbo Environment.

viii. The CFD and 1D results for each of the 18 test compressors were compared at the various stations in the compressor. Results were used to update the function code of the 1D App.

ix.   Once the 1D App code was updated using the results and analysis of the 18 test compressors, an additional 2 compressors were developed as a final verification. CFD analyses of these compressors were also performed and the results compared to the results from the 1D App.

1.4   Thesis Outline

Chapter 2 summarises the Literature Study that was performed. The study focussed on the basic theory of centrifugal impellers and diffusers, specifically crossover diffusers. Chapter 3 describes the development of the 1D App, focussing on the 1D mean line theory forming the basis of the code. The 3D analysis of 18 test compressors using Numeca/FINE™ Turbo CFD software, is described in Chapter 4. The comparison of the results and subsequent modification of the 1D App code forms the crux of Chapter 5, while the final results and discussions are summarised in Chapter 6.

Chapter 2:

Literature Study

2.1   Introduction

The literature study focusses on compressor (impeller and diffuser) theory and includes pure radial (centrifugal) and mixed flow configurations. The literature study is presented in such a manner that it supports the technical content of the 1D App. Users of the 1D App can therefore read the literature study if they require additional information on the theory applied in the App.

2.2   Micro Gas Turbine

A basic Micro Gas Turbine engine consists of three main components, namely the compressor stage, combustion chamber and turbine stage. In the case of centrifugal or mixed flow compressor engines, the compressor stage incorporates both an impeller and diffuser.
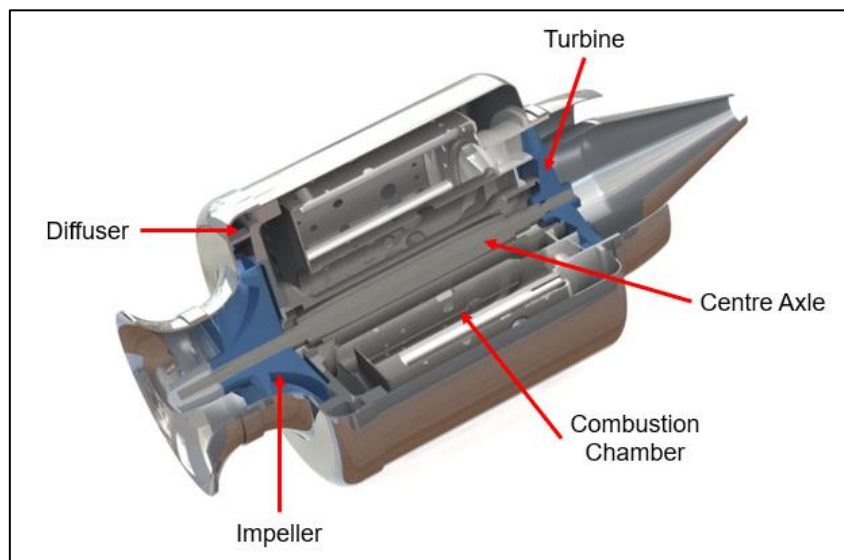
Figure 2.1: Micro Gas Turbine Engine Main Components (Trebunskikh, *et al.*, 2012)

Refer Figure 2.1. The principle of operation of a jet engine is based on the increase in net axial momentum flux (Newton's 2nd law) due to the increase in pressure and temperature of the working fluid and its subsequent acceleration through the exhaust nozzle (Phillips, 2004). Kinetic energy is imparted on the air entering the engine intake through the impeller stage. In the diffuser, this increase in energy and total pressure is diffused, which implies that a large amount of the impeller exit

6

kinetic energy is exchanged for an increase in static pressure. This higher pressure, lower velocity air then enters the combustion chamber of the MGT engine. The addition of heat in the combustion chamber allows for the rapid expansion of the working fluid, which accelerates through the turbine and exhaust nozzle. The high temperature at the turbine inlet enables it to provide the work required by the compressor with a lower pressure drop than the compressor pressure rise. The excess pressure causes a high velocity through the exhaust nozzle by accelerating the flow through a carefully designed exhaust nozzle. This allows for an overall increase in momentum flux of the working fluid, which provides the thrust force generated by the engine.

2.3   Compressors

The compressor supplies compressed air to the combustion chamber. Due to their inherent size constraints, MGTs utilise centrifugal or mixed flow compressors. Mixed flow compressors typically allowed higher mass flow rates, although at the expense of stage pressure ratio (Dixon and Hall, 2014). In both a centrifugal and mixed flow compressor, air enters the impeller axially but exits the impeller perfectly radially (centrifugal compressor) or with a radial and axial component (mixed flow compressor) when viewed meridionally.

2.3.1   Centrifugal Compressor Stage

Air exits the impeller of a centrifugal compressor with a radial and tangential component. The work done by the impeller on the air increases its total pressure and temperature. A radial diffuser is typically matched with a centrifugal impeller. The main purpose of the diffuser is the transfer of kinetic energy to mechanical energy by increasing the static pressure of the fluid in the diffuser (Kock, 2017). Such a diffuser can either be vaned or vaneless, depending on the specific design or size requirements of the engine. Figure 2.2 shows a centrifugal compressor as part of a typical MGT engine (Krige, 2013).

The compressor depicted in Figure 2.2 is a pure radial compressor with no inlet guide vanes. Air enters the impeller axially and is turned through 90° to exit it radially. The impeller is matched with a conventional diffuser. A small vaneless gap exists between the impeller exit and the diffuser radial vanes. Once exiting the radial vaned section of the diffuser, the air is turned axially again through a 90° vaneless bend. The air will still typically display a high tangential velocity component in this region, hence the need for axial de-swirl vanes, as depicted here.
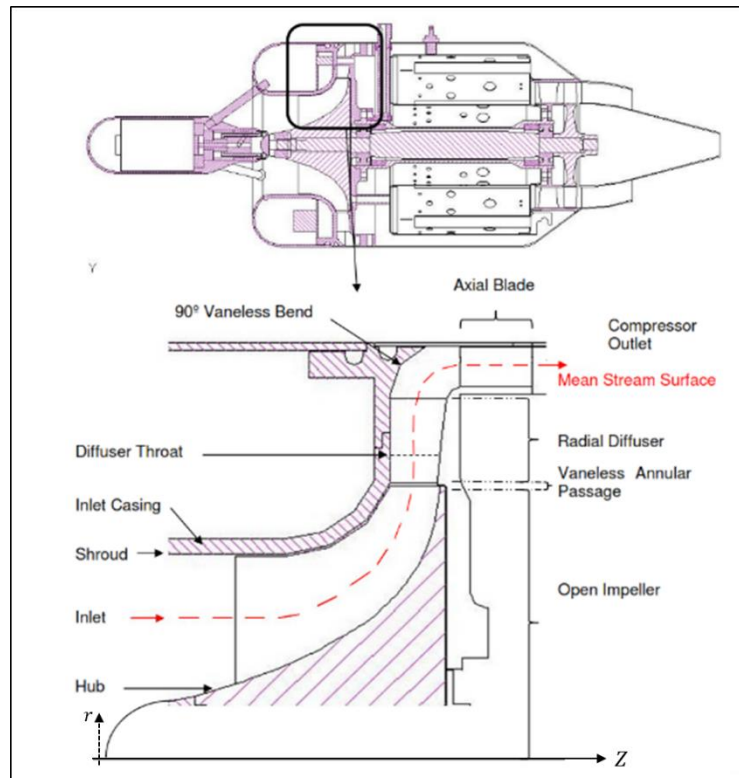
Figure 2.2: Centrifugal Compressor r-Z Plane (Krige, 2013)

2.3.2   Mixed Flow Compressor Stage

Figure 2.3 below indicates the definition of the meridional exit angle (α_{C2}) relative to the r-Z plane of a mixed flow compressor.
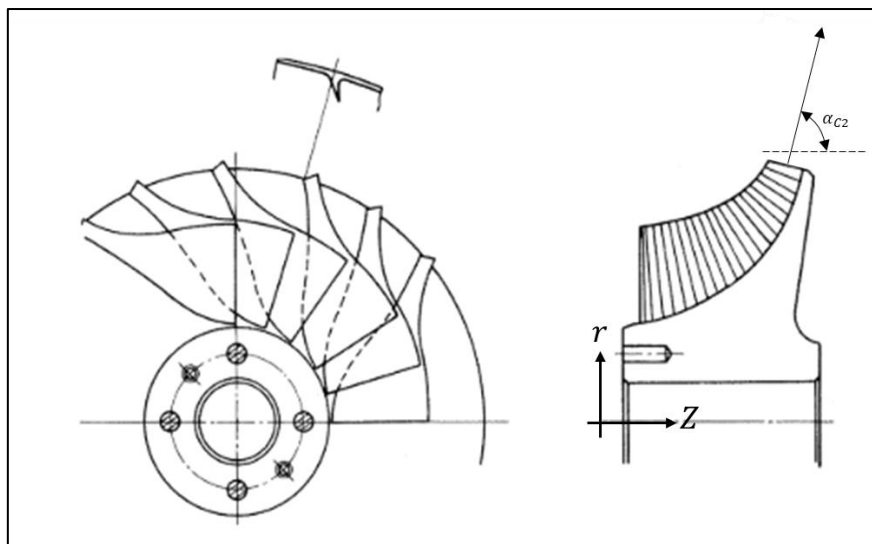
Figure 2.3: Mixed Flow Impeller Meridional View (Adapted from Kano *et al.*, 1984)

A mixed flow compressor can be described as a transition between a centrifugal and an axial flow compressor. The advantages of both configurations can therefore be combined, i.e. higher mass flow rates (axial flow compressors) and higher stage pressure ratios (centrifugal compressors) (Çevik and Uzol, 2011). Mixed flow compressors can handle higher mass flow rates over a wider operating range than comparable centrifugal compressors (Saravanamuttoo *et al.*, 2001). Mixed flow compressors provide the additional advantage of smaller frontal areas while still producing relatively high single stage pressure ratios (Çevik, 2009). The smaller frontal area leads to lower resultant drag values for the platform that is propelled by the gas turbine engine (Goldstein, 1948).

Mixed flow compressors are favoured for use in MGT engines due to their smaller frontal area and higher thrust-to-weight ratio (Rajakumar *et al.*, 2015). Early research into the feasibility of using mixed flow compressors did however highlight various challenges, including structural limitations and diffuser matching problems (Musgrave and Plehn, 1987).

Per definition, mixed flow compressors refer to compressors with meridional impeller exit angles (also referred to as cone angle) between 0° and 90°. Intuitively, the feasibility of a mixed flow compressor below a certain meridional exit angle will be questionable due to a too low stage pressure ratio. This will specifically be applicable if such a compressor is to be used in a single stage configuration, which is typically the case in MGT engines. However, Giri *et al.* (2016) designed a high pressure ratio mixed flow compressor stage with a meridional impeller exit angle of 50°. The higher pressure ratio was achieved by designing the mixed flow impeller with a higher specific speed, compared to that of an equivalent radial impeller. In this case the impeller exit flow was transonic, which led to increased diffuser total pressure losses (Giri *et al.*, 2016). Çevik (2009) optimised the impeller for a mixed flow compressor. His optimum design impeller yielded a meridional exit angle of 50°. He achieved a pressure ratio of 4.34 with an isentropic efficiency of 0.718. The achieved pressure ratio did require a comparably higher rotational speed and resulted in a relative tip Mach number of 1.2.

2.3.3 Compressor Instabilities

To maximise the operating range of a centrifugal compressor stage, it is important to understand and reduce the flow phenomena which can lead to instabilities in a compressor stage. If unchecked, flow instabilities can lead to dramatic performance losses or even engine damage (Dixon and Hall, 2014). Typical compressor flow instabilities include stall, surge and choke.

Stall. Stall in centrifugal compressors can be divided into static and dynamic stall (Japikse, 1996). Static stall is associated with flow separation at stationary locations in the compressor. These can include passage or channel separations in high aerodynamically loaded areas. On the other hand, dynamic (or unsteady) stall is associated with the rotating parts of the compressor, e.g. rotating blade stall.

Japikse and Baines (1997) defined a stability criterion based on the slope of the pressure ratio characteristic between the operating and stall point:

$$\frac{\partial PR}{\partial \dot{m}} = 0 \qquad \text{[Metastable conditions]}$$

$$\frac{\partial PR}{\partial \dot{m}} < 0 \qquad \text{[Stable conditions]} \qquad (2.1)$$

$$\frac{\partial PR}{\partial \dot{m}} > 0 \qquad \text{[Unstable conditions]}$$

with $PR = p_{04}/p_{01}$, which represents the total-to-total pressure ratio between the diffuser exit and impeller inlet points.

Using the following formula, the stall position on the characteristic curve can be determined:

$$SM = \frac{\dot{m}_0 - \dot{m}_s}{\dot{m}_s} \qquad (2.2)$$

where: SM -   Stall Margin.
           $\dot{m}_s$ -   Mass flow rate at stall point.
           $\dot{m}_o$ -   Mass flow rate at operating point.

A larger stall margin (*SM*) therefore allows a compressor to operate over a larger mass flow rate range. In a compressor, the diffuser (vaned diffuser) is particularly prone to stall (Dixon, 1998). Any flow diversion that leads to an excessive incidence flow angle onto the diffuser vane leading edge can lead to a stall situation. Halawa *et al.* (2015) investigated the injection of air close to the diffuser blade leading edge on the shroud side as a means of controlling the stall in the diffuser at various mass flow rates. Good results were observed, especially with higher injection mass flow rates.

Surge

Another form of compressor instability to consider is surge. Dixon and Hall (2014) explains surge by means of the following theoretical curve.
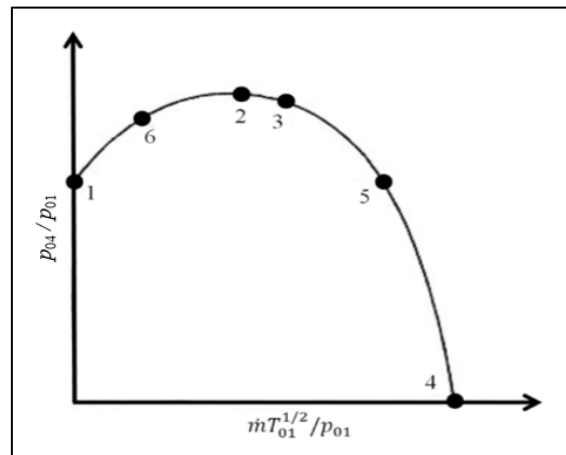
Figure 2.4: Compressor Characteristic Curve (Adapted from Dixon and Hall, 2014)

This theoretical curve would be obtained by controlling the mass flow through a compressor by means of a valve downstream of the compressor assembly. The total-to-total pressure ratio between the diffuser outlet and impeller inlet is used as the vertical axis parameter, while a mass flow parameter is used on the horizontal axis. With the valve closed (at point 1), no flow is established, and a specific, datum pressure ratio is present. As the valve is slowly opened, the mass flow increases with an associated increase in the pressure ratio up to a maximum pressure ratio at point 2. A further increase in mass flow result in a slight pressure ratio drop, but an increase in efficiency up to point 3 where maximum efficiency is reached. This would typically be the design operating point of the compressor. A further increase in mass flow result in a further decrease of the pressure ratio, eventually reaching a value of zero (point 4), which corresponds with a condition where all the input power is used to overcome friction. This is however a theoretical value, as choke conditions will be reached at around point 5 on the curve. No further increase in mass flow rate will therefore be possible past point 5.

With the compressor operating on the negative slope side of the characteristic curve (around point 3), typical stable operating conditions will be experienced. For example: A slight decrease in mass flow will result in a slight increase in pressure ratio being exerted on the system, which in turn will lead to an increase in the mass flow back to point 3. The situation is self-correcting and stable. In the event that the mass flow (for instance due to blockage, mechanical damage, etc.) reduces to point 6, operating on the positive slope side of the curve will lead to unstable conditions. The associated reduction in mass flow at point 6 would have resulted in a reduction in pressure ratio, which in turn will result in a further reduction in mass flow. The mass flow may be reduced to zero or the situation might even lead to a reverse flow situation (Boyce, 2012). Depending on the shape of the system curve, a further reduction in pressure ratio might lead to positive flow being established again, but only until the restricted mass flow is reached, after which the process will be repeated. This positive and negative flow through the

compressor is referred to as surge. This is an unstable situation and may eventually lead to mechanical damage.

Rotating Stall

Japikse (1996) states that rotating stall can be induced by destabilised impeller or diffuser flow (vector quantity imbalance) or by unsteady interaction between the impeller and diffuser. In the event of, for example, a partial blockage in the diffuser, the upstream blade in that vicinity may stall. A stalled blade has the effect of increasing the angle of incidence on the following blade and decreasing the angle of incidence on the preceding blade. This will result in the following blade stalling when reaching the point of disturbance, with the situation repeating itself. The stall thus propagates in the opposite direction of rotation, having the effect that the stalled region remains in a specific area relative to the fixed casing, but moves approximately at the speed of rotation relative to the rotating blades (Boyce, 1993).

Choke

Choke is a condition where, for given upwind total conditions, the maximum mass flow through the compressor is reached due to the development of sonic conditions in the impeller or diffuser throat. Any further reduction in back pressure will only have the effect of moving the normal shock downstream from the throat, but no increase in mass flow rate can be achieved due to the maximum achievable velocity (sonic) having been reached in the throat (Phillips, 2004).

Figure 2.4 indicates a typical compressor characteristic curve at a specific speed. A compressor map at various speeds is indicated below in Figure 2.5, showing the respective surge and choke regions.
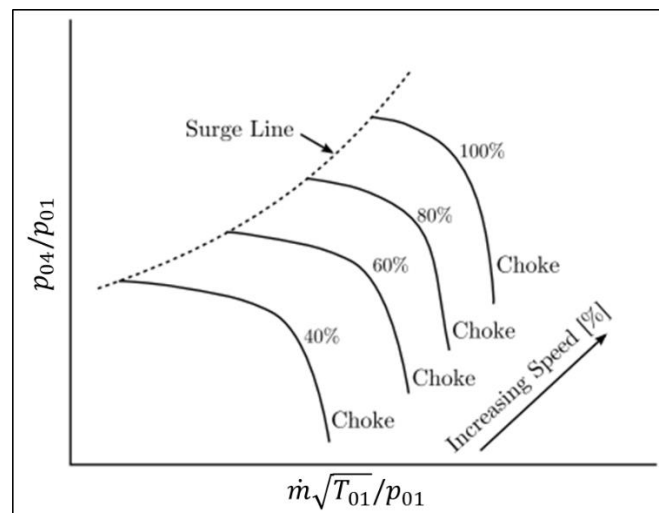
Figure 2.5: Typical Compressor Map (Adapted from Burger, 2016)

2.4　Impeller Theory

As was the case with most fluid flow, flow through an impeller and diffuser is governed by the following fundamental physical laws:

i. Conservation of Mass.
ii. Conservation of Momentum.
iii. Conservation of Energy (1st Law of Thermodynamics).
iv. $dS \geq \int \frac{dQ}{T}$ (2nd Law of Thermodynamics).

2.4.1　Impeller Velocity Triangles

The applicable inlet (1) and outlet (2) velocity components and angles associated with a mixed flow impeller are illustrated in Figure 2.6.

Air entering the inlet could be either purely axial (as illustrated) or pre-whirl can be achieved by adding inlet guide vanes. Pre-whirl has the advantage that the operating mass flow can be altered without noticeable changes in pressure ratio (van der Merwe, 2012). Pre-whirl can also assist in the reduction of the relative inlet velocity for high pressure ratio compressors (Dixon and Hall, 2014). In the case of no inlet guide vanes, air enters the inlet at an absolute velocity of $C_1 = C_{abs}$. At the design point, the magnitude of $C_1 = C_{abs}$ is controlled such that the vector sum of C_1 and U_1 (rotational velocity) results in the relative inlet velocity (W_1) to be closely aligned with the inlet blade angle (β_1). In practice this cannot be achieved across the whole inlet. Reasonable assumptions in this regard are therefore made, for instance that the relative inlet velocity is aligned with the inlet blade angle at the hub and at the shroud. Angles of incidence can then be calculated for the rest of the inlet. Pre-whirl was not further investigated, as the developed 1D App did not cater for this feature.

Because of the work done by the impeller on the working fluid (air) between impeller inlet and outlet, the air experience an increase in total pressure and temperature. The impeller tip speed (U_2) plays a major role in determining the achievable pressure ratio. The tip speed is however limited by structural considerations, as the material stresses typically increase in proportion to the square of the tip speed (Sandberg, 2016).

Figure 2.6: Mixed Flow Impeller Velocity Components (Adapted from Van der Merwe (2012))

Figure 2.6 above illustrates the velocity components present at the inlet (no inlet guide vanes) and exit of a mixed flow impeller. It is important to note that the depicted velocity triangle at the impeller exit (station 2) in Figure 2.6 actually lies in the plane of the meridional velocity (C_{m2}) and not on the vertical plane (refer C_{m2} in both schematics).

2.4.2 Slip and Slip Factor

In a mixed flow impeller, the absolute flow velocity vector (C_2) exiting the impeller (station 2) consists of three components, namely a radial component, a tangential component and an axial component. The axial component is a function of the meridional exit angle (α_{C2}). In an ideal scenario, air will exit the impeller with a relative velocity angle (β_2') equal to the blade exit angle (β_2). In practice however, $\beta_2 < \beta_2'$ due to a phenomenon called slip. From a velocity point-of-view, slip manifests itself as a reduction in the outlet tangential component (C_{U2}) by a magnitude of ΔC_{U2}. In the case of mixed flow impellers, slip is reduced with a reduction in the meridional exit angle due to the reduction in the Coriolis force (Diener, 2016).

For the purpose of predicting impeller performance, a suitable parameter to quantify the effect of slip is the slip factor. The slip factor is defined as:

$$\sigma_s = \frac{C_{U2}}{C_{U2} + \Delta C_{U2}} \qquad (2.3)$$

From Equation 2.9 it is clear that $\sigma_s < 1$. As mentioned earlier, a reduction in meridional exit angle of an impeller will result in a reduction of slip. Applying this to Equation 2.9, it is clear that slip factor will increase with a decrease in meridional exit angle.

The presence of slip also affects the power required to drive the impeller.

$$\dot{W} = \sum \tau \omega = \dot{m}(U_2 C_{U2} - U_1 C_{U1}) \qquad (2.4)$$

Slip has the effect of reducing C_{U2}. Consequently, the energy transferred by the impeller is also reduced. To regain the required pressure rise, the rotational velocity has to be increased, along with an increase in power transferred to the air.

2.4.3 Tip Flow Coefficient

Another dimensionless property which is used to characterise the impeller (or stage) is the tip (or stage) flow coefficient (Aungier, 2000). The tip flow coefficient provides a dimensionless relationship, which includes flow rate, size and speed data. This parameter can be used to compare various stages/impellers with each other.

$$\phi_2 = \frac{\dot{m}}{\rho_2 A_2 U_2} \qquad (2.5)$$

2.4.4 Mollier Diagram and Streamline Relationships

The flow through a compressor stage can be analysed by means of a Mollier diagram (Dixon and Hall, 2014) (Figure 2.7), where the following positions are defined:

    i.   Position 0 – Inlet to inducer section (inlet casing).
    ii.   Position 1 – Inlet to impeller.
    iii.   Position 2 – Impeller exit – vaneless space start.
    iv.   Position 3 – Vaneless space exit – vaned diffuser inlet.
    v.   Position 4 – Diffuser exit.

The whole compressor section encapsulates positions 0 to 4. The static conditions are indicated by the single digit numbered positions 0 to 4 on the Mollier diagram. This path is indicated by the arrows. The total (stagnation) conditions are indicated on the diagram by the double-digit positions (00 to 04) above their associated static positions, the kinetic energy term ($C_n^2/2$) being the difference between these.

The efficiency of the compressor is often expressed in terms of the ideal isentropic process that takes place between the inlet and outlet states. The ideal isentropic process is indicated by the red line on the Mollier diagram. The ideal isentropic conditions are indicated with a 's' suffix.
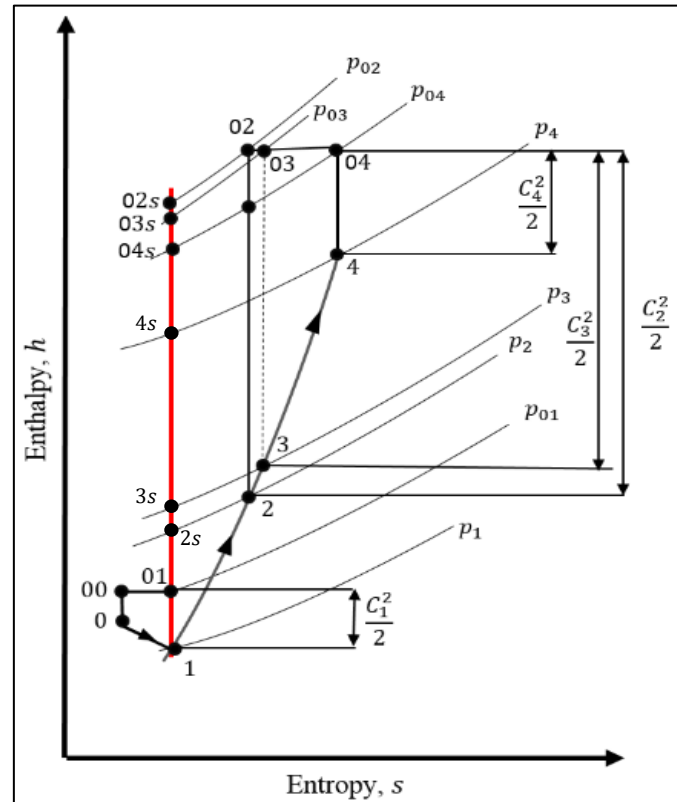
Figure 2.7: Mollier Diagram (Kock, 2017)

The stagnation enthalpy at any position in the compressor can be written as:

$$h_{0n} = h_n + \frac{C_n^2}{2} \tag{2.6}$$

which states that the total (stagnation) enthalpy at any point is equal to the static enthalpy at that point plus the specific kinetic energy at that point.

Since no work is done on the fluid in the inlet casing and assuming adiabatic conditions, negligible friction and negligible change in potential energy, the steady flow energy equation between stations 0 and 1 reduces to:

$$h_{00} = h_{01} \tag{2.7}$$

In the case of the impeller however (between positions 1 and 2), work is done on the fluid in the impeller. If this process is assumed to be adiabatic and with a negligible change in potential energy, then the work rate (power) imparted is:

$$\dot{W} = \dot{m}(h_{02} - h_{01}) \tag{2.8}$$

Equating Equation 2.8 with Equation 2.4 and substituting Equation 2.6, the equation for rothalpy (I_R) is derived:

$$I_R = \ h_1 + \frac{C_1^2}{2} - U_1 C_{U1} = h_2 + \frac{C_2^2}{2} - U_2 C_{U2} \tag{2.9}$$

With no inlet swirl, $C_{U1} = 0$. From Equation 2.9 it is clear that (assuming adiabatic flow) rothalpy is conserved in the impeller. From Equation 2.15, the static enthalpy change in the impeller can be derived as:

$$h_2 - h_1 = \frac{U_2^2 - U_1^2}{2} - \frac{W_2^2 - W_1^2}{2} \tag{2.10}$$

It is important to note that these equations are applicable only along a mean streamline through the impeller. This is because U_1, C_1 and W_1 are not uniform along the inlet. Depending on the impeller exit design, U_2, C_2 and W_2 might also not be uniform along the impeller exit.

The specific heat at constant pressure is given by:

$$c_p = \left(\frac{\partial h}{\partial T}\right)_p \tag{2.11}$$

By assuming a constant c_p, integrating this equation relative to a reference value (Aungier, 2000) and substituting it into Equation 2.6, the equation for total temperature at any point along a streamline is derived:

$$T_{0n} = T_n + \frac{C_n^2}{2c_p} \tag{2.12}$$

Equation 2.11 shows that the specific heat at constant pressure is a function of temperature $(c_p = f(T))$. One example of an empirical formula which can be used to calculate $c_p = f(T)$ is (Kröger, 2004):

$$c_p = 1.045356 \times 10^3 - 3.161783 \times 10^{-1}T$$
$$+7.083814 \times 10^{-4}T^2 - 2.705209 \times 10^{-7}T^3 \tag{2.13}$$

The relationship between enthalpy, temperature and pressure is quantified by the Gibbs equation.

$$Tds = dh - \frac{1}{\rho}dp \tag{2.14}$$

Using Equation 2.14 and isentropic relationships, the ideal impeller exit temperature can be determined if the impeller pressure ratio is available. Equation 2.15 is used in the 1D mean line code of the compressor design process.

$$\frac{p_{02}}{p_{01}} = \left(\frac{T_{02s}}{T_{01}}\right)^{\frac{\gamma}{\gamma-1}} \tag{2.15}$$

Another important equation that is used in the mean line code is the isentropic relationship between static and total conditions at any point in the flow.

$$\frac{p_{0n}}{p_n} = \left(\frac{T_{0n}}{T_n}\right)^{\frac{\gamma}{\gamma-1}} \tag{2.16}$$

2.5 Diffuser Theory

The diffuser encompasses the space between the exit of the impeller and the inlet to the combustion chamber (positions 2 to 4). In the case of a vaned diffuser, a vaneless gap exists between positions 2 and 3 (the start of the diffuser vanes). For a combustion chamber to operate optimally it is required that the air enters at as low a velocity (kinetic energy) and as high static pressure as possible (Saravanamuttoo *et al.*, 2001).

2.5.1 Diffuser Purpose

The flow exiting the impeller contains a large kinetic energy component, particularly in the tangential direction. The primary objective of a diffuser is to achieve a large as possible static pressure recovery and to reduce the tangential velocity components. The capability of a diffuser to achieve this objective is dependent on the sizing constraints that are imposed on it (Saravanamuttoo *et al.*, 2001).

Diffusers can either be vaned or vaneless, although the primary objective of static pressure recovery is achieved by means of an increasing flow area ratio from diffuser inlet to outlet. For a radial diffuser, the increase in radius from diffuser inlet

to outlet results in an increase in cross-sectional area which in turn results in a decrease in velocity, regardless of whether it is a vaneless or vaned diffuser. Depending on the engine size constraints, the use of vanes assists significantly in reducing the tangential velocity prior to entering the combustion chamber. A compressor with a vaned diffuser therefore usually has a higher efficiency but narrower operating range, compared to one with a vaneless diffuser (Dixon and Hall, 2014).

As shown on the Mollier diagram (Figure 2.7), no work is done on the working fluid that passes through the vaneless space and diffuser. If adiabatic conditions are assumed, the steady flow energy equation between positions 2 and 4 reduces to:

$$h_{02} = h_{03} = h_{04} \qquad (2.17)$$

From the Mollier diagram the increase in static pressure between positions 2 and 4 is clearly observed ($p_4 > p_2$) at the expense of the kinetic energy of the fluid ($C_2^2/2 > C_4^2/2$).

2.5.2 Diffuser Types and Design

The primary purpose of a diffuser is to provide high static pressure and low swirl, uniform flow to the combustion chamber for optimum operation. The size of an MGT engine and the associated sizing constraints on the diffuser section largely dictates how well a diffuser will be able to perform its primary task. Diffuser designs thus vary from a mere extension of the vaneless space, to curved and leaned continuous vaned designs.

One of the major design considerations which affects diffuser design is the state of the impeller exit flow (Kock, 2017). The diffuser inlet vane angle (β_3) is typically designed to align with the impeller exit absolute flow angle (α_2) at a suitable incidence angle (i_3). The impeller exit absolute flow angle (α_2) determines the absolute flow angle at the end of the vaneless gap (α_3). Thus:

$$\beta_3 = \alpha_3 + i_3 \qquad (2.18)$$

2.5.3 Vaneless Gap

In the case of a vaned diffuser, the distance between the impeller blades trailing edge (station 2) and the diffuser vane leading edge (station 3) comprises the vaneless gap section (see Figure 2.8). The vaneless gap is typically defined as a radius ratio (r_3/r_2).
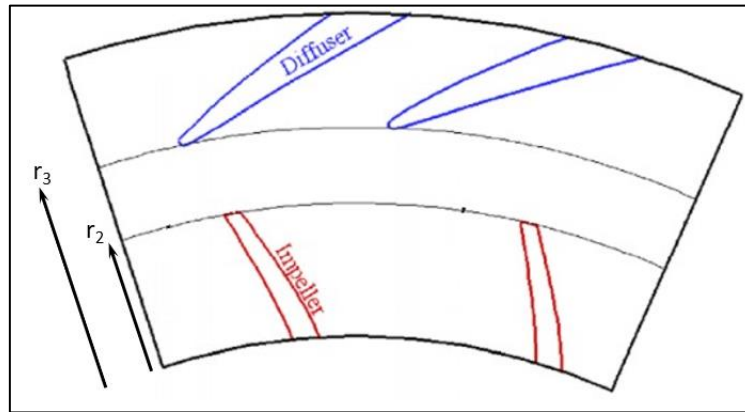
Figure 2.8: Vaneless Gap (Adapted from Gaetani *et al.*, 2012)

Impeller exit absolute velocities may exceed sonic conditions, with the disadvantage of higher Mach numbers leading to early choke conditions in the diffuser throat (Ziegler *et al.*, 2003). The effect of the impeller exit Mach number can be reduced by increasing the size of the vaneless gap. Aungier (1988) also notes that the distorted flow wake from the impeller can be mixed out in the vaneless gap before entering the diffuser inlet.

Aungier (2000) recommends a vaneless gap size of $1.06 \leq r_3/r_2 \leq 1.12$. The larger the vaneless gap, the higher the friction losses in the vaneless gap. Aungier (2000) bases the higher limit on this limiting effect of the friction losses. The lower limit is based on the requirement for sufficient space to mix out the exit flow wake.

2.5.4   Vaned Radial Diffusers

Vaned diffusers are able to diffuse and remove the impeller exit fluid swirl at a higher rate, in a shorter flow path length and radius and at a higher efficiency than vaneless diffusers (Dixon and Hall, 2014). For this reason, vaned diffusers are preferred in MGT engines due to their inherent size limitations.

Diffuser vanes can vary from a simple wedge type profile to aerofoil shaped vanes (Kock, 2017). According to Dixon and Hall (2014), the number of vanes used in the diffuser should be selected with the following in mind:

    i.   More vanes will result in better diffusion and pressure recovery, but at the expense of higher frictional losses and a lower choke mass flow rate.

    ii.   To prevent resonance or sympathetic vibration, the number of diffuser vanes should not be the same as or be a multiple of the number of impeller blades.

Conventional vaned diffuser designs typically include a vaned radial section with a 90° vaneless bend and a set of axial de-swirler vanes (refer Figure 2.9a and b). This conventional configuration can also be replaced by a crossover diffuser (Figure 2.9c), which allows for a more gradual change in flow angle, while still achieving pressure recovery through increasing cross-sectional area.
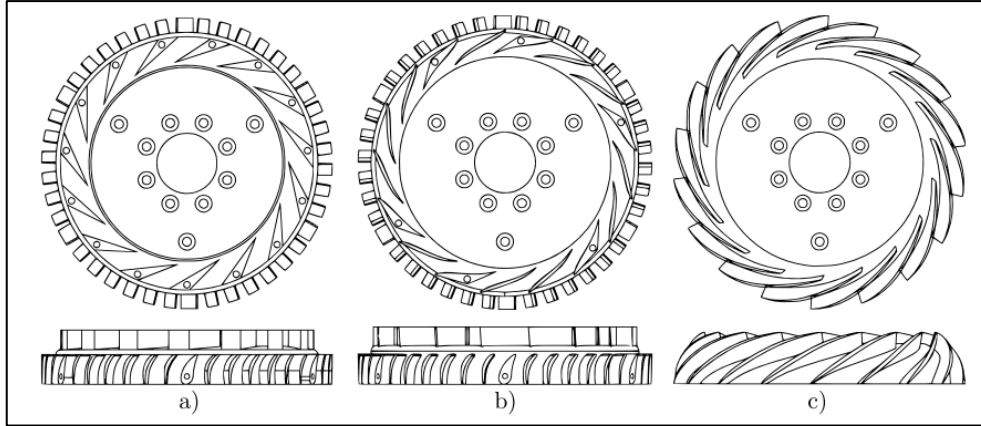
Figure 2.9: a) and b) Examples of Conventional Vaned Diffuser c) Example of Crossover Diffuser (Burger, 2016)

According to Aungier (2000), static pressure recovery in a conventional vaned diffuser is achieved by, firstly, the increase in effective passage area from diffuser inlet to outlet and, secondly, by what he refers to as the blade loading parameter (L). The effective increase in passage area, or the area ratio (AR) is defined as:

$$AR = \frac{A_4}{A_3} \qquad (2.19)$$

The blade loading or fluid turning effect, which is the relationship between the average vane-to-vane pressure difference and the diffuser inlet-to-outlet pressure difference (Aungier, 2000), is quantified using the blade loading parameter (L):

$$L = \frac{\Delta C}{C_3 - C_4} \qquad (2.20)$$

ΔC is defined as the average blade-to-blade velocity difference. At design operating conditions, the inlet and outlet flow angles are nearly equal to the blade angles, in which case simple potential flow yields (Aungier, 2000):

$$\Delta C = \frac{2\pi(r_3 C_{U3} - r_4 C_{U4})}{Z L_B} \qquad (2.21)$$

2.5.5   De-swirler Vanes

De-swirler axial blades are used to reduce the tangential flow (swirl) and thus the absolute flow velocity prior to entering the combustion chamber (Beér and Chigier, 1972).

Annular combustion chambers, as used on most MGT engines, may experience a marked alteration in exit temperature profile based on changes in the inlet velocity profile (Kock, 2017). For this reason, de-swirler vanes play an important role in conventional radial diffusers. They attempt to closely align the flow to axial, uniform conditions, contributing to an optimal combustion process. This also has the advantage of effectively shortening the flow path through the combustion chamber and thus reducing the overall pressure loss as much as possible (Kock, 2017).

2.5.6   Crossover Diffuser

The term 'crossover' diffuser is used by Burger (2016) as a more descriptive and alternative name for a continuous vane diffuser. The crossover diffuser aims for a gradual and continuous connection of the radial (or nearly so) discharge of the impeller with the axial inlet of the combustor within the defined sizing restrictions. It has the advantage that the flow irregularities experienced in the 90° vaneless bend of a conventional diffuser are largely reduced (Kock, 2017). It further allows for the control of the exit velocity vector. A properly designed crossover diffuser can re-align the flow towards the axial direction upon diffuser exit. This eliminates the need for axial de-swirlers.

Jie and Guoping (2010) redesigned the diffuser for an 11 cm diameter MGT engine. The conventional wedge type radial diffuser with axial de-swirler vanes originally used in the engine was replaced with a continuous vane diffuser. An 11% thrust increase was achieved.

Continuous vane diffusers typically display better performance and pressure recovery when compared to similar conventional diffusers, but at the expense of operating range and sometimes also choke mass flow rate (Ling *et al.*, 2007).

2.6   Efficiency and Pressure Ratio

Compressor efficiency is typically measured relative to an ideal isentropic case. Isentropic efficiency is an important performance indicator of a compressor and compares the energy increase of the working fluid relative to the work required to drive the compressor during reversible, adiabatic conditions (Kock, 2017). Higher efficiencies would thus permit a lower power requirement to drive the compressor at the associated operating point (Orth *et al.*, 2001).

The efficiency of each of the individual compressor components is similarly determined. The impeller total-to-total isentropic efficiency is defined as:

$$\eta_{TT,1-2} = \frac{h_{02s} - h_{01}}{h_{02} - h_{01}} \tag{2.22}$$

The complete compressor total-to-total isentropic efficiency is a function of the inlet (position 0) and outlet (position 4) enthalpies, which relate to the inlet and outlet temperatures and pressures as follows:

$$\eta_{TT,0-4} = \frac{h_{04s} - h_{00}}{h_{04} - h_{00}} = \frac{\left(\frac{p_{04}}{p_{00}}\right)^{\frac{\gamma-1}{\gamma}} - 1}{\left(\frac{T_{04}}{T_{00}}\right) - 1} \tag{2.23}$$

The main purpose of a compressor is to provide compressed air to the combustion chamber. Another important performance parameter of a compressor is therefore the pressure ratio (PR). For the compressor, this is a ratio of the total pressure increase from compressor inlet (position 0) to compressor outlet (position 4).

$$PR_{TT,0-4} = \frac{p_{04}}{p_{00}} \tag{2.24}$$

In a centrifugal compressor, pressure recovery is not just achieved because of velocity diffusion, but also because of radius increase. For this reason centrifugal compressors deliver higher per-stage pressure ratios than comparable axial flow compressors (Dixon and Hall, 2014).

In the case of the diffuser, being responsible for static pressure recovery, a measure of the static-to-static pressure recovery is appropriate (Kock, 2017):

$$PR_{SS,2-4} = \frac{p_4}{p_2} \tag{2.25}$$

As the primary objective of a diffuser is to convert kinetic energy to static pressure, the performance parameter to measure this is the static pressure recovery coefficient (C_p). This coefficient provides a ratio of the static pressure gain in the diffuser relative to the diffuser inlet kinetic energy (dynamic pressure) (Krain, 1981).

$$C_p = \frac{p_4 - p_2}{p_{02} - p_2} \tag{2.26}$$

2.7   Conclusion

The development of a rapid design 1D mean line flow tool is reliant on the basic turbomachinery and thermodynamic equations summarised in this chapter. The basic theory is used to verify the performance and working range of a compressor. During this study the theory summarised in this chapter provided a baseline for the analysis of the various test compressors designed by the 1D App. It was found that the initial results obtained from the 1D software were not satisfactory when compared to CFD results. Performance prediction differences in excess of 15% and even 20% were observed.   Therefore, although the baseline 1D and turbomachinery theory provide the basis for the design and flow analysis prediction code, a need for wider performance validation was identified. These are discussed in the next chapters.

Chapter 3:

MATLAB® Application Development

3.1   Introduction

The foremost goal of this project is to develop a first order, rapid design ("quick turnaround") application for the design of a radial or mixed flow compressor using mean line flow analysis. To achieve this, it is essential to develop a user-friendly, simple and intuitive GUI as the front-end for the 1D Application. The 1D App was developed using MATLAB® R2019b.

This chapter covers the development process of the 1D App, with particular focus on the mean line code forming the backbone of the 1D App, which is primarily based on the theory of Aungier (2000).

3.2   1D App Layout

The front-end GUI layout was designed to follow a logical compressor design process. The main window is therefore designed with Tab Groups (user inputs), with the Tabs arranged in the proposed order of design.

Five main design processes are incorporated as user inputs. These include Inlet Thermodynamic Conditions, Impeller Design, Diffuser Design, Overall Performance Analysis and CFD Output. In the case of both Impeller and Diffuser Design, an additional Tab Group is included to cater for the more involved design processes of each.

A schematic of the design process is presented in the flowchart in Figure 3.1. A schematic of the main window of the 1D App is provided in Figure 3.2.
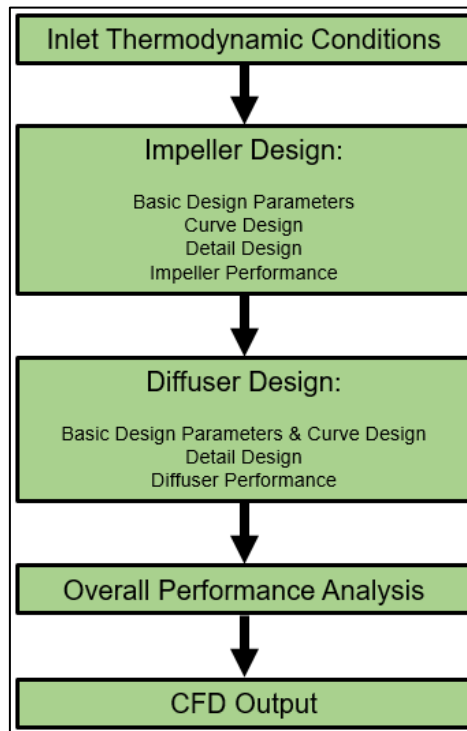
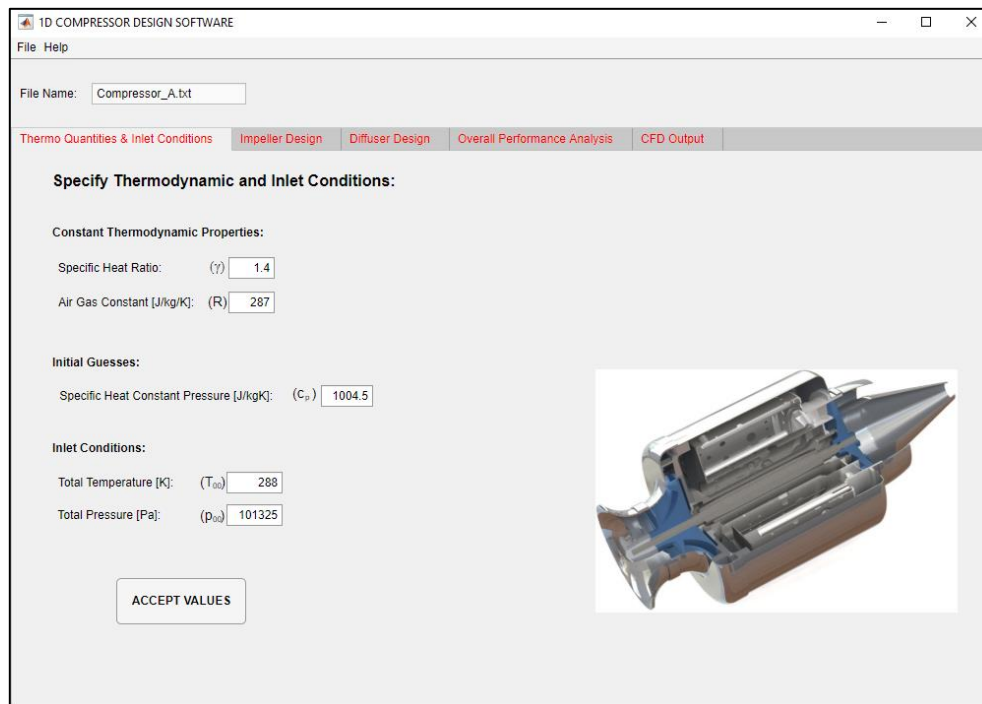Figure 3.1: 1D App Design Logic Flowchart

Figure 3.2: 1D App Main Window Layout

The 1D App also includes the ability to save the parameters of a designed compressor in the form of a text file. A previously designed compressor can also be opened in the 1D App by opening a saved text file.

3.3   Thermodynamic and Inlet Conditions

The first step in the design of a compressor using the 1D App is to define the basic thermodynamic and inlet quantities (refer Figure 3.2). Constant thermodynamic quantities include the specific heat ratio (γ) of air and the gas constant for air (R). Although these values are editable, typical constant values of 1.4 and 287 J/kg·K respectively are pre-populated.

The value for specific heat at constant pressure (c_p) is a function of static temperature. Although this relationship is incorporated in the code, an initial value for c_p need to be defined as part of the initial thermodynamic constants. Even though the value is editable, a pre-populated value of 1004.5 J/kg·K is provided.

Finally, the total inlet temperature (T_{00}) and pressure (p_{00}) are defined. Due to the fact that the 1D App does not cater for any pre-inlet arrangements (i.e. inlet guide vanes), the total conditions at station 0 and 1 are regarded as equal.

3.4   Impeller Design

The impeller design process comprises of four phases. These include defining the basic geometric and design parameters, the basic hub and shroud curve design, the detail design, including the blade geometry, and impeller performance prediction. Each of these phases are detailed below. Flowcharts for the main design processes of the impeller are also provided in Appendix B.

3.4.1   Basic Design Parameters of the Impeller

During the initial phase of the impeller design, data needs to be provided in two sections. The first section encapsulates the basic geometric data of the impeller. This includes the inlet hub radius (r_{1h}), the impeller outlet radius (r_2), the meridional exit angle (α_{C2}), the impeller exit blade angle (β_2), the impeller axial length (z_{1-2}), the number of impeller blades (Z_{imp}), the blade tip clearance (s_{CL}) and the diffusion ratio (DR).

The second section encapsulates data concerned with the design flow conditions of the compressor. These include the design mass flow rate ($\dot{m}$), rotational speed (N) and the desired impeller total-to-total pressure ratio ($PR_{TT,1-2}$). The data provided by the user is sufficient to complete important initial calculations for the

inlet and outlet geometry of the impeller, which is required for the next phase of defining the impeller hub and shroud curves.

An important geometric parameter that needs to be calculated as part of the inlet profile is the inlet shroud radius (r_{1s}). This is done in an iterative manner, aiming to minimise the relative velocity (and thus relative Mach number) at the impeller inlet shroud. The iterative process is started by selecting a suitable value for r_{1s}. The inlet area is then divided into a suitable number of increments (250 set as default). Within the larger iteration, the inlet meridional velocity distribution is determined for each of the selected values of r_{1s}. This is done iteratively. Some assumptions are made regarding the inlet velocity distribution.

    i.   The inlet meridional velocity follows a linear distribution from shroud to hub.

    ii.   The shroud-to-hub velocity ratio is quantified as (adapted from Herbert (1980)):

$$\kappa = \frac{C_{m1s}}{C_{m1h}} \qquad (3.1)$$

For the purpose of the 1D App, κ is selected as 1.45. This value provides a good correlation with CFD results, as well as good mean inlet results.

Aungier (2000) proposed a slightly different inlet velocity distribution based on an approximate stream surface curvature correction procedure. This method provides a pseudo linear inlet velocity distribution, as it is linear from the hub to the mean position, and linear from the mean position to the shroud. Herbert (1980) proposed a linear inlet velocity distribution from hub to shroud. An evaluation of both these proposed methods found that both provided very similar results. For this reason, the simpler linear distribution method is implemented.

With the relationship between C_{m1s} and C_{m1h} now determined, a suitable value for C_{m1h} is chosen. The suitability of the value for C_{m1h} is tested by determining the mass flow rate across the inlet by summing the incremental mass flow rates. With the meridional inlet velocity distribution known, C_{m1i} for each increment is determined:

$$C_{m1i} = \frac{r_i - r_{1h}}{r_{1s} - r_{1h}}(\kappa C_{m1h} - C_{m1h}) + C_{m1h} \qquad (3.2)$$

In the absence of inlet guide vanes:

$$C_{1i} = C_{m1i} \qquad (3.3)$$

From Equation 2.12:

$$T_{1i} = T_{01} - \frac{C_{1i}^2}{2c_p} \tag{3.4}$$

The initial value for c_p is as defined as part of the Thermodynamics and Inlet Conditions input fields for the 1D App. With T_{1i} determined, c_p can be determined more accurately using Equation 2.13. Assuming isentropic conditions at any point, p_{1i} is subsequently determined using Equation 2.16. The incremental area and mass flow rate values are now calculated:

$$A_{1i} = 2\pi r_i \delta r \tag{3.5}$$

$$\dot{m} = \sum_{i=1}^{n} A_{1i} p_{1i} C_{m1i} \tag{3.6}$$

The determined mass flow rate can be compared to the known mass flow rate as defined as part of the Thermodynamics and Inlet Conditions of the 1D App. If the calculated mass flow rate is not equal to the defined mass flow rate (within a pre-defined tolerance), the selected value for C_{m1h} is updated and the process repeated. Once the mass flow converges, the relative velocity at the inlet shroud is calculated knowing that $U_{1s} = \omega r_{1s}$:

$$W_{1s} = \sqrt{(U_{1s} + C_{1s} sin\alpha_{C1})^2 + (C_{1s} cos\alpha_{C1})^2} \tag{3.7}$$

With no inlet guide vanes, $\alpha_{C1} = 0$. With the value of W_{1s} known for the initially selected r_{1s}, a new r_{1s} is selected and the entire process repeated until a minimum value for W_{1s} is found.

Once the inlet geometry has been determined, the impeller outlet geometry is calculated. This is done by assuming that the rothalpy (I_R) remains constant in the impeller (Equation 2.9). The rothalpy at the inlet mean position is determined as follows, with $C_{U1} = 0$:

$$I_R = c_p T_1 + \frac{C_1^2}{2} \tag{3.8}$$

The values for T_1 and C_1 are taken as the mean position values as determined in the iterative process to determine W_{1s}.

The process to solve the impeller outlet geometry is dictated by the meridional exit angle. Two conditions are considered, namely $\alpha_{C2} = 90°$ ($r_2 = r_{2h} = r_{2s}$) or

$\alpha_{C2} < 90°$ ($r_{2h} < r_{2s}$). For $\alpha_{C2} < 90°$, r_{2s} is taken as the user-defined value for r_2, and r_{2h} is determined iteratively. An initial guess for r_{2h} is $r_{2h} = r_{2s}$.

The impeller outlet slip factor is determined using the Wiesner (1967) slip factor equation. Although a more accurate slip approximation is used during the detail performance analysis of the impeller (see section 3.4.4), the Wiesner approximation is adequate for the initial impeller geometry creation.

$$\sigma_s = 1 - \frac{\sqrt{cos\beta_2}\, sin\alpha_{C2}}{Z^{0.7}} \tag{3.9}$$

With r_{2h} and r_{2s} known, the mean outlet radius (r_2) can be determined as the average of the two values. Having calculated r_2, the mean outlet rotational velocity ($U_2 = \omega r_2$) is determined.

Another important impeller design parameter is the diffusion ratio (DR). Cumpsty (2004) explained that the diffusion ratio provides an indication of the pressure rise in the impeller at the expense of relative fluid velocity.

$$W_2 = \frac{W_{1s}}{DR} \tag{3.10}$$

Cumpsty (2004) also noted that typical values for diffusion ratios varies between 1.3 and 1.7. A value that is too high can lead to an unusable design due to high impeller losses. Although the 1D App allows for the user to define a specific diffusion ratio, a default value of 1.5 is proposed by the 1D App. This value was used for all the test compressors.

With W_2 known, the relative mean flow exit angle (β_2') is determined by iteratively solving the following implicit equation:

$$\frac{W_2}{sin(\pi + \beta_2)} = \frac{\frac{U_2}{\sigma_s} - \frac{W_2 sin\beta_2'}{\sigma_s} - U_2 + W_2 sin\beta_2'}{sin(\beta_2' - \beta_2)} \tag{3.11}$$

The derivation of Equation 3.11 is presented in Appendix A.

Using the impeller exit velocity triangle, C_2 is determined. The exit total enthalpy (h_{02}), total temperature (T_{02}), static temperature (T_2) and static pressure (p_2) are then determined by employing Equations 2.9, 2.12, 2.13 and 2.16. The mean exit density is determined using the basic ideal gas equation of state:

$$\rho_2 = \frac{p_2}{RT_2} \tag{3.12}$$

Depending on whether the impeller is a pure radial or mixed flow configuration, the exit area and width are determined. In the case that $\alpha_{C2} = 90°$, the exit area is simply determined as:

$$A_2 = \frac{\dot{m}}{\rho_2 C_{m2}} \tag{3.13}$$

after which the exit width is calculated:

$$b_2 = \frac{A_2}{2\pi r_2} \tag{3.14}$$

With $\alpha_{C2} = 90°$, the determination of the exit geometry is now complete. In the event that $\alpha_{C2} < 90°$, the process is iterative, and the exit area is calculated as follows:

$$A_2 = \pi \left(r_{2s} \frac{r_{2s}}{\cos\alpha_{C2}} - r_{2h} \frac{r_{2h}}{\cos\alpha_{C2}} \right) \tag{3.15}$$

The exit mass flow rate is now determined and compared to the known mass flow rate:

$$\dot{m} = \rho_2 C_{m2} A_2 \tag{3.16}$$

In the event that the calculated mass flow rate differs from the known mass flow rate, the initial guestimate for r_{2h} is updated and the process repeated until the mass flow rate converges.

3.4.2 Impeller Shape Design

The impeller meridional shape is designed using a 7-point Bezier curve for both the hub and shroud curves. Choosing U intervals along the curves and with $n = 7$:

$$[z_U \ \ r_U] = \sum_{k=0}^{n-1} [z_k \ \ r_k] \binom{n}{k} U^k (1 - U)^{n-k} \tag{3.17}$$

The 7 points defining the hub and shroud Bezier curves are defined by the user under the Impeller Curve Design input field in the 1D App (see Figure 3.3). To simplify the process, the provided curve values are normalised $(0 - 1)$ between the maximum and minimum radius and axial length. The z-parameter of point 6 of the hub curve is automatically calculated such that the hub meridional exit angle is equal to the defined meridional exit angle.
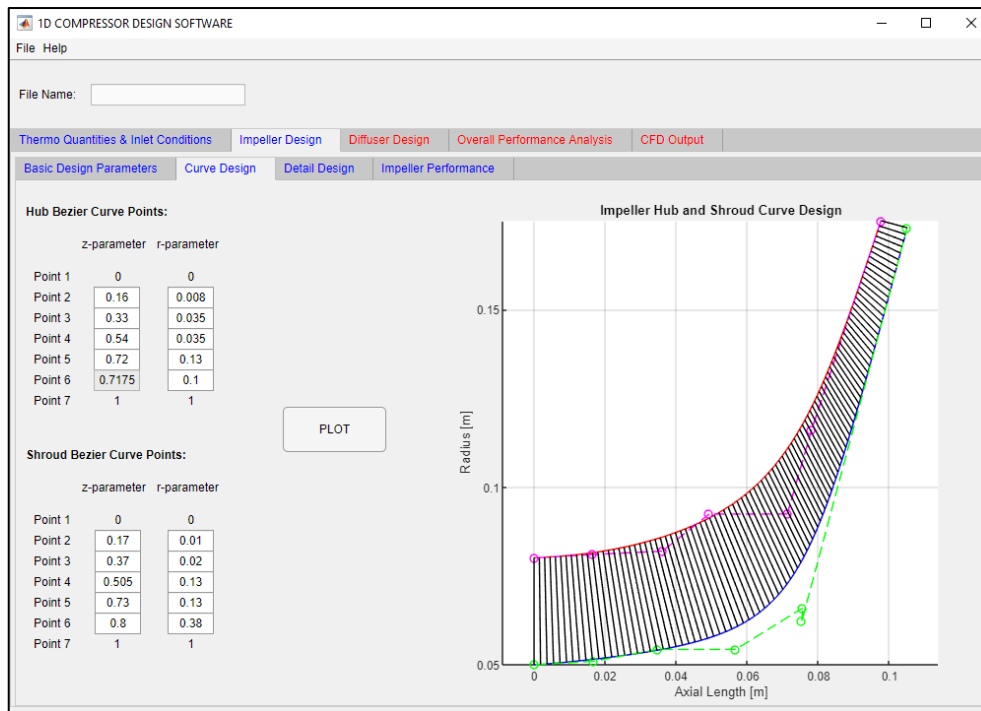
Figure 3.3: Impeller Curve Design Tab

With the geometric data for both the hub and shroud curves known, these are divided into equal parts and connected along quasi-normal lines.

3.4.3 Impeller Detail Design

Once the impeller hub and shroud curves are defined, the impeller detail design is performed. Under the Detail Design input field, the user specifies details regarding the impeller blade thicknesses, splitter blade length ratio and blade lean (rake) angle distribution parameters.

The 1D App allows for automatic determination of main blade and splitter blade thicknesses, but the user have the ability to specify these at the leading and trailing edge hub and shroud positions.

The user can specify an impeller design with or without splitter blades. If splitter blades are selected, the user specifies a length ratio of the splitter blade relative to the full blade length (a value between 0 and 1). Aungier (2000) defined an effective blade number (Z_{eff}) based on this ratio, which is used during the impeller design process:

$$Z_{eff} = Z_{FB} + Z_{SB}\frac{L_{SB}}{L_{FB}} \tag{3.18}$$

Inlet Conditions and Inlet Blade Angle

The detail design of the impeller commences by determining the inlet conditions as per section 3.4.1. Additionally, the inlet blade angle (β_1) distribution is determined. Certain assumptions are made regarding the inlet blade angle distribution:

    i.   The inlet blade angle distribution is linear from hub to shroud.

    ii.   The incidence angles at the hub and shroud are zero: $i_{1s} = i_{1h} = 0$.

From the inlet velocity triangle (Figure 2.6):

$$\beta_{1h} = \beta'_{1h} = acos\left(\frac{C_{m1h}}{W_{1h}}\right) \tag{3.19}$$

β_{1s} is calculated in a similar fashion. The complete inlet blade angle distribution can subsequently be determined.

Aungier (2000) proposed that the mean stream surface position along the inlet be determined where equal amounts of mass flow passes above and below the mean stream surface. Once this point is established, all the required geometric and thermodynamic mean parameters are determined and saved as mean inlet values.

Outlet Geometry

The core of the detail impeller design process is to determine the outlet geometric parameters in conjunction with the design of the main and splitter blades (if selected). The process followed to calculate the outlet geometric parameters is similar to the process described in section 3.4.1. The presence of the blades at the exit have to be considered, however. As explained in section 3.4.1, two outlet calculation procedures exist, depending on the meridional exit angle. In the event that $\alpha_{C2} = 90°$, Equation 3.14 changes as follows:

$$b_2 = \frac{A_2}{2\pi r_2 - \dfrac{Z t_{B2}}{cos\beta_2 cos\theta_{R2}}} \tag{3.20}$$

In the event that $\alpha_{C2} < 90°$, Equation 3.16 changes as follows:

$$\dot{m} = \rho_2 C_{m2}\left[\pi\left(r_{2s}\frac{r_{2s}}{cos\alpha_{C2}} - r_{2h}\frac{r_{2h}}{cos\alpha_{C2}}\right) - \frac{Z t_{B2} b_2}{cos\beta_2 cos\theta_{R2}}\right] \tag{3.21}$$

In both these cases, blade thicknesses and rake angles are not available yet and are only calculated in the detail design process. As a first iteration, these values are taken as zero and are updated after completion of each full design cycle.

Blade Angle Distribution Along Hub and Shroud Curves

Aungier (2000) proposed a numerical process for calculation of the blade angle distribution along the hub and the shroud curves (see Appendix A). These blade angle distributions are reliant on the rake angle parameter (K). This value, as well as the inlet blade rake angle, can be edited by the user under the Detail Design input field. Once the blade angle distribution is calculated along both the hub and shroud curves, the blade angle at any point in the impeller is determined based on the design criteria that the blade angle varies linearly from hub to shroud along a quasi-normal.

Hub and Shroud 3D Camber Lines

With the blade angle distribution along the hub and shroud known, the 3D camber line of the blades is determined along the hub and shroud. The Cartesian coordinate system defined in the 1D App is schematically displayed in Figure 3.4 below.
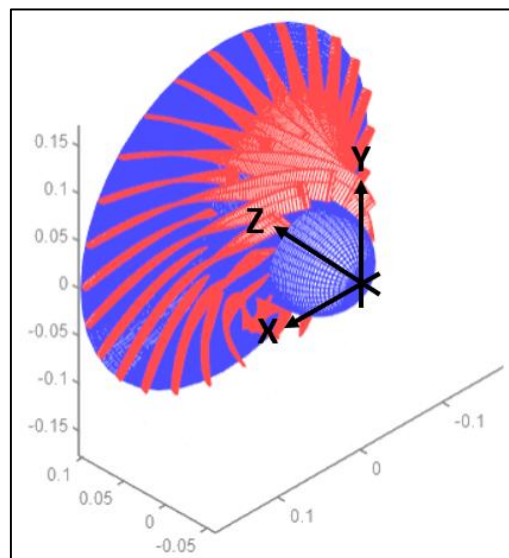

Figure 3.4: Coordinate System

The 3D camber line of the main blade along the hub is calculated as follows:

$$Z_{FB_{hi}} = z_{hi}$$

$$X_{FB_{hi}} = r_{hi} sin\left(\sum_{i=1}^{n} \delta\theta_i\right)$$

$$Y_{FB_{hi}} = r_{hi} cos\left(\sum_{i=1}^{n} \delta\theta_i\right) \qquad (3.22)$$

with:

$$\delta\theta_i = tan\left(\frac{\beta_{h_i} + \beta_{h_{i+1}}}{2}\right)\frac{\Delta m_h}{\bar{r}_i}$$

where Δm_h is the incremental meridional length between quasi-normals along the hub curve and $\bar{r}_i$ is the mean radius between consecutive quasi-normals on the hub curve. The same formulas are used for the splitter blade camber line along the hub curve, albeit commencing further along the hub curve. The 3D camber line of the main and splitter blades along the shroud curve is calculated in a similar manner.

Rake Angle Distribution

With the blade camber line 3D coordinates along both the hub and shroud known, the blade rake angle (θ_R) distribution is determined. The rake angle is the angle between the blade hub-to-shroud line and the line normal to the meridional surface (refer Figure 3.5).
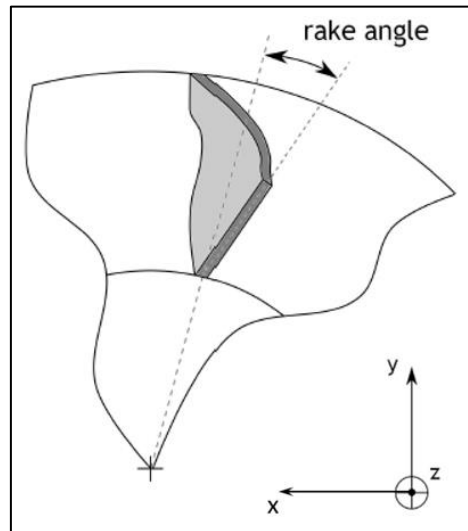

Figure 3.5: Rake Angle (adapted from Schiff (2013))

Along the hub blade camber line, at each quasi-normal, the normal vector from the hub point ($\bar{B}$), as well as the vector between the hub point and shroud point ($\bar{A}$) are determined as follows:

$$\bar{A} = (x_s - x_h)\mathbf{i} + (y_s - y_h)\mathbf{j} + (z_s - z_h)\mathbf{k}$$
$$\bar{B} = (x_n - x_h)\mathbf{i} + (y_n - y_h)\mathbf{j} + (z_n - z_h)\mathbf{k}$$

(3.23)

From vector formulations, the rake angle at each quasi-normal are determined:

$$\theta_R = acos\left(\frac{\bar{A} \cdot \bar{B}}{|\bar{A}||\bar{B}|}\right)$$

(3.24)

The rake angle for each quasi-normal is calculated accordingly.

Blade Thickness Distribution

As part of the blade design, the user has the ability to select blade thickness parameters or allow the 1D App to automatically calculate suitable blade thickness parameters. The blade thickness is defined by four parameters, namely the thickness of the blade at the inlet hub (t_{B1h}), inlet shroud (t_{B1s}), outlet hub (t_{B2h}) and outlet shroud (t_{B2s}). The inlet blade thickness parameter is a slight misnomer, as the blade actually has a zero thickness at the inlet. The inlet parameter actually refers to the maximum thickness of the blade, which is reached some distance behind the leading edge along the camber line. The blade thickness distribution used in the 1D App is based on the procedure as proposed by Verstraete, *et al.* (2010). A schematic of this procedure is provided in Figure 3.6.
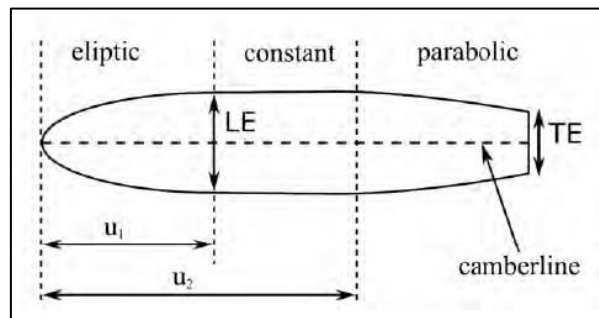
Figure 3.6: Blade Thickness Distribution Along Camber Line (not to scale)
(Verstraete *et al.*, 2010)

The values for u_1 and u_2 are defined as 0.1 and 0.9 respectively in the 1D App code. In the event that the user selects the option for the blade thickness distribution to be calculated automatically, the thickness parameters are determined as a function of the outlet width (b_2), subject to certain maximum values:

$$t_{B1h} = 0.3b_2; \ t_{B1h} \leq 0.0025 \ m$$
$$t_{B1s} = t_{B2h} = t_{B2s} = 0.2b_2; \ t_{B1s} = t_{B2h} = t_{B2s} \leq 0.002 \ m$$

(3.25)

Appendix A presents the detail blade thickness calculations. The thickness distribution used for the main blade is also incorporated for the splitter blade. The splitter blade thickness distribution also commences with a similar elliptical section. The parabolic trailing edge section of the splitter blade commences at the same point as the main blade trailing edge section along the meridional curve. Blade thickness distribution between the hub and shroud vary linearly along the applicable quasi-normal.

Blade 3D Suction and Pressure Coordinates

With the blade camber line 3D coordinates known, as well as the blade thickness distribution available, the 3D coordinates of the suction and pressure sides of the blades are determined. The calculations for the 3D coordinates for the main blade suction side along the hub curve follows:

$$Z_{FB_{h\,suc\,i}} = Z_{FB_{hi}}$$

$$X_{FB_{h\,suc\,i}} = X_{FB_{hi}} + \frac{1}{2}\left(\frac{t_{Bhi}}{cos\theta_{Li}cos\beta_{hi}}\right)cos\left(\sum_{i=1}^{n}\delta\theta_i\right)$$

$$Y_{FB_{h\,suc\,i}} = Y_{FB_{hi}} - \frac{1}{2}\left(\frac{t_{Bhi}}{cos\theta_{Li}cos\beta_{hi}}\right)sin\left(\sum_{i=1}^{n}\delta\theta_i\right)$$

(3.26)

For the pressure side of the blade along the hub:

$$Z_{FB_{h\,pres\,i}} = Z_{FB_{hi}}$$

$$X_{FB_{h\,pres\,i}} = X_{FB_{hi}} - \frac{1}{2}\left(\frac{t_{Bhi}}{cos\theta_{Li}cos\beta_{hi}}\right)cos\left(\sum_{i=1}^{n}\delta\theta_i\right)$$

$$Y_{FB_{h\,pres\,i}} = Y_{FB_{hi}} + \frac{1}{2}\left(\frac{t_{Bhi}}{cos\theta_{Li}cos\beta_{hi}}\right)sin\left(\sum_{i=1}^{n}\delta\theta_i\right)$$

(3.27)

The same calculations are used for determining the suction and pressure side 3D coordinates of the blades on the shroud curve.

Passage Area

The calculation of the passage area also requires an iterative procedure. For each quasi-normal, the corresponding total passage area (A_{pass_i}) is guessed. The guessed passage area is used to incrementally determine the quasi-normal length and compare it to the known length of the quasi-normal (see Figure 3.7).
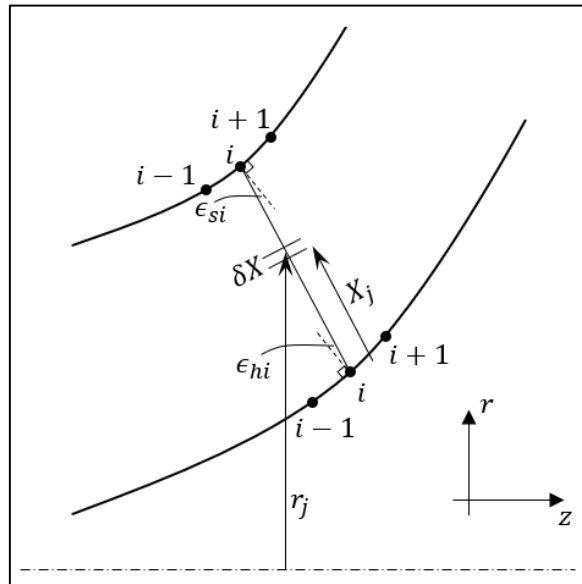
Figure 3.7: Incremental Calculation of Quasi Normal Line Length

The guessed area is divided into *n* increments:

$$\delta A_{pass_i} = \frac{A_{pass_i}}{n} \tag{3.28}$$

Starting from the hub, the length of each increment along the quasi-normal is determined:

$$X_{j+1} = X_j + \frac{\delta A_{pass_i}}{cos\epsilon_j cos\beta_j \left(2\pi r_j - \frac{Z t_{Bj}}{cos\beta_j cos\theta_{Rj}} \right)}$$

where:

$$\beta_j = \frac{X_j}{L_{QN_i}} (\beta_{si} - \beta_{hi}) + \beta_{hi} \tag{3.29}$$

$$t_{Bj} = \frac{X_j}{L_{QN_i}} (t_{Bsi} - t_{Bhi}) + t_{Bhi}$$

Once the last increment along the quasi-normal is reached (X_n), this value is compared to the known quasi-normal length (L_{QN_i}). If these values do not correspond, the guesstimate of the passage area is updated, and the process repeated until the quasi-normal length converges. This process is repeated for each quasi-normal. It is important to note that the number of blades (Z) in the above equation includes the splitter blades once the applicable quasi-normals are reached.

Meridional Mean Streamline and 3D Blade Length

The next phase in the impeller detail design process entails the calculation of the full and splitter blade lengths along the mean streamline. This line is formed by the locus of mean radii points of all the quasi-normals along the stream path and not along the meridional length. The mean blade angle and rake angle at each quasi-normal are therefore important parameters used in the calculation process in order to determine the tangential direction and distance shift of the mean point at each consecutive quasi-normal. With the mean radius, blade angle and rake angle known at each mean point on a quasi-normal, the 3D blade and streamline lengths are calculated.

The meridional mean streamline position and length are determined first. With the mean positions at both the inlet and outlet known, the mean position along each quasi-normal is linearly interpolated between these two end positions.

The mean position along each quasi-normal is determined by firstly calculating the mean increment position along the quasi-normal. Again, selecting n increments along each quasi-normal:

$$\bar{n}_{QN_i} = \frac{n}{2} + 1 + \left(\bar{n}_{QN_1} - \left(\frac{n}{2} + 1 \right) \right) sin \left(atan \left| \frac{dr}{dz} \right|_i \right) \qquad (3.30)$$

Using this result, the actual length along each quasi-normal to the mean position on that quasi-normal is calculated:

$$\bar{X}_i = L_{QN_i} \frac{\bar{n}_{QN_i}}{n} \qquad (3.31)$$

In terms of the meridional coordinate system, the mean streamline coordinates are determined as follows:

$$\bar{r}_i = r_{h_i} + \bar{X}_i sin \left[\pi + atan \left(\frac{dr}{dz} \right)_i \right]$$

$$\bar{z}_i = z_{h_i} + \bar{X}_i cos \left[\pi + atan \left(\frac{dr}{dz} \right)_i \right]$$

$$(3.32)$$
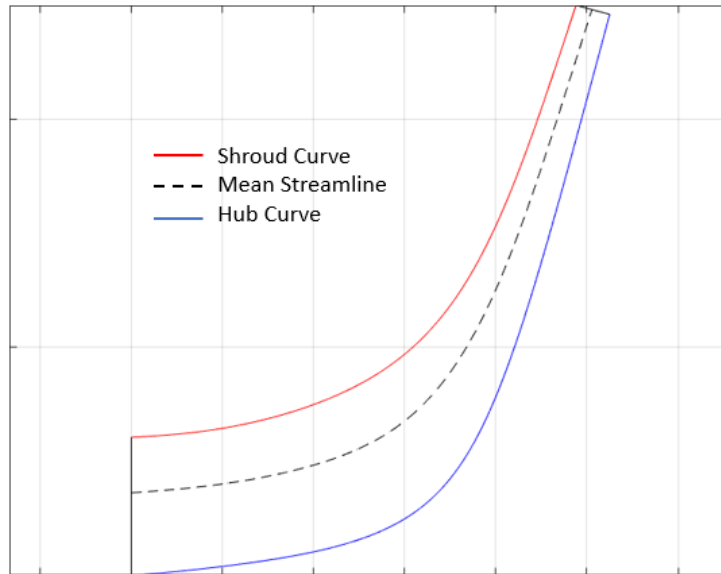
Figure 3.8: Meridional Mean Streamline Position

With the mean meridional distribution available (see Figure 3.8), both the mean meridional length and mean 3D blade length can be determined. Having divided the impeller into k quasi-normals:

$$
\begin{aligned}
L_{MSL} &= \sum_{i=1}^{k} \sqrt{(\bar{z}_i - \bar{z}_{i-1})^2 + (\bar{r}_i - \bar{r}_{i-1})^2} \\
L_B &= \sum_{i=1}^{k} \frac{\sqrt{(\bar{z}_i - \bar{z}_{i-1})^2 + (\bar{r}_i - \bar{r}_{i-1})^2}}{cos\bar{\beta}_i}
\end{aligned}
\tag{3.33}
$$

Throat Position

As an initial estimate, the passage area distribution along the impeller is used to determine the throat position. This is achieved by determining where the passage area reaches a minimum after the inlet. Once this position is determined, the throat position is refined utilising the procedure to determine the throat width as proposed by Aungier (2000) (see Appendix A).

Re-calculation of Outlet Geometry

With the first main impeller design iteration complete and with the exit rake angle and blade thickness known, the main design loop is restarted, and the outlet geometry recalculated with these known values. The main design loop is run for only 5 iterations in the 1D App, as the exit geometric values converges rapidly.

<u>User Controlled Rake Angle Distribution</u>

The entire impeller design process is based on a user-defined leading-edge rake angle (θ_{R1}) and rake angle distribution parameter (K). Aungier (2000) proposed that the rake angle distribution is maintained below a maximum absolute value of 15° as far as possible, especially at the leading and trailing edges.

On completion of the impeller design process, the 1D App provides feedback in terms of the maximum calculated absolute rake angle along the blade as well as a graphical representation of the entire rake angle distribution (see Figure 3.9). It often happens during the design process that the rake angle exceeds 15° at some point along the blade. In such a case the user has to re-select the leading-edge rake angle and/or the rake angle distribution parameter. The leading-edge rake angle is typically chosen between 0° and 15°. The rake angle distribution parameter (K) was typically found to be between 0.4 and 0.6, although its hard limits are between 0 and 1. The selection of θ_{R1} and K therefore is a manual iterative process aimed at choosing values for θ_{R1} and K such that the rake angle distribution remains within 15°.
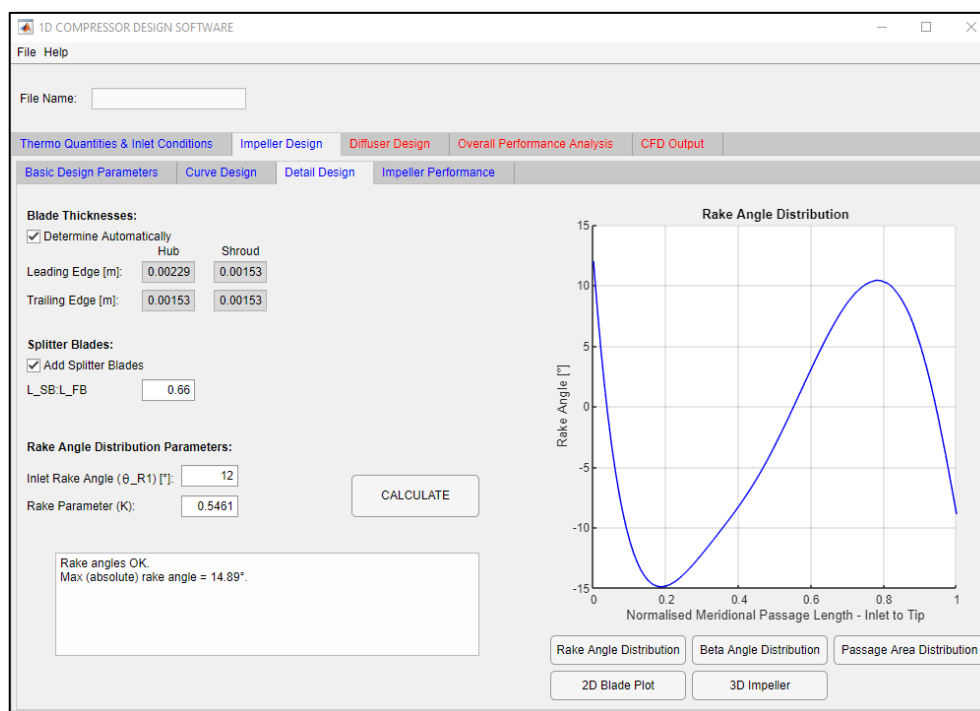

Figure 3.9: Impeller Detail Design Tab – Rake Angle Distribution

3.4.4 Impeller Performance

Once the impeller is designed, the mean line performance prediction the impeller at design conditions is performed. The performance prediction utilised in the 1D App is primarily based on the work of Aungier (2000) and MATLAB ® coding initially developed by De Wet (2012). Three significant alterations to the available in-house mean line code for impeller performance prediction are however incorporated in the 1D App.

Slip Factor

Various slip factor prediction models have been developed for radial and mixed flow compressor performance analysis. These include the models of Stodola (1945), Wiesner (1967) and Eck (1973) as summarised by von Backström (2006). These models were found to not necessarily perform well across a wide range of impeller types (Qiu *et al.*, 2011). The in-house mean line code (as originally developed by De Wet (2012)), has been using the Wiesner (1967) slip factor. Bindeman (2019) specifically investigated the effect of various slip models on the accuracy and usability of the in-house mean line code. He concluded that the Ji *et al.* (2011) slip formulation was preferable due to its reliable results for both radial and mixed flow impellers. For this reason the 1D App impeller performance prediction code was updated to incorporate the Ji *et al.* (2011) slip formulation:

$$\sigma_s = 1 - \left(\frac{FZ}{2Z + F\pi sin\alpha_{C2}}\right)\left[(2 + \phi_2 tan\beta_2)sin\alpha_{C2} + \frac{\phi_2 r_2}{cos^2\beta_2}\frac{d\beta}{dm}\bigg|_2\right]$$

(3.34)

where:

$$F = \frac{Z}{\pi}sin\left(\frac{\pi}{Z}\right)cos\left(|\beta_2| - \frac{\pi}{Z}\right) - \frac{Zt_{B2}}{2\pi r_2 cos\beta_2}$$

Impeller Choke Prediction

As verification, 18 test compressors were developed using the 1D application (details are provided in Appendix C). These test compressors covered a wide range of design velocities, mass flow rates, as well as meridional exit angles (mixed flow compressors). Predicted performance results were verified using Numeca/FINE™ Turbo CFD software. Initial comparisons between 1D and CFD results did not correspond well for the majority of the test compressors. In particular, it was found that the 1D software provided poor impeller choke prediction. Both Klausner and Gampe (2014) and Sundström *et al.* (2017) found deviations between 1D performance predictions and experimental/CFD results in the choke region. After further investigation it was found that there exists a relationship between choke mass flow prediction in the impeller and impeller exit

slip factor for higher flow compressors ($\phi_2 > 0.34$). For lower flow impellers ($\phi_2 < 0.34$) it was found that the choke mass flow prediction is related to the flow itself. Details of these findings are provided in Chapter 5. Once these relationships were quantified, the 1D App impeller performance prediction code was updated accordingly. This update provided much better choke correlation across all 18 test compressors.

General Performance Over-prediction

Further comparison of the 1D results versus the CFD results indicated that the 1D software generally over-predicted compressor performance, i.e. total-to-total efficiency and pressure ratio. Further investigation into the over-prediction of compressor performance by the 1D software revealed three contributing factors. One of these factors entailed a general over-prediction in impeller performance (details are provided in Chapter 5). Once the impeller performance prediction anomaly was quantified, the 1D App impeller performance prediction code was updated accordingly.

3.5 Diffuser Design

The 1D App only caters for one diffuser type and configuration, namely a vaned crossover diffuser. The diffuser comprises of two sections, namely an initial vaneless gap and a continuous crossover vaned section. The diffuser design process comprises of three phases. These include the basic design parameters and curve design, the detail design of the diffuser, including the blade geometry, and performance prediction of the diffuser and compressor. Each of these phases are detailed below. Flowcharts for the main design processes of the diffuser are provided in Appendix B.

3.5.1 Diffuser Basic Design Parameters and Curve Design

In the basic design phase, the user defines basic geometric data of the diffuser (see Figure 3.10). This includes the hub and shroud exit radii (r_{4h} and r_{4s}), the diffuser axial length (z_4), a Bezier Curve Curvature Constant, the required diffuser blade mean inlet incidence angle (i_3) and the vaneless gap radius ratio (r_3/r_2).

As is the case with the impeller hub and shroud curves, the diffuser meridional curve is also designed using a 7-point Bezier Curve. The difference however is that in the case of the diffuser, the user does not have the option to design both the hub and shroud curves independently. Only a diffuser centreline curve is designed with the diffuser meridional width being equally spaced around the centreline. The user does not have full control over the 7 Bezier Curve points and can only specify a curvature control parameter.
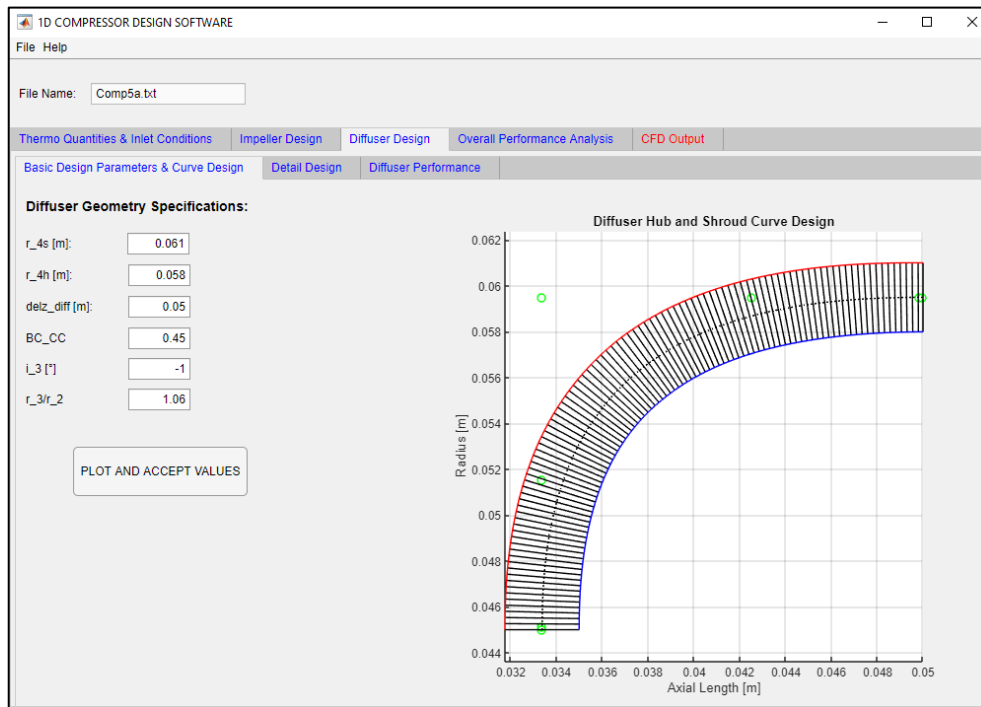
Figure 3.10: Diffuser Basic Design Parameters and Curve Design Tab

The diffuser curve design process also includes the definition of equally spaced quasi-normals in the meridional direction.

3.5.2 Diffuser Detail Design

A major part of the detail diffuser design process involves the design of the diffuser blades. Under the diffuser Detail Design input, the user can specify various parameters related to the diffuser blade. This includes the number of diffuser blades. Aungier (2000) proposed that the number of diffuser blades (Z_{diff}) should either be 1 more or 1 less than the number of impeller blades (Z_{diff}). To improve the stall incidence range, $10 \leq Z_{diff} \leq 20$ is additionally recommended.

The 1D App allows the user to specify the maximum and trailing edge diffuser blade thicknesses. The user can further select for this parameter to be automatically calculated by the 1D App. In this case the 1D App simply uses default values of 2 mm for maximum blade thickness and 1 mm for trailing edge blade thickness.

The 1D App bases the design of the diffuser blades on the process proposed by Aungier (2000). This process requires two blade design parameters (K_3 and K_4) as well as the diffuser blade trailing edge angle (β_4) to be specified. The user has the ability to manually enter these three values or the user can select the option for the 1D App to optimise these values.

Vaneless Gap Performance

In order to fix the blade leading edge design parameters of the vaned section of the diffuser, the flow conditions at the exit of the vaneless gap need to be determined. The location of the leading edge of the diffuser vanes (exit of the vaneless gap) is dictated by the user-defined vaneless gap ratio (r_3/r_2). With the geometric parameters of the vaneless gap available and the impeller exit flow conditions (at station 2) available, the flow through the vaneless gap can be modelled.

The mean flow analysis for the vaneless gap incorporated in the 1D App is based on vaneless space performance theory as proposed by Aungier (2000) and initially incorporated in the in-house mean line code by De Wet (2012). The approach is to discretise the vaneless gap into control volumes and to follow an incremental flow analysis procedure. The model aims at predicting the losses through the vaneless gap. These losses include surface friction losses, diffusion losses and passage curvature losses. This process enables the determination of the mean flow conditions at the exit of the vaneless gap (station 3).

Blade Design

Aungier (2000) recommended low inlet blade angles, preferably in the range $16° \leq \beta_3 \leq 22°$ (measured from the tangential). This is however largely dictated by impeller exit flow conditions and not always attainable.

The 1D App allows the user to specify the required diffuser blade leading edge incidence angle. Aungier (2000) recommends an incidence angle in the order of -1°, which is set as the 1D App default value. Based on Equation 2.18, β_3 is calculated using the absolute flow angle at the exit of the vaneless gap (α_3).

The next step in the diffuser vane design process is to define the shape of the vane itself. Aungier (1988) proposes a mean camber line method, around which a thickness distribution is defined. Defining the parameter $\eta = r/r_3$, the camber line is determined by:

$$\theta(\eta) = A \ln(\eta) + B(\eta - 1) + C(\eta^2 - 1) + D(\eta^3 - 1) \qquad (3.35)$$

To determine the values of A, B, C and D, four boundary conditions are required. Two are determined from the blade angle leading edge and trailing edge angles while the other two are selected such that the blade loading distribution remains within controlled limits. It can be shown that:

$$D = \frac{(cot\beta_4 - cot\beta_3)(K_3 + K_4 - 2)}{3(R-1)^3}$$

$$C = \frac{(cot\beta_4 - cot\beta_3)(K_4 - K_3)}{4(R-1)^2} - \frac{9D(R+1)}{4}$$

$$B = \frac{K_3(cot\beta_4 - cot\beta_3)}{R-1} - 4C - 9D$$

$$A = cot\beta_3 - B - 2C - 3D$$

(3.36)

where:

$$K_{(n)} = \frac{R-1}{cot\beta_4 - cot\beta_3}\frac{dcot\beta_{(n)}}{d\eta}$$

Two options for specifying the blade thickness distribution are proposed by Aungier (2000):

i.   A constant thickness vane with the option of tapering it towards the leading edge.

ii. An aerofoil shape closely resembling the NACA 66-006 profile.

The choice between these two options might not be performance driven, but rather influenced by cost, ease of manufacturing, stress and vibration. The 1D App incorporates the NACA 66-006 option. The following approximations are used:

$$\frac{t_b}{t_{b\,max}} = t_0 + (1 - t_0)\left(\frac{2x}{c}\right)^n \qquad for\,\frac{x}{c} \leq 0.5$$

$$\frac{t_b}{t_{b\,max}} = t_0 + (1 - t_0)\left(2 - \frac{2x}{c}\right)^n \qquad for\,\frac{x}{c} > 0.5 \qquad (3.37)$$

$$t_0 = \frac{\left[t_{b3} + (t_{b3} - t_{b4})\frac{x}{c}\right]}{t_{b\,max}}$$

and:

$$n = 0.755 \left(0.57 - \frac{x}{c} \right) \qquad for \frac{x}{c} \leq 0.539$$

$$n = 1.225 \left(\frac{x}{c} - 0.52 \right) \qquad for \frac{x}{c} > 0.539$$

(3.38)

Part of the 1D App diffuser blade design process is to ensure that the overall diffuser stays within certain size limits. Aungier (2000) recommended the following limits in terms of the Equivalent Divergence Angle ($2\theta_c$) and Blade Loading parameter (L):

$$10° \leq 2\theta_c \leq 11°$$

(3.39)

$$0.3 \leq L \leq \frac{1}{3}$$

(3.40)

In the event that design parameters specified by the user leads to a diffuser design which results in an Equivalent Divergence Angle or a Blade Loading parameter falling outside of the specified limits, the 1D App will warn the user accordingly.

Throat Position

The diffuser throat position and area are determined in a similar fashion as for the impeller throat.

Design Optimisation

The 1D App provides the user the ability to automatically determine the best values for K_3, K_4 and β_4. In the case of K_3 and K_4, the 1D App searches for optimum values within the ranges of 1.5 and 3.5, and 1 and 3 respectively (as proposed by Aungier (2000)). β_4 is optimised within the range 0° to 40° relative to the axial direction. These optimum values are chosen such that $PR_{TS,14}$ is a maximum.

During the optimisation process, the 1D App ensures that all possible outcomes conforms to the size limits as specified in Equations 3.39 and 3.40. The 1D App further selects possible outcomes within the stall limit as proposed by Aungier (2000). The stall limit (α_{3s}) is determined as follows:

$$\alpha_{3s} = asin \left[sin\alpha_{th} \left(\frac{K_s h_{th}}{r_3} + 1 \right) \right]$$

where:

$$K_s = 0.39 - K_0$$

(3.41)

and:

$$K_0 = \frac{M_3^2 cos^2\beta_3 sin\beta_3}{1 - M_3^2 cos^2\beta_3}$$

3.5.3 Diffuser Performance

As part of the detail design process of the diffuser, a complete performance prediction is completed for every design iteration. This ensures that the diffuser design remains within the size and stall limits. Consequently, once the detail design process is complete, the full mean line performance prediction results for the design point are available. These results are subsequently recalled for display under the Diffuser Performance tab in the 1D App.

The diffuser performance prediction utilised in the 1D App is based on the work of Aungier (2000) and Japikse (1996). The applicable MATLAB® coding was initially developed by De Wet (2012). De Wet (2012) developed the diffuser performance code for a conventional radially vaned diffuser. Burger (2016) adapted this code for a crossover diffuser. This forms the basis of the diffuser performance prediction code for the 1D App.

Two significant alterations to this code are however incorporated in the 1D App. As explained in section 3.4.4, initial comparisons between the 1D and CFD results showed that the results did not correlate well for the majority of the 18 test compressors. Anomalies observed (amongst others) included a general over-prediction in compressor performance results. Additional investigation into the over-prediction of compressor performance by the 1D software revealed three contributing factors. The first one of these is impeller related and is explained in section 3.4.4.

The other two factors that contributed to the general over-prediction of the compressor performance are specifically connected to the diffuser performance prediction code. These include an under-prediction of the total diffuser exit temperature (T_{04}) (which affects the total-to-total isentropic efficiency), as well as an over-prediction in diffuser performance (due to an under-prediction of diffuser losses). In the case of the over-predicted diffuser performance, it was found that the original 1D code only determined the skin friction loss model for one channel (between two blades). Once the diffuser skin friction loss model was corrected to calculate $\bar{\omega}_{SF}$ for all the channels, diffuser performance was better aligned with CFD results. In terms of the under-predicted diffuser exit total temperature, it was found that a relationship between these errors and the impeller exit slip factor existed. Once these were quantified and implemented into the 1D App code, the results predicted by the modified 1D App compared well with the CFD results obtained. These anomalies are covered in detail in Chapter 5.

3.6 Overall Performance Analysis

Once the complete compressor design process is complete, the 1D App provides the user with the ability to create performance curves. These include curves for total-to-total isentropic efficiency (η_{TT}), total-to-total pressure ratio (PR_{TT}) and

total-to-static pressure ratio (PR_{TS}) (see Figure 3.11). The 1D App further allows the user to plot these performance curves for the entire compressor (1-4) or only for the impeller (1-2).

The 1D App allows the user to specify the range of mass flow rates (in kg/s) and rotational velocities (in RPM) to plot the performance curves. In such a case, the 1D App also displays the full performance data as text, but only for the original design point. In the event that the user requires a performance data plot at any other specific point ($\dot{m}$ and N), this option can be selected accordingly.
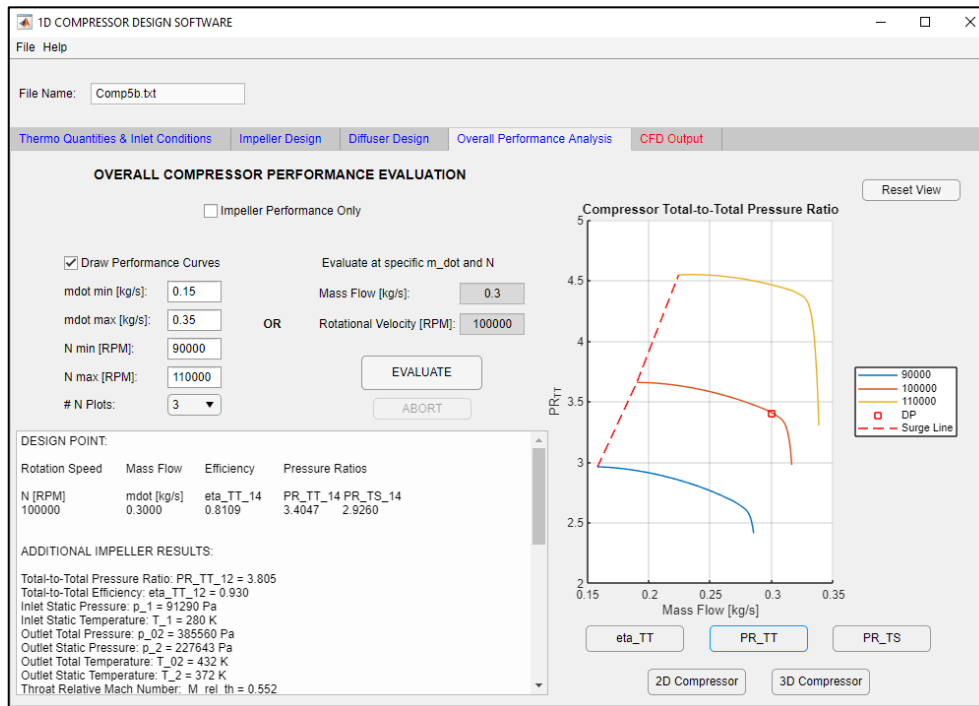
Figure 3.11: 1D App Performance Curves – $PR_{TT,1\text{-}4}$

Finally, under the Overall Performance Analysis section, the 1D App allows the user schematic views of the full compressor meridional curves (2D Compressor) and a 3D plot of the whole compressor (3D Compressor) (see Figure 3.12).
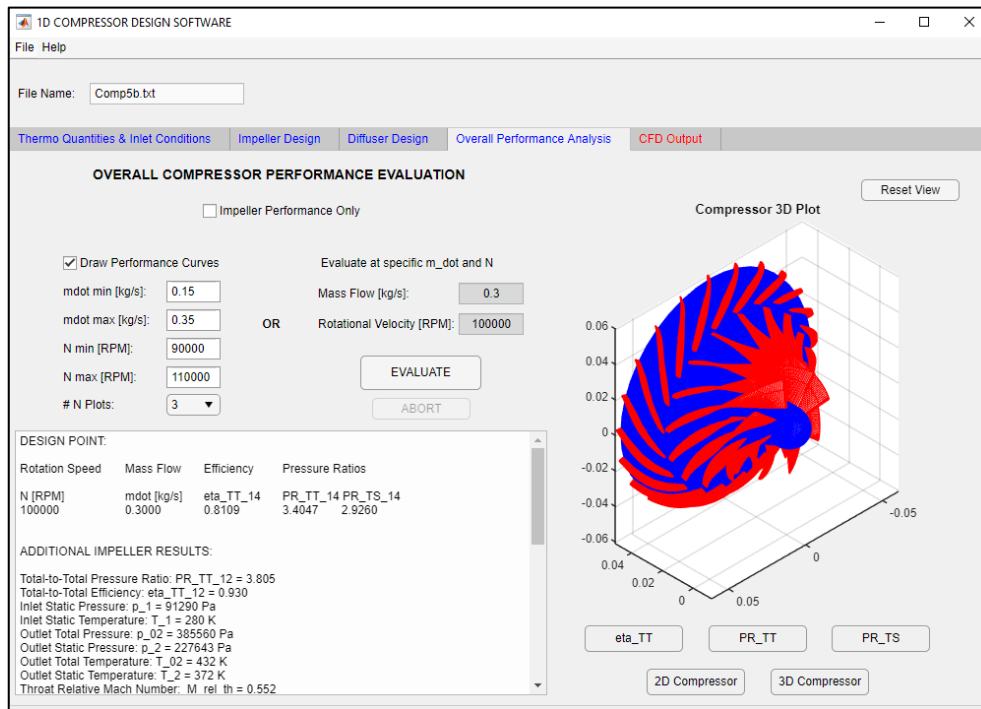
Figure 3.12: 1D App 3D Compressor Plot

3.7   CFD Output

The last stage of the 1D App compressor design process is to create a .geomTurbo file from the geometry of the designed compressor (see Figure 3.13).   This .geomTurbo file can be used for a 3D CFD analysis using Numeca/FINE™ Turbo (AutoGrid5™ for mesh generation). When creating the .geomTurbo file under the CFD Output tab of the 1D App, some basic impeller radius and axial geometric data is provided to the user. This data is required in FINE™/Turbo when defining the Solid Boundary Condition Definition.

Figure 3.13: 1D App CFD Output Tab

Chapter 4:

CFD Numerical Analysis

4.1   Introduction

To verify the validity and accuracy of the 1D App, 18 (+2) test compressors (see Appendix C for details) were designed using the 1D App. One of the 1D App features is the ability to create a .geomTurbo file from the geometry of the designed compressor. This .geomTurbo file can then be used for a 3D CFD analysis using Numeca/FINE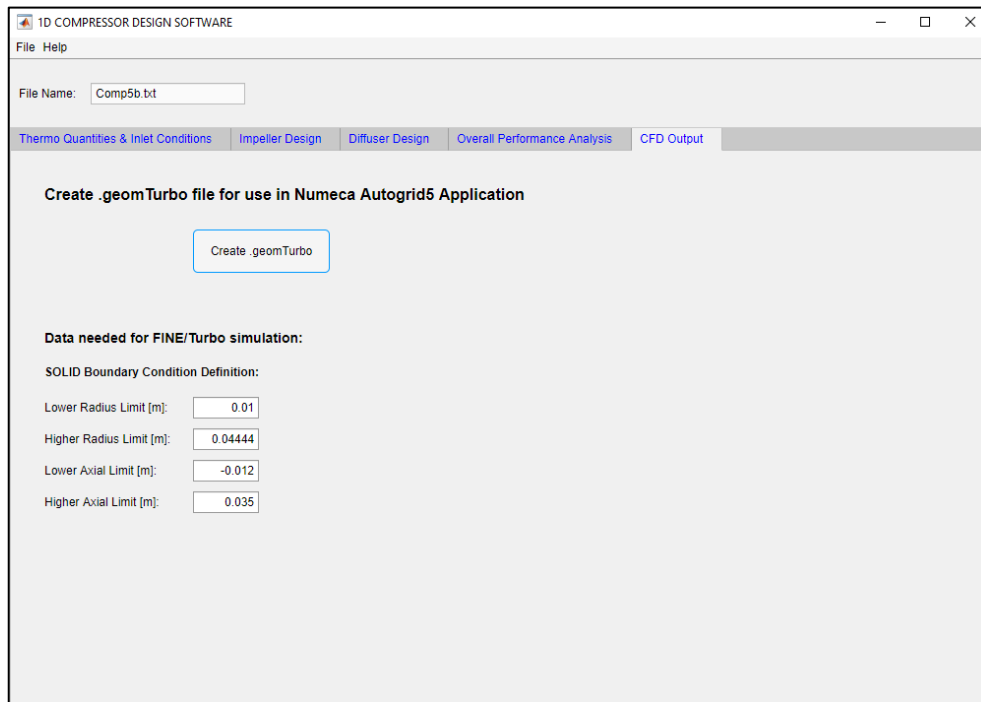™ Turbo. A CFD analysis was therefore completed for each of the 18 test compressors as a means of verifying the accuracy of the 1D App. Subsequent to updating the 1D App code, 2 more compressors were designed as final verification of the 1D App accuracy. These final 2 compressors were also fully analysed using Numeca/FINE™ Turbo. This chapter focusses on the generic procedure followed to conduct the full CFD analysis on a typical compressor designed using the 1D App.

4.2   Mesh Creation Using AutoGrid5™

Numeca/AutoGrid5™ is an automatic mesh generation tool used to generate meshes for a wide array of turbomachines, i.e. fans, axial compressors, centrifugal compressors and various turbine types. AutoGrid5™ allows various geometric file formats to be imported as an initial geometry definition. One such file format is a .geomTurbo file, which is a text file programmed with the required geometric data of the turbomachine for which a mesh needs to be generated. AutoGrid5™ requires the .geomTurbo file to be in a very specific format. Data include 2D arrays for the definition of the hub and shroud meridional curves, 3D arrays for the definition of the blade shapes (main and splitter), and the number of blades. The meshing process consists of three phases, namely the initial meridional mesh setup, blade-to-blade mesh setup and finally the complete 3D mesh definition. The .geomTurbo file created by the 1D App defines the impeller and diffuser separately. During the meshing process the impeller and diffuser mesh are created separately for the meridional setup and blade-to-blade setup phases. Once these are completed, the final 3D mesh creation is done for the complete compressor (impeller and diffuser).

4.2.1   Meridional Mesh Setup

AutoGrid5™ provides a 'Row Wizard' function which is used to import the geometry file, and also provides some default meshes for the various supported turbomachinery configurations. The default 'Centrifugal Impeller' and 'Centrifugal Diffuser' configurations were selected. At this point it was confirmed that the

number of blades for the impeller and diffuser, as well as the design rotational speed were imported correctly. Next it was verified that the tip gap, as designed in the 1D App for the specific compressor, was entered correctly. The required number of flow paths through the impeller and diffuser, which are basically the number of meridional stream surfaces stacked from hub to shroud between the blades were set to 73 and 59 for the impeller and diffuser respectively. The flow paths are illustrated by the red lines in Figure 4.1. It is clear from the figure that the flow paths (red lines) become denser towards the hub and shroud walls. This is to accurately capture the boundary layer effect.
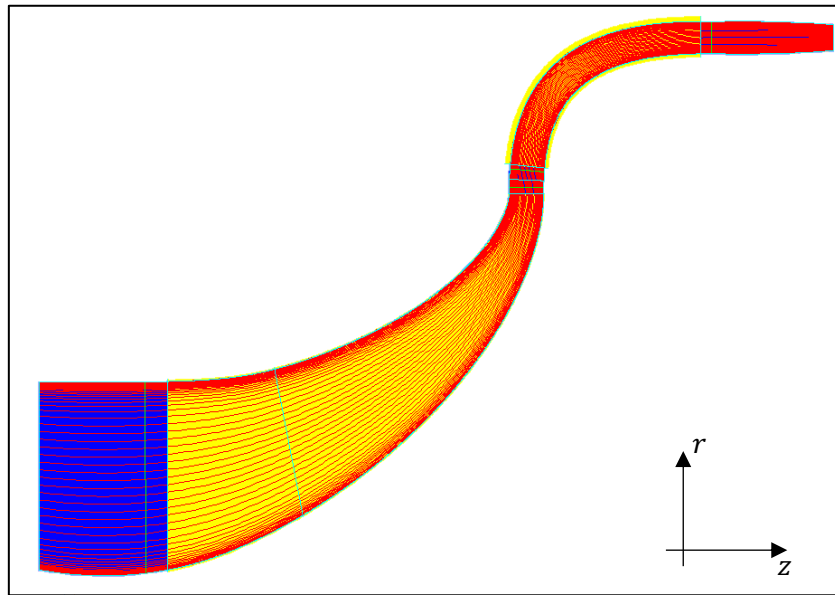

Figure 4.1: Meridional Mesh Flow Paths – Test Compressor 5a

The cell width at the walls were set to ensure that the correct y^+-values were obtained during the flow simulation. The Spalart-Allmaras turbulence model was used for flow simulation. This model typically requires $1 < y^+ < 10$. The required wall cell centre height (y_{wall}) is determined as follows:

$$y_{wall} = 6 \left(\frac{V_{ref}}{\nu} \right)^{-7/8} \left(\frac{L_{ref}}{2} \right)^{1/8} y^+ \qquad (4.1)$$

where reference values are taken at the mean impeller outlet. As an example, the wall cell width for Test Compressor 8 was calculated as 6.9×10^{-6} m, using a y^+ value of 6. The attained y^+ values for Compressor 8 for both the impeller and diffuser section are displayed in Figure 4.2 below. Note that these y^+ values were attained using the medium grid level. The effect of the grid level on the attained y^+ values are explained later in this chapter.
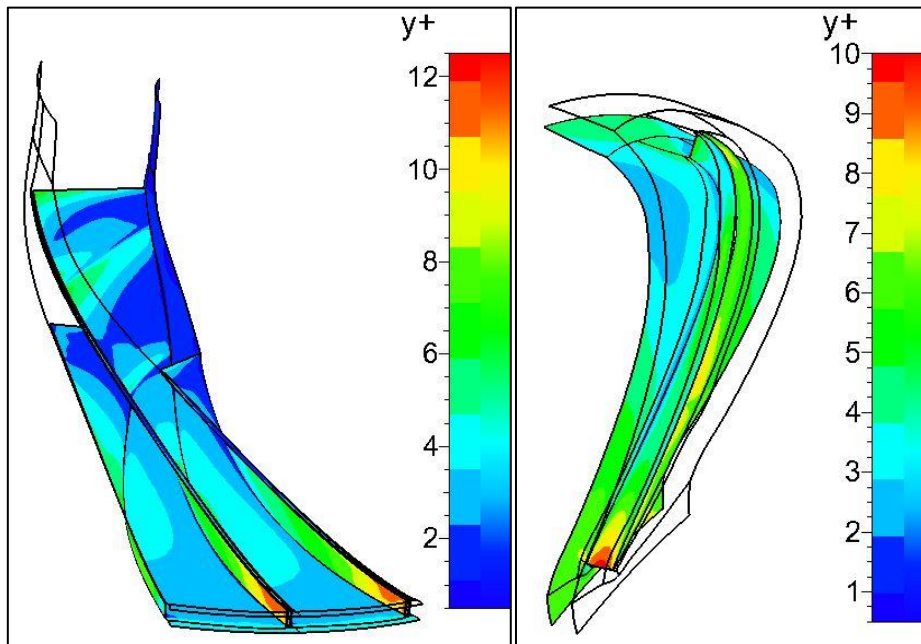
Figure 4.2: y^+ Values for Impeller and Diffuser – Compressor 8

4.2.2   Blade-to-blade Mesh Setup

<u>Impeller</u>

Most of the blade-to-blade meshing settings are pre-set due to the selection of the default 'Centrifugal Impeller' mesh under the 'Row Wizard'. The pre-set 'H&I' topology for both main and splitter blades, as well as 'H Topology' for the outlet for both main and splitter blades were used. To ensure proper capturing of the boundary layer, 'High Staggered Blade Optimisation' was selected for both main and splitter blades. A generic inlet and outlet angle for both the main and splitter blades are defined by the 'Inlet Type' and 'Outlet Type' setting. These were set to 'High Angle' and 'Normal' respectively for the main blade, and 'Normal' and 'Normal' respectively for the splitter blade. The biggest effort in creating a suitable blade-to-blade mesh is to select the appropriate number of grid points in the blade-to-blade domain. This process is typically a balance between having as few cells as possible to allow for shorter solver times, but still have enough cells to ensure proper mesh quality. As an example, the grid blocks for Compressor 8 are provided in Figure 4.3 below.
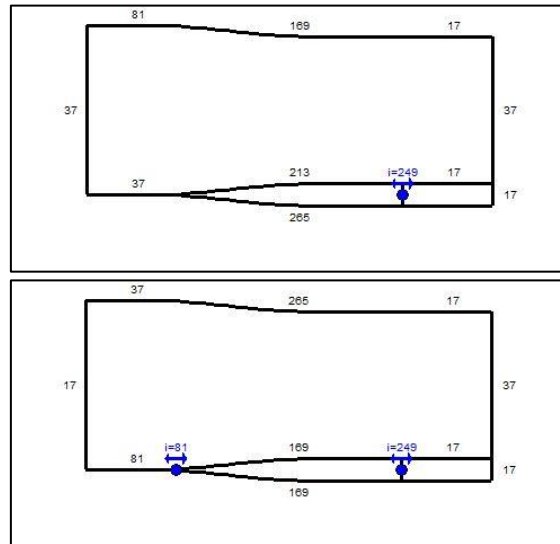
Figure 4.3: Impeller Main Blade and Splitter Blade Grid Points – Compressor 8

After generation of the 3D mesh, the Angular Deviation occasionally exceeded the maximum recommended value of 40° in a few cells. In such a case, the 'Intersection Quality' can be set to 'High' and the 3D mesh generation be re-started. This mode uses a more precise (albeit more time consuming) algorithm to determine the intersections between the blade and any axisymmetric flow path surface (Numeca International, 2018b).

Diffuser

The diffuser blade-to-blade topology was selected as "default". To ensure blade-to-blade mesh similarity, 'Matching Periodicity' was selected. As with the impeller, 'High Staggered Blade Optimisation' was selected to ensure proper boundary layer capture. The inlet and outlet blade angle type were set to 'Low Angle' and 'High Angle' respectively. Contrary to what was experienced during the blade-to-blade mesh setup for the impeller, the default diffuser grid point values were found to be suitable in most cases. The diffuser grid block for Compressor 8 is illustrated in Figure 4.4 below.
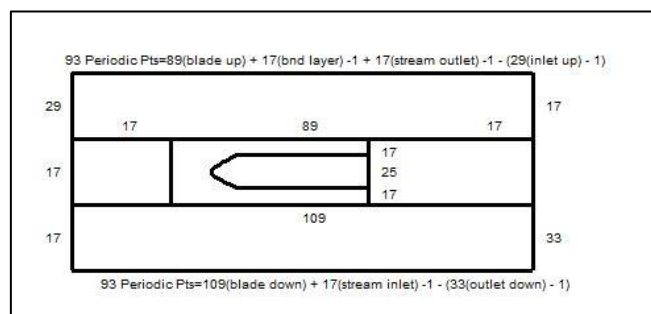

Figure 4.4: Diffuser Blade-to-Blade Grid Points – Compressor 8

4.2.3   3D Mesh Setup

Before the creation of the final 3D mesh for both the impeller and diffuser, the Mesh Optimisation Properties were set. De Villiers (2013) recommended values of 400 and 250 for the 'Optimisation Steps on Fine Grid' and 'Gaps and/or CHT Optimisation Steps' respectively. These values worked well for both the impeller and diffuser meshes. Under the 'Expert' option, the 'Skewness Control' and 'Skewness Control in Gaps' were set to 'Medium' and 'Full' respectively. These settings had a great impact on the general orthogonality of the mesh. 'Multigrid Acceleration' was enabled for both the impeller and the diffuser. This setting assisted in reducing the expansion ratios. Additionally, 'Multisplitter Control' was enabled for the impeller. An illustration of the final 3D mesh of Compressor 8 is provided in Figure 4.5.
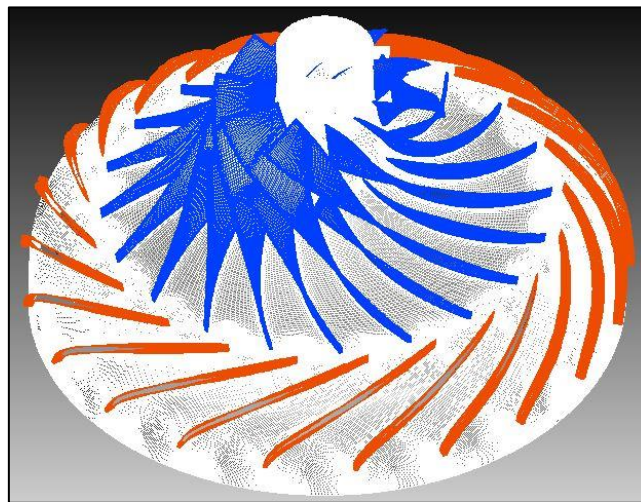
Figure 4.5: 3D Mesh – Compressor 8

4.2.4   Mesh Quality

Mesh quality is based on four parameters, namely Orthogonality (or Skewness), Aspect Ratio, Expansion Ratio and Angular Deviation (Numeca International, 2018b). These mesh quality parameters are defined as follows:

  i.   Orthogonality (or Skewness – which is more descriptive) give an indication of the skewness of a cell. It is determined as the minimum 2D internal angle between adjacent edges of a cell in a range of 0° to 90°. The recommended minimum value is 18°.

  ii.   The Aspect Ratio of a cell is the ratio of the length to width of a cell in the range 1 to 50000. The recommended maximum value is 2000.

    iii.   Expansion Ratio provides an indication of the rate at which the cell width of adjacent cells increases in a specific direction in the range 1 to 100. The recommended maximum value is 2.5.

    iv.   Angular Deviation is a 3D criterion and is an indication of the angular variation between two adjacent cells in all three cardinal directions in the range 0° to 180°. The recommended maximum value is 40°.

A summary of the mesh quality for Compressor 8 is given in Table 4.1 below. A small number of 'bad' cells were present in the test compressor meshes. These were negligibly small and had no negative effect on the convergence of any of the test compressor simulation points.

Table 4.1: Mesh Quality – Compressor 8

Quality Parameter	Requirement	Max Cells	Cells Outside	% 'Bad' Cells
Orthogonality	>18°		54	0.00065%
Aspect Ratio	<2000	8307968	0	0
Expansion Ratio	<2.5		144	0.00347%
Angular Deviation	<40°		0	0

4.2.5 Mesh Independence

Meshes were created in three grid levels using AutoGrid5™. These three grid levels were 000, 111 and 222 and increased in coarseness, with 000 being the finest and 222 being the coarsest. The 18 (+2) test compressors were all run on a medium (111) mesh. A mesh independence check was conducted on Compressor 1a by conducting a full FINE™/Turbo simulation on both medium (111) and fine (000) grid levels. The results of the compressor total-to-total isentropic efficiency ($\eta_{TT,1-4}$) and compressor total-to-total pressure ratio ($PR_{TT,1-4}$) are graphically illustrated in Figure 4.6.
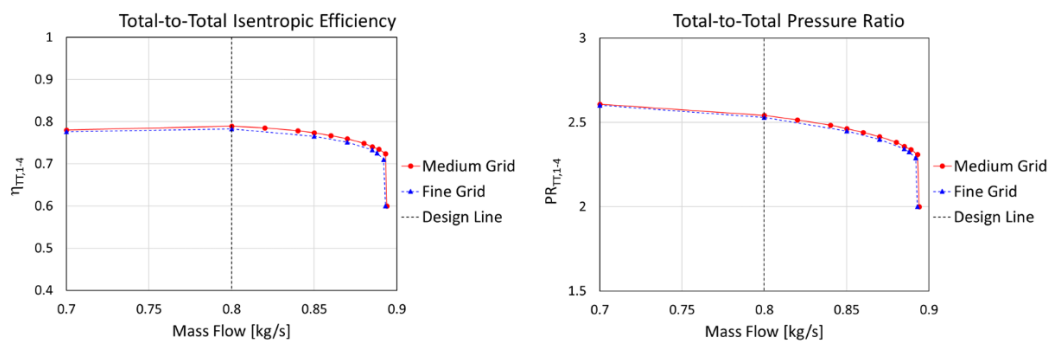

Figure 4.6: Medium vs Fine Mesh Comparison – Compressor 1a

The performance prediction difference at design conditions, as well as the choke prediction difference are provided in Table 4.2.

Table 4.2: Medium vs Fine Mesh Comparison – Compressor 1a

Fine Mesh # Cells	Medium Mesh # Cells	ΔChoke [%]	$\Delta\eta_{TT,1-4}$ [%]	$\Delta PR_{TT,1-4}$ [%]
2 697 306	361 350	0.52	0.65	0.47

The primary objective of this thesis is to develop a first order, quick turnaround application for the design of a radial or mixed flow compressor over a wide range of design operating conditions. The intention is therefore not to achieve a high level of accuracy in terms of performance prediction, but rather to achieve an initial approximation of the feasibility of a specific design. The differences encountered between the medium and fine meshes were deemed small enough to justify the use of the medium mesh for all the test compressors.

As mentioned earlier, the grid level used influenced the attained y^+ values. In the case of the medium grid level, the wall cell width was proportionally increased in comparison to the fine grid level. This had a direct impact on the attained y^+ values. Figure 4.7 below illustrates the difference in y^+ values for the impeller of Compressor 1a at medium and fine grid.
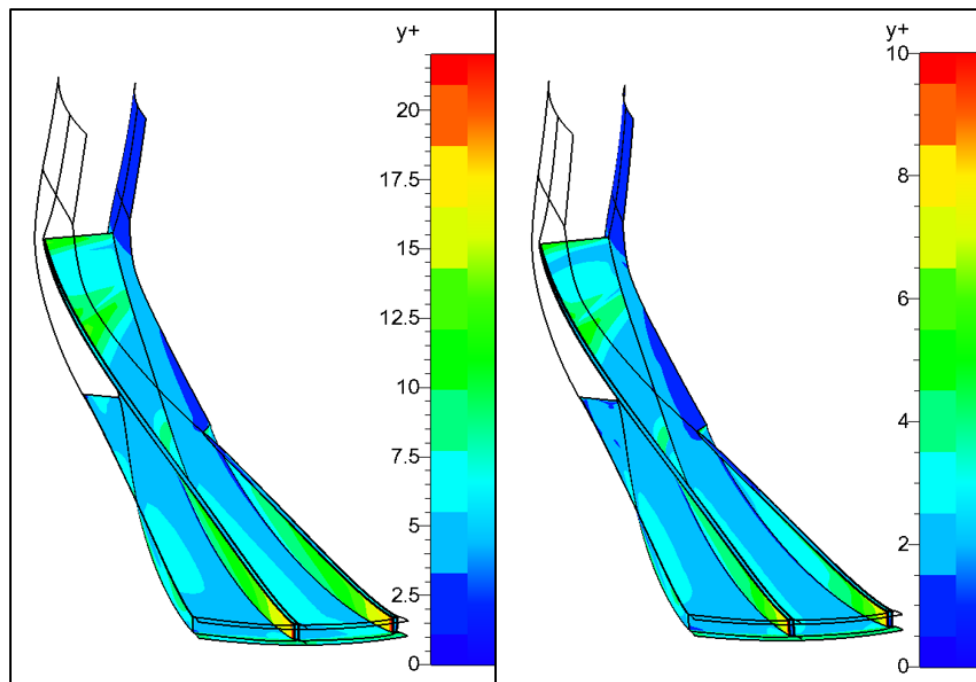

Figure 4.7: y^+ Distribution for Medium (left) and Fine (right) Grid Levels – Compressor 1a impeller

From Figure 4.7 it is clear that, in the case of the medium grid, a small area towards the blade trailing edge of the impeller presented y^+ values above the recommended maximum value of 10 (refer Spalart-Allmaras turbulence model). In the case of the fine mesh all the y^+ values are well inside the recommended maximum value. Having already ascertained that the performance prediction difference between the medium and fine grid levels were negligible, it was also deduced from the compared y^+ distributions that a slight overshoot in the small area as indicated also had a negligible effect on the final results.

4.3 FINE™/Turbo Setup

Numeca/FINE™ Turbo was used as the 3D flow simulation tool. The mesh generated in AutoGrid5™ was imported into FINE™/Turbo as the flow domain. Details regarding the flow simulation setup are discussed here.

4.3.1 Fluid and Flow Model

Air as a calorically perfect gas was selected as the fluid for all simulations. Various previous studies (including Krige (2013), Kock (2017)) compared results of air as a real gas to air as a prefect gas. They all found negligible differences in results. This is also supported by general compressibility charts. Selecting air as a real gas also increased computational time by 20 to 25% compared to air as a perfect gas (Numeca International, 2018b). For these reasons, other fluid options were not investigated. Viscosity was based on the Sutherland approximation, and the heat conduction was based on the Prandtl approximation. The fluid properties of air as a perfect gas are depicted in Table 4.3.

Table 4.3: Properties of Air as a Perfect Gas

Fluid Property	Value
Specific Heat (c_p)	1006 J/kg·K
Specific Heat Ratio (γ)	1.4
Prandtl Number	0.708
Dynamic Viscosity (μ) at 293.11K	1.716 x 10^{-5} Pa·s
Sutherland Temperature	110.555 K

The Time Configuration of the flow model was selected as 'Steady' state. 'Turbulent Navier-Stokes' was selected as the mathematical model, with 'Spalart-Allmaras' being selected as the turbulence model. This model is a one-equation model and provides economical computations in boundary layers, especially for external aerodynamic scenarios where adverse pressure gradients are typically present (Versteeg and Malalasekera, 2007). Kock (2017) compared the Spalart-

Allmaras turbulence model with the SST and k-ε models. He found that all three these models provided similar results. The Spalart-Allmaras model was selected due to its smaller computational time and memory requirement and due to its preference for use with aerofoil type applications, i.e. turbomachinery (Versteeg and Malalasekera, 2007; Spalart and Allmaras, 1992). The model is a one-equation model (hence the lower memory requirement) with the model constants selected to provide good performance in boundary layers with adverse pressure gradients present.

4.3.2 Boundary Conditions

The general methodology followed for all the test compressors was to create a performance curve by completing simulation runs at the design speed and at various mass flow rates. This was done by fixing the inlet conditions and varying the outlet mass flow rate throughout the operating range.

Inlet

To ensure standard environmental test conditions for all the test compressors, the inlet conditions were kept constant at ISA values. This was achieved by selecting the 'Total Quantities Imposed' option under the 'INLET' tab. The 'Velocity direction (V extrapolated)' option was selected, and the values were entered as presented in Table 4.4.

Table 4.4: Inlet Boundary Conditions

$V_r/\lvert V \rvert$	0
$V_t/\lvert V \rvert$	0
$V_z/\lvert V \rvert$	1
Absolute Total Pressure [Pa]	101325
Absolute Total Temperature [K]	288
Turbulent Viscosity [m^2/s]	0.0001

Outlet

The various operating points of each compressor were determined by altering the mass flow rate at the outlet. A locus of these operating points formed the operating curve for the specific compressor at its design speed. 'Mass Flow Imposed' was selected under the 'OUTLET' boundary condition tab. The 'Pressure Adaptation' option was selected, with the 'mass-flow' selected per run. A generic 'Initial Pressure' of 160000 Pa was selected for all the runs, with the 'Backflow Control' also activated. This selection was made to control the exit stagnation temperature distribution, especially in the event that some flow re-enter through the outlet boundary (Numeca International, 2018a). The choke mass flow rate was achieved

at the last point where inlet and outlet mass flow rate converged. Beyond this mass flow rate, the inlet and outlet mass flow rate maintained a constant difference, while the overall efficiency and pressure ratio continued a steady decrease.

Solid

The Solid boundary condition defines the rotation of the various compressor parts, namely the impeller hub, shroud and blades, as well as the diffuser hub, shroud and blades. For the impeller hub, the 'Adiabatic', 'Area Defined Rotation Speed' was selected. This option allows the selection of a specific area zone of the hub to be defined for rotation in the meridional sense, irrespective of the mesh structure (Numeca International, 2018a). It is however important for this zone to be defined correctly in terms of its geometric extremities. For this reason, the 1D App provides the values for this zone when the .geomTurbo file is created under the 'CFD Output' tab (see Figure 3.13). These values were separately defined for each test compressor. An example is provided in Table 4.5 below.

Table 4.5: Solid Impeller Hub Boundary Conditions – Compressor 8

Rotation Speed 1 [RPM]	0
Rotation Speed 2 [RPM]	60000
Lower Radius Limit [m]	0.015
Higher Radius Limit [m]	0.06938
Lower Axial Limit [m]	-0.018
Higher Axial Limit [m]	0.047

The rest of the solid groups were all defined as 'Adiabatic', 'Constant Rotation Speed'. With the exception of the impeller blade group, which was set to the design rotation speed, the other solid groups (impeller shroud, diffuser shroud, hub and blades) were set to 0 RPM.

4.3.3 Computational settings

Numerical Model

Grid level 111 was used for the simulation of all the test compressors. 'Coarse Grid Initialisation' was selected, which allowed the solution to run the first 100 iterations on the coarser grid level and use this result as an initial solution for the next grid level.

Initial Solution

The initial solution option specifically dedicated to turbomachinery were selected. A constant estimated static pressure for both impeller inlet and rotor-stator

boundary (between impeller and diffuser) were defined. Generic values of 95000 Pa and 160000 Pa were used respectively.

Control Variables

The maximum number of iterations were set to 10000, with a convergence criterion of -6 specified. The solution often reached the conversion criteria well before 10000 iterations, in which case the solution terminated automatically. Solutions were saved to the output file every 200 iterations. The solver was set to double precision for grid level 111. The memory requirements typically varied between 370 and 420 MB.

Convergence

FINE™/Turbo provides the option to monitor various variables during the simulation process. The variables monitored were the global residual, inlet and outlet mass flow, efficiency and pressure ratio. Convergence were achieved when:

    i.   The global residual decreased by more than three orders of magnitude.

    ii.   The inlet and outlet mass flow rate converged to within at least 0.5% of each other.

    iii.   The efficiency and pressure ratio results have stabilised.

As an example, the global residual and mass flow convergence for Compressor 8 at 60000 RPM and 0.4 kg/s are provided in Figures 4.8 and 4.9 below.
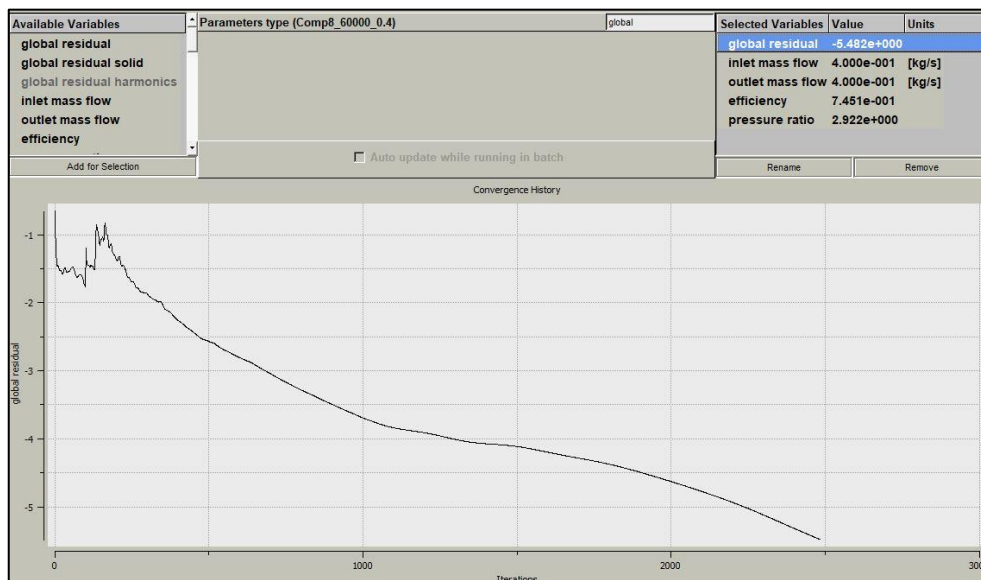

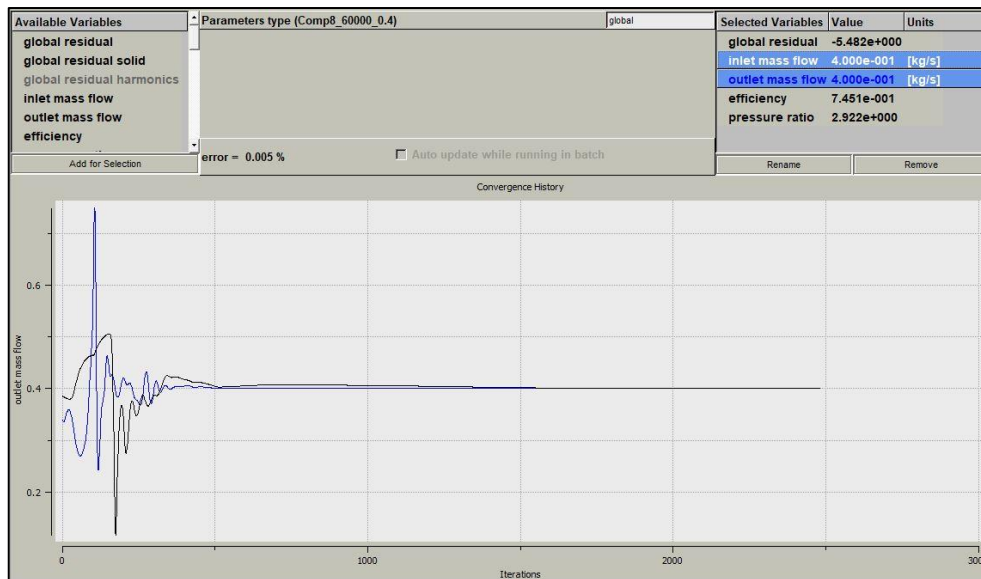Figure 4.8: Global Residual – Compressor 8 (60000 RPM / 0.4 kg/s)

Figure 4.9: Mass Flow Convergence – Compressor 8 (60000 RPM / 0.4 kg/s)

4.4 Post Processing

Post processing was conducted using Numeca CFView™. CFView™ provides various methods to visualise the performance and results of each individual FINE™/Turbo run by analysing the .run file created after each simulation. CFView™ was used to determine mean pressures (total and static) and temperatures (total and static) in order to predict performance of the various compressor components and compare it to the 1D mean line code results. Colour schematics (e.g. y$^+$ schematic) are also produced in CFView™.

4.5 Summary

3D CFD analysis of all the test compressors were conducted using Numeca/FINE™ Turbo CFD software. This was done to validate the results obtained by the 1D App. The setup explained in this chapter was used for all the test points of all the test compressors.

Chapter 5:

Results Discussion

5.1   Introduction

As mentioned before, the primary objective of this thesis is to develop a first order, quick turnaround application for the design of a micro gas turbine compressor. The intention is to achieve an initial approximation of the feasibility of a specific design. Design optimisation would typically still have to be conducted by another means.

The 1D App was developed with these basic requirements in mind. However, after comparison of the initial performance prediction results of the 18 test compressors, it was clear that the accuracy of the initial 1D code was unsatisfactory when compared to CFD results, even as a first order design tool. Choke prediction and isentropic efficiency prediction were especially unsatisfactory. Performance prediction differences in excess of 20% were observed. These performance prediction anomalies necessitated deeper investigation and scrutinization of specific performance parameters at the various compressor stations. This was done in an attempt to narrow down the anomalies to specific components and regions inside the compressor. Details about these findings are discussed in this chapter.

5.2   Alternative Flow Parameter

The 18 test compressors designed using the 1D App and verified by CFD analysis covered a wide range of rotational velocities, mass flow rates and impeller meridional exit angles (see Appendix C). These 18 test compressors were arranged from largest (geometrically) and slowest (rotational velocity) to smallest and fastest. It was further observed that the design tip flow coefficient (ϕ_2) roughly increased in the same order, while the impeller exit slip factor (σ_s) roughly decreased in the same order.

The various performance prediction anomalies observed were compared against the design tip flow coefficient (ϕ_2) and the impeller exit slip factor (σ_s). Although, in certain flow regimes, relationships between some of the anomalies and these two parameters were observed (details to follow in the next sections), all the observed anomalies could not be linked to these two parameters alone. During the analysis process it became clear that an alternative flow parameter needed to be defined that could better quantify the test compressor design points. The intention was for this alternative flow parameter to be used to compare the various test compressors and then analyse the observed performance anomalies between the 1D code and CFD against this alternative flow parameter.

During the analysis process of the various performance anomalies, it became clear that four main compressor parameters influenced the observed performance anomalies. These were the design mass flow rate ($\dot{m}$), the design rotational velocity (ω), the meridional exit angle (α_{C2}) and the impeller exit slip factor (σ_s). Due to this observation, it was decided to investigate an alternative flow parameter which incorporate these four parameters. As was observed with the impeller exit slip factor (σ_s) it was expected that the alternative flow parameter would decrease from the slower, larger compressors to the faster, smaller compressors. With this in mind, by considering dimensional analysis it was anticipated that the alternative flow parameter would take the form:

$$\psi = f\left(\sigma_s^a, \dot{m}^b, (sin\alpha_{C2})^c, \frac{1}{\omega^d}\right) \tag{5.1}$$

The power values (a, b, c, and d) were determined by analysing the alternate flow parameter for the 18 test compressors against the observed performance prediction anomalies. During this analysis process, the large numerical values of ω relative to the other parameters were problematic. For this reason, a logarithmic function of ω was introduced into the formula for the alternative flow parameter. The analysis yielded the following formula:

$$\psi = \frac{\sigma_s\left(\dot{m}/\dot{m}_{ref}\right)^{\sigma_s^2}(sin\alpha_{C2})^{3.5}}{ln\left(\omega/\omega_{ref}\right)} \tag{5.2}$$

where:
ψ Alternative flow parameter
σ_s Impeller exit slip factor
$\dot{m}$ Design mass flow rate [kg/s]
$\dot{m}_{ref}$ Reference mass flow rate = 1 kg/s
α_{C2} Impeller meridional exit angle [rad]
ω Rotational velocity [rad/s]
ω_{ref} Reference rotational velocity = 1 rad/s

Due to the fact that $\dot{m}$ and ω were not dimensionless quantities, these values had to be divided by reference values to ensure that the alternative flow parameter was a dimensionless quantity. In both cases a value of 1 was selected as reference value. The application and use of the alternate flow parameter is explained later in this chapter.

5.3 Choke Prediction Anomaly

Appendix D shows the performance prediction comparison plots of the original 1D code, the CFD results and the updated 1D code. From these plots it is clear that the choke mass flow rate is over-predicted for the slower, larger compressors, while the choke mass flow rate is under-predicted for the faster, smaller compressors. Initial observations indicated that there might be a relationship between choke prediction and the tip flow coefficient and impeller exit slip factor.

5.3.1 Choke Anomaly Analysis

The 1D code choke mass flow prediction was initially only compared to the impeller exit slip factor. Although a clear relationship was observed for smaller, faster compressors, this comparison did not provide good results throughout the test compressor range. Prior to conducting further analysis, it was prudent to firstly ascertain which component (impeller or diffuser) contributed to the choke prediction anomaly. The CFD analysis of the test compressors assisted in this regard. It was observed that the under-prediction of choke for the smaller, faster compressors was due to the impeller 1D code not predicting choke correctly. On the other hand, in the case of the slower, larger compressors it was observed that the CFD analysis indicated choke in the diffuser throat section which was not predicted early enough by the 1D code.

A clear distinction in choke prediction was thus observed between the smaller, faster and the bigger, slower compressors. To quantify this distinction, the choke prediction results were firstly compared to the design tip flow coefficient (ϕ_2) of each compressor. It was observed that all compressors with $\phi_2 > 0.34$ presented an under-prediction of the choke mass flow rate by the original 1D code. On the other hand, compressors with $\phi_2 < 0.34$ presented an over-prediction in choke mass flow rate. The compressors in these two regions were subsequently analysed separately.

5.3.2 Choke Prediction for Higher Flow Compressors

The under-prediction of the choke mass flow rate for the smaller, faster compressors was attributed to the prediction of choke for the impeller in the 1D code. Due to the specific choice of compressor sequencing (large and slow to small and fast – see Appendix C), a very interesting phenomenon was observed. In the range $\phi_2 > 0.34$, the choke prediction roughly moved from a lower limit to an upper limit. After further analysis, it became apparent that the impeller exit slip factor of these test compressors also seem to generally decrease in the same order. It thus seemed that there existed a relationship between impeller exit slip factor and choke prediction in this flow range.

In order to explore this relationship further, it is first important to understand the mechanism of choke prediction in the 1D code. Choke prediction in the mean line code is based on the following formula (Aungier, 2000):

$$X = 11 - 10\,\frac{C_r A_{th}}{A^*} \qquad (5.3)$$

In Equation 5.3, X provides an indication of how close the critical area comes to the actual throat area. Choke losses are incurred if the flow critical area approaches the throat area. It was found that if the numerical value of the first term of Equation 5.3 is changed, the position of choke (the mass flow where choke occurred) can be controlled. For each of the test compressors in the range $\phi_2 > 0.34$ the first term in this equation was adjusted until the occurrence of choke was comparable with what was observed in the CFD analysis. These updated choke formula first terms were then subsequently compared to the impeller exit slip factors of the same compressors to establish the relationship between these factors. The graphical results are provided in Figure 5.1 below:
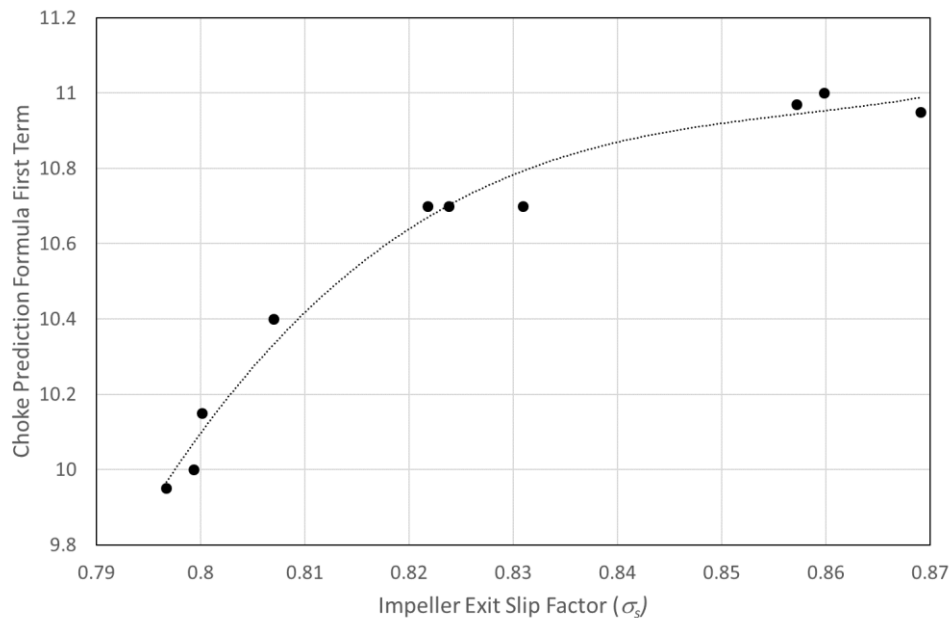

Figure 5.1: Choke Prediction Relationship – $\phi_2 > 0.34$

From the above plot it is evident that a relationship between slip factor and choke prediction existed for the test compressors with a design tip flow coefficient $\phi_2 > 0.34$. A 3rd order polynomial trend line was added to the data and this formula was implemented in the 1D App code to improve choke prediction. Apart from Compressor 4b, significantly better choke prediction was observed after implementation of the updated choke prediction formula. For all the test compressors, choke mass flow was predicted to within 3.5% of the choke mass

flow rate predicted by CFD. Details of this are provided in Table 5.1. Detailed performance curves are also provided in Appendix D.

Table 5.1: Choke Prediction Results – $\phi_2 > 0.34$

Compressor Name	Initial 1D Code Choke Prediction difference [%]	Updated 1D Code Choke Prediction difference [%]
Compressor 4a	-3.06	-1.02
Compressor 4b	0.00	1.49
Compressor 4c	-1.47	-1.03
Compressor 5a	-10.98	0.41
Compressor 5b	-10.82	-0.41
Compressor 5c	-10.66	-3.48
Compressor 6a	-30.20	0.20
Compressor 6b	-26.98	1.22
Compressor 6c	-13.18	2.33
Compressor 7	-39.88	-0.61

5.3.3 Choke Prediction for Lower Flow Compressors

For the test compressors with a tip flow coefficient $\phi_2 < 0.34$, the CFD analysis indicated choke in the diffuser throat section which was not predicted early enough by the 1D code. Figure 5.2 shows the absolute and relative Mach number meridional distribution for Compressor 2c at a mass flow rate of 0.515 kg/s. By studying these absolute and relative Mach number schematics it is clear that choke was developing in the diffuser throat section.
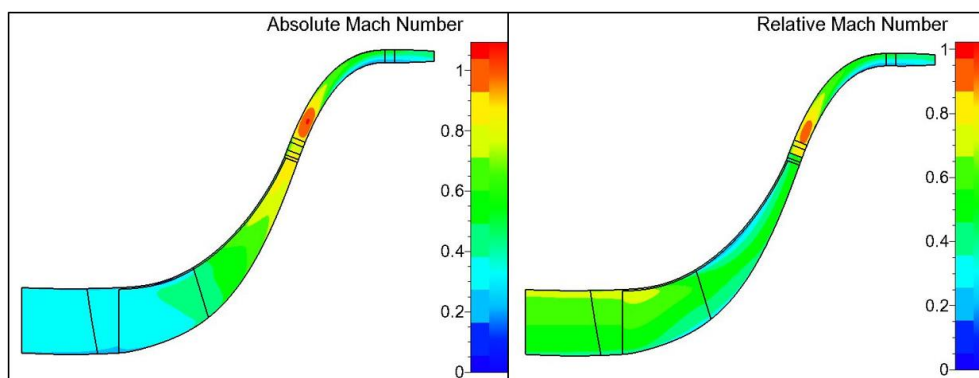

Figure 5.2: Diffuser Choke Development – Compressor 2c at 0.515 kg/s

With the choke prediction anomalies for the larger, slower compressors being attributed to the diffuser, it was anticipated that choke prediction for these

compressors were probably not linked to the impeller exit slip factor. In this case the choke prediction anomaly was compared to the alternative flow parameter (ψ) (see Section 5.2).

For each of the test compressors in the range $\phi_2 < 0.34$ the first term in the 1D code choke prediction equation (Equation 5.3) was again edited until the onset of choke was comparable to what was observed in the CFD analysis. These updated choke formula terms were compared with the alternative flow parameter (ψ) to establish the relationship between these factors. The graphical results are provided in Figure 5.3 below:
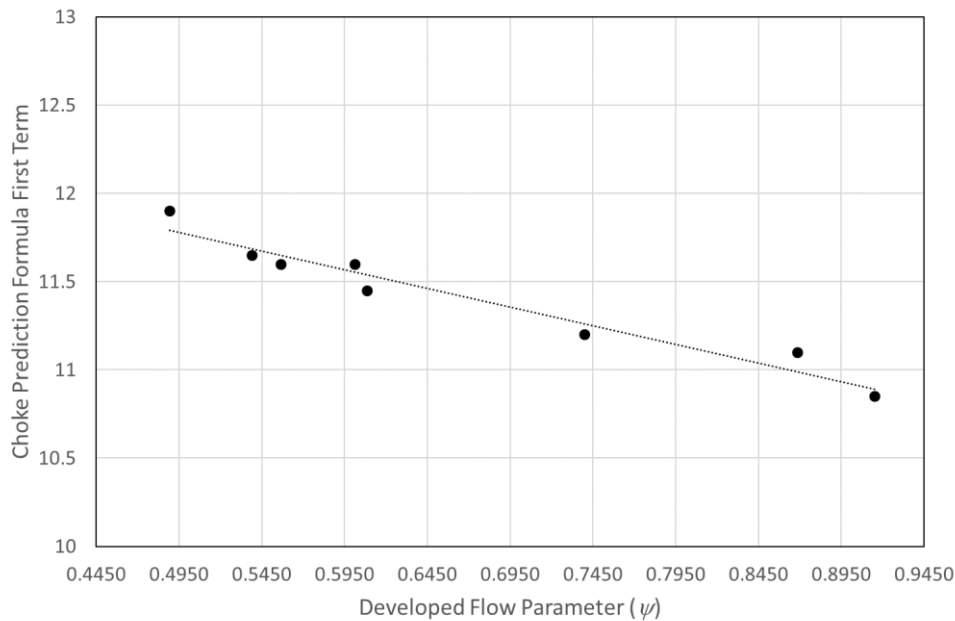

Figure 5.3: Choke Prediction Comparison – $\phi_2 < 0.34$

From the above plot there seems to be a linear relationship between the alternative flow parameter (ψ) and choke prediction for the test compressors with a tip flow coefficient $\phi_2 < 0.34$. A linear trend line was added to the data and this formula was implemented in the 1D App. Significantly better choke prediction was observed after implementation of the updated choke prediction formula. The choke mass flow rate was predicted to within 5% of the actual choke mass flow rate for all the test compressors in this range. Details of this are provided in Table 5.2. Detailed performance curves are also provided in Appendix D.

Table 5.2: Choke Prediction Results – $\phi_2 < 0.34$

Compressor Name	Initial 1D Code Choke Prediction difference [%]	Updated 1D Code Choke Prediction difference [%]
Compressor 1a	-4.54	-3.25
Compressor 1b	6.88	4.97
Compressor 1c	7.85	-1.82
Compressor 2a	12.87	-1.47
Compressor 2b	18.04	-0.97
Compressor 2c	26.23	1.90
Compressor 3a	28.72	0.74
Compressor 3b	17.24	-1.30

5.4   Compressor Performance Prediction Anomaly

Comparison of the initial 1D performance prediction results against the CFD results for the range of 18 test compressors indicated a consistent over-prediction of compressor performance ($\eta_{TT,1-4}$ and $PR_{TT,1-4}$) at design point. To narrow down these potential anomalies, predicted performance parameters were compared at the various stations inside the test compressors (i.e. impeller exit (station 2) and diffuser exit (station 4)). Three factors were identified that contributed to the overall compressor over-prediction anomaly.   These are discussed in the following sections.

5.4.1   Impeller Performance Prediction Anomaly

During analysis and comparison of the test compressors it was found that impeller exit static pressures were consistently over-predicted by the 1D code. This over-prediction did not have a major influence on the total performance over-prediction of the various test compressors (this was mainly attributed to the diffuser – see next section) but was still analysed and implemented.

As was the case with choke prediction (see previous section), it was found that the impeller exit static pressure (p_2) over-prediction anomaly needed to be analysed separately for $\phi_2 < 0.34$ and $\phi_2 > 0.34$.

Impeller Exit Static Pressure Prediction for Lower Flow Compressors

As was the case with choke prediction, the impeller exit static pressure anomaly for the lower flow test compressors ($\phi_2 < 0.34$) was found to be a function of the alternative flow parameter defined in Equation 5.2.   For each of the test

compressors in the range $\phi_2 < 0.34$, the impeller exit static pressure over-prediction ratio ($p_{2_{1D}}/p_{2_{CFD}}$) was plotted against the flow parameter (ψ).
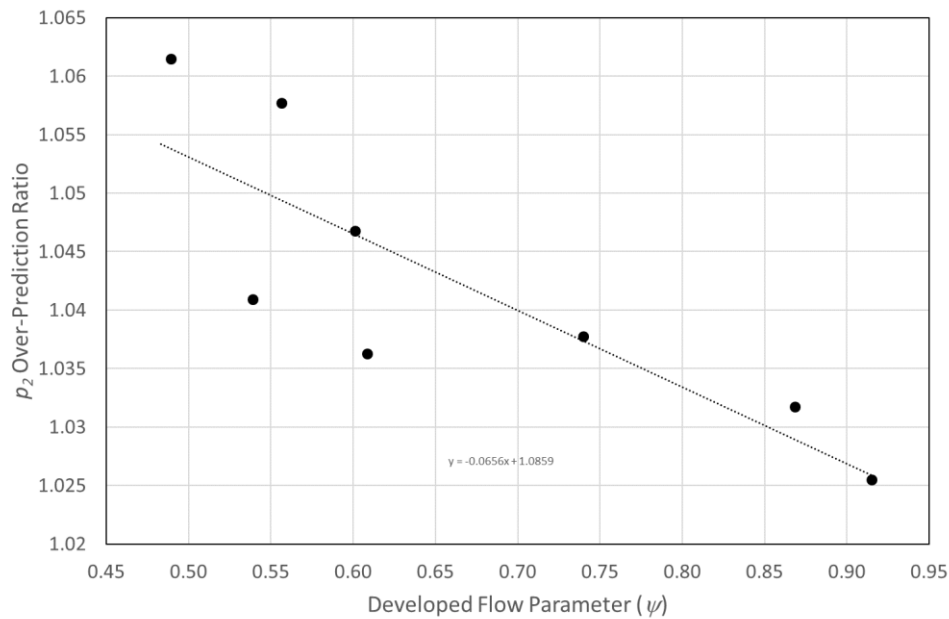

Figure 5.4: p_2 Prediction Comparison – $\phi_2 < 0.34$

From Figure 5.4 it is clear that p_2 was over-predicted for all the test compressors considered (over-prediction ratio > 1). Although the data points were somewhat scattered, there seemed to be a linear relationship between the alternative flow parameter (ψ) and the impeller exit static pressure over-prediction ratio ($p_{2_{1D}}/p_{2_{CFD}}$) for the test compressors with a tip flow coefficient $\phi_2 < 0.34$. The contribution of the p_2 over-prediction anomaly was however small in comparison to other factors. The effect was however still considered and implemented. A linear trend line was added to the data and implemented in the 1D App code. The effect of this update was not analysed in isolation but is presented later in this chapter as part of the combined performance update results.

Impeller Exit Static Pressure Prediction for Higher Flow Compressors

As was the case with choke prediction, the impeller exit static pressure deviation for the higher flow test compressors ($\phi_2 > 0.34$) was found to be a function of the impeller exit slip factor (σ_s). For each of the test compressors in the range $\phi_2 > 0.34$, the impeller exit static pressure over-prediction ratio ($p_{2_{1D}}/p_{2_{CFD}}$) was plotted against the impeller exit slip factor (σ_s).
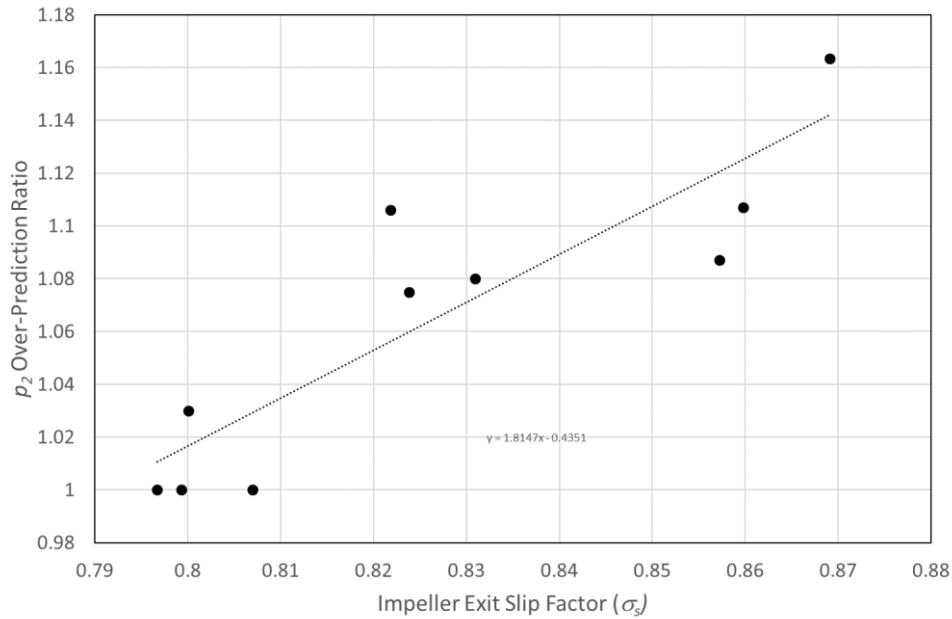
Figure 5.5: p_2 Prediction Comparison – $\phi_2 > 0.34$

From Figure 5.5 it is clear that p_2 is either correctly predicted or over-predicted for all the test compressors considered (over-prediction ratio ≥ 1). Although the data points were scattered, there seemed to be a linear relationship between the impeller exit slip factor (σ_s) and the impeller exit static pressure over-prediction ratio ($p_{2_{1D}}/p_{2_{CFD}}$) for the test compressors with a tip flow coefficient $\phi_2 > 0.34$. Although the effect was small, it was still considered and implemented. A linear trend line was added to the data and implemented in the 1D App code. The effect of this update was again not analysed in isolation but are presented later in this chapter as part of the combined performance update results.

5.4.2   Diffuser Performance Prediction Anomaly

The general performance over-prediction by the original 1D code necessitated the analysis of performance parameters of the individual compressor components. The contribution of the impeller 1D code towards the total performance anomalies was discussed in the previous section. Analysis of the diffuser exit parameters (station 4) indicated that the predicted performance of the diffuser in the 1D code differed significantly from the CFD results for all 18 test compressors. Two main problem areas were identified, namely an under-prediction of the skin friction loss ($\overline{\omega}_{SF}$) inside the diffuser, as well as an under-prediction of the diffuser total exit temperature (T_{04}). These are explained individually in the following paragraphs.

Diffuser Skin Friction Loss Anomaly

The 1D mean line code performance prediction used in the 1D App consists of empirical loss models in both the impeller and diffuser. One of the losses being predicted in the diffuser is the skin friction loss ($\overline{\omega}_{SF}$). The formulas used in the 1D code for this loss prediction was originally inherited from a previously developed 1D MATLAB® code for crossover diffusers.

Analysis of the CFD data at the various compressor stations (impeller inlet and exit, vaneless gap, diffuser blade inlet and diffuser exit) indicated that the 1D code consistently over-predicted the overall performance of the crossover diffuser. The 1D code thus consistently under-predicted the losses arising in the diffuser. After some deeper analysis of the various loss coefficients, it was observed that the skin friction loss was only calculated for a single channel in the diffuser. Once the skin friction loss was multiplied by the number of channels (number of blades) the diffuser performance in general compared considerably better with the CFD results. This correction was therefore introduced in the updated 1D App code.

Diffuser Exit Total Temperature Under-Prediction Anomaly

Analysis of the CFD results at the various compressor stations further indicated that the 1D code consistently under-predicted the diffuser (and compressor) exit total temperature (T_{04}). This had a major influence on the compressor total-to-total efficiency ($\eta_{TT,1-4}$) prediction. The under-predicted exit total temperature resulted in a significantly over-predicted total-to-total efficiency (refer Equation 2.23) across the entire test compressor range. It was found that the under-prediction seemed to be a function of impeller exit slip factor (σ_s), albeit for the entire compressor range, regardless of tip flow coefficient. For each of the test compressors the diffuser exit total temperature under-prediction ratio ($T_{04_{1D}}/T_{04_{CFD}}$) was plotted against the impeller exit slip factor (σ_s).
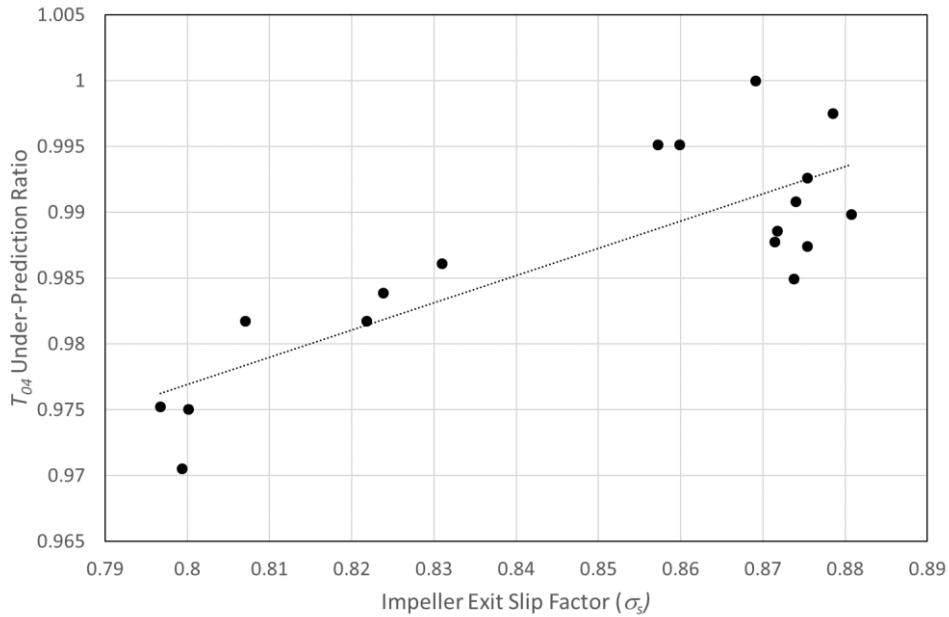
Figure 5.6: T_{04} Prediction Comparison

From Figure 5.6 it is clear that T_{04} was either correctly predicted or under-predicted for all the test compressors considered (under-prediction ratio ≤ 1). Although the data points were scattered, there seems to be a linear relationship between the impeller exit slip factor (σ_s) and the compressor exit total temperature under-prediction ratio ($T_{04_{1D}}/T_{04_{CFD}}$) for the full range of test compressors. A linear trend line was added to the data and this formula was implemented in the 1D App code. The effect of this update was not analysed in isolation but is presented in the next section as part of the combined performance update results.

5.4.3   Updated Performance Prediction Results

Significantly better performance prediction results were observed after implementation of the 1D code performance updates. Performance prediction results were evaluated at the design mass flow rate and design rotational velocity. The only exception to this was Compressor 7, where the original 1D code already predicted the onset of choke at the design mass flow rate. Therefore, performance results for Compressor 7 were evaluated at 95.4% (the next lower analysed CFD test point) of design mass flow rate. Details of these performance results are provided in Table 5.3. Detailed performance curves are also provided in Appendix D.

Table 5.3: Performance Prediction Results for 18 Test Compressors

Compressor Name	Initial 1D Code		Updated 1D Code	
	$\eta_{TT,1-4}$ difference [%]	$PR_{TT,1-4}$ difference [%]	$\eta_{TT,1-4}$ difference [%]	$PR_{TT,1-4}$ difference [%]
Compressor 1a	11.64	6.62	0.81	-0.72
Compressor 1b	12.49	8.62	1.40	0.75
Compressor 1c	13.02	10.33	1.57	1.37
Compressor 2a	12.36	9.97	0.25	0.29
Compressor 2b	11.32	10.13	-0.92	-0.05
Compressor 2c	13.07	14.22	1.03	3.52
Compressor 3a	11.68	11.62	-1.44	-2.11
Compressor 3b	15.09	16.78	0.35	-0.34
Compressor 4a	10.92	10.81	-0.91	0.73
Compressor 4b	11.31	12.35	-0.51	2.14
Compressor 4c	12.82	17.27	0.15	5.01
Compressor 5a	9.46	5.90	-0.05	0.56
Compressor 5b	9.07	6.35	-0.49	1.00
Compressor 5c	8.89	6.56	-1.38	-0.17
Compressor 6a	10.26	5.54	0.76	1.08
Compressor 6b	9.74	4.85	-0.31	-0.49
Compressor 6c	9.87	7.03	-0.63	0.64
Compressor 7	9.15	2.59	0.38	-1.35

From Table 5.3 it is clear that both total-to-total efficiency ($\eta_{TT,1-4}$) and total-to-total pressure ratio ($PR_{TT,1-4}$) predictions are significantly enhanced after implementation of the 1D code updates. For all the test compressors, total-to-total efficiency ($\eta_{TT,1-4}$) predictions are within 1.6% of the CFD values, with 13 of the 18 test compressors' results being within 1% of the CFD values. In the case of total-to-total pressure ratio ($PR_{TT,1-4}$) prediction, all 18 compressors show results that are within 5.5% of the CFD results, with 14 of the 18 test compressors exhibiting results that are within 2% of the CFD results. Across the 18 test compressors, the mean total-to-total efficiency ($\eta_{TT,1-4}$) prediction difference for the initial 1D code is 11.23%, while the mean difference for the updated 1D code is 0.74%. The mean total-to-total pressure ratio ($PR_{TT,1-4}$) prediction difference for the initial 1D code is 9.31%, while the mean difference for the updated 1D code is 1.24%. It is therefore clear that the updates incorporated in the 1D App code provides superior results compared to the original 1D code.

5.5   Velocity Triangle Comparison

The 1D App provides data regarding the predicted velocity components at the impeller and diffuser exit. These values were also compared to the CFD results. As an initial disclaimer, it is important to realise that the mean line theory inherently applies the notion of the flow through the compressor following a mean line or mean surface. In the mean line code, velocity components are therefore always determined to be in the plane of the mean line. At any point along the compressor, the mean line code is therefore not able to determine the true 3D velocity effects. To illustrate this, consider the flow exiting the compressor/diffuser at station 4 (see Figure 5.7). Due to the orientation of the mean flow line being purely horizontal at this point (Figure 5.7 left), the mean line code is unable to predict any vertical component of velocity. Realistically, of course, there will be a vertical component of velocity still present at this point (Figure 5.7 right). The presence of the vertical exit velocity component was correctly predicted by the CFD results for all the test compressors.
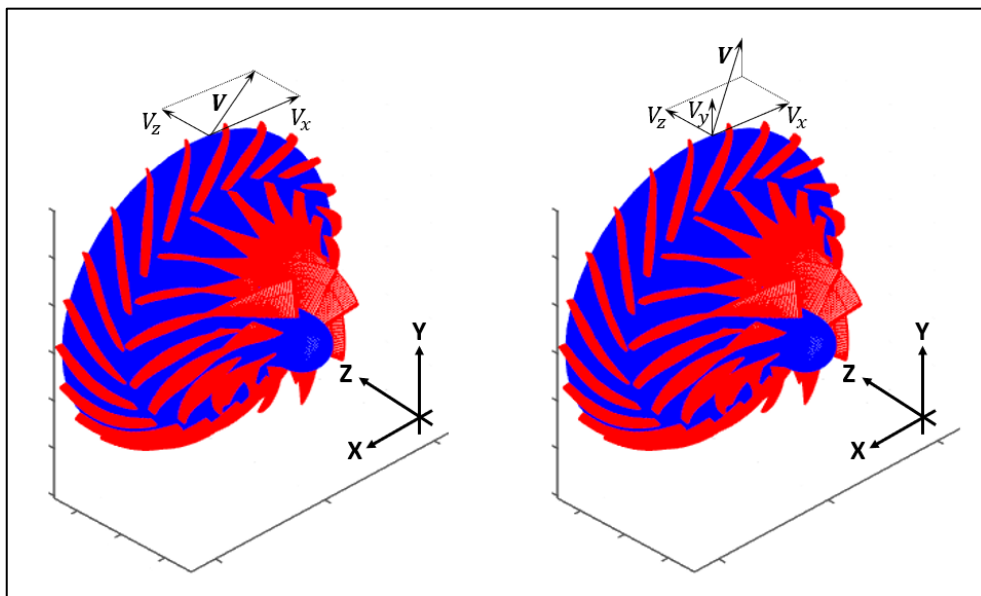

Figure 5.7: Velocity Prediction at Station 4 – 1D (left) and CFD (right)

Therefore, it is clear that the mean line theory may not provide accurate velocity results at the various compressor stations. The 1D App do however provide reasonable results. As an example, velocity triangle results for Compressor 1c are provided in Table 5.4:

Table 5.4: Velocity Triangle Comparison

Parameter	1D App Results	CFD Results
V_{x2} [m/s]	-275	-288
V_{y2} [m/s]	101	50
V_{z2} [m/s]	37	47
M_2	0.787	0.792
V_{x4} [m/s]	-59.8	-44
V_{y4} [m/s]	0	45
V_{z4} [m/s]	108.7	80
M_4	0.316	0.308

5.6   Final Test Compressor Results

As a final validation of the 1D App code, two more test compressors (Compressors 8 and 9 – see Appendix C) were designed using the 1D App and verified using Numeca/FINE™ Turbo. These two test compressors were designed subsequent to the various updates being incorporated in the 1D App code. Their performance results did therefore not influence the 1D App code updates. The purpose of designing and analysing these additional two compressors was to evaluate the maturity of the 1D App in terms of compressor design and CFD comparable performance prediction.
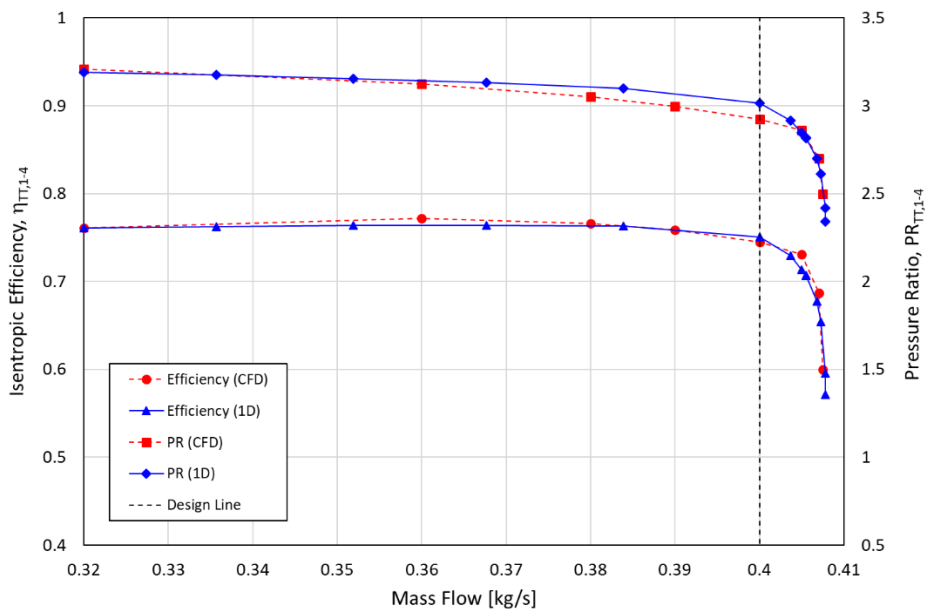

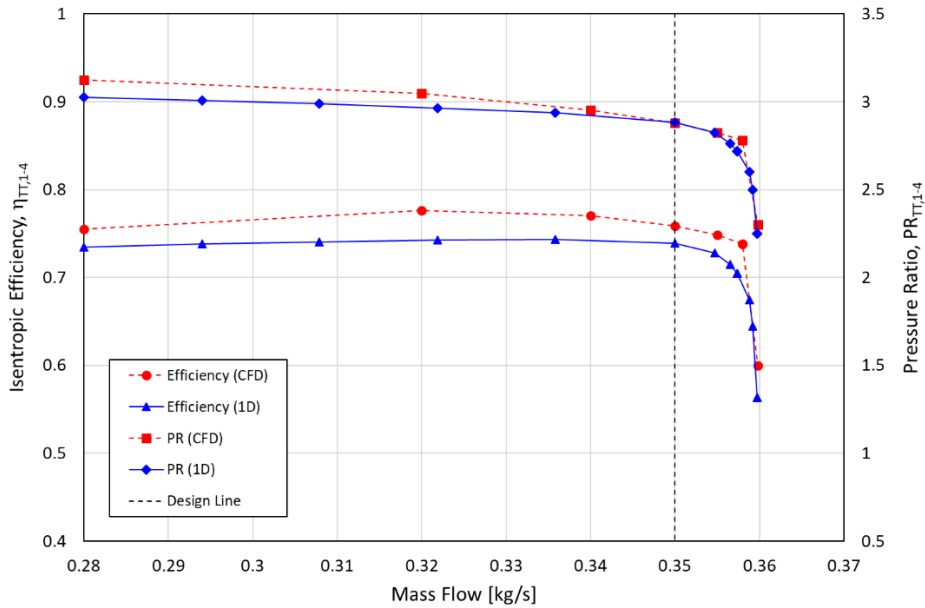Figure 5.8: Compressor 8 Performance Curves

Figure 5.9: Compressor 9 Performance Curves

Detailed performance curves for Compressors 8 and 9 are provided in Figure 5.8 and 5.9 respectively. (see also Appendix D). Performance prediction results are provided in Table 5.5.

Table 5.5: Performance Prediction Results for Final Two Test Compressors

Compressor Name	Updated 1D Code		
	Choke difference [%]	$\eta_{TT,1-4}$ difference [%]	$PR_{TT,1-4}$ difference [%]
Compressor 8	0.34	0.53	3.21
Compressor 9	-0.13	-2.00	0.18

From the performance graphs (Figure 5.8 and 5.9) and performance prediction results (Table 5.5), it was concluded that the updated 1D App provided good results for these two test compressors.

5.7   Summary

The developed 1D App aimed at providing a preliminary MGT engine compressor design tool. The performance prediction results achieved by the updated 1D App provide sufficient evidence that the developed 1D App achieved the primary objective.

Chapter 6:

Conclusions and Recommendations

A MATLAB® based application (1D App) is developed as a first-order, quick turn-around tool for the design and performance prediction of a MGT compressor stage. The 1D App caters for the design of pure radial, as well as mixed-flow compressor configurations in the subsonic flow regime. The 1D App further caters for the design of a crossover diffuser to be matched to the impeller. The 1D App design code is based on the mean line theory presented by Aungier (2000). The accuracy of the 1D App was evaluated by designing 18 test compressors and exporting the geometric data for 3D flow analysis and comparison using Numeca/FINE™ Turbo CFD software. Various performance prediction anomalies were identified in the original 1D mean line code. These anomalies were investigated, quantified, addressed and the subsequent improvements incorporated into the updated mean line code of the 1D App.

6.1   Project Summary

MATLAB® App Designer was used as the application development environment for the purpose of developing the front-end Graphical User Interface (GUI) of the 1D App. The App Designer environment provides the ability to call basic MATLAB® script files (.m files) as functions from the App Designer code. This allowed the in-house developed MATLAB® mean line code to be used as the basis for the 1D App. Specifically, the code used for the performance prediction of the impeller and crossover diffuser was primarily incorporated from the existing in-house code. New code was developed for the initial and detail design of the impeller and diffuser.

The 1D App provides the user with the ability to export the geometric parameters of a designed compressor in the form of a .geomTurbo file for specific use by Numeca/FINE™ Turbo. For the purpose of this project, 18 test compressors were designed by the 1D App. These test compressors covered a wide range of mass flows, rotational velocities and impeller meridional exit angles. The purpose of the 18 test compressors was to validate the accuracy of the compressor performance prediction of the 1D App mean line code.

Initial comparison of the 1D code and the CFD results indicated poor choke prediction across the test compressor range, as well as a general over-prediction in overall compressor performance. An initial investigation into the compressor performance over-prediction anomaly highlighted three main contributing factors:

i.   An over-prediction of impeller exit static pressure (p_2).

ii.   An under-prediction of diffuser skin friction losses ($\overline{\omega}_{SF}$).

iii.   An under-prediction of diffuser exit total temperature (T_{04}).

A further investigation into the choke anomaly revealed an over-prediction in the choke mass flow rate for compressors with a tip flow coefficient below 0.34. In contrast, an under-prediction in choke mass flow rate was observed for compressors with a design tip flow coefficient above 0.34. In the mean line code, choke is predicted by the choke loss model. For a specific compressor, the choke mass flow rate could be varied by varying the numerical value of the first term of Equation 5.3. It was observed that there was a relationship between the corrected term and the impeller exit slip factor for compressors with a design tip flow coefficient above 0.34. For compressors with a design tip flow coefficient below 0.34, it was found that the required term varied as a function of not just the impeller exit slip factor, but also as a function of mass flow rate, rotational velocity and impeller meridional exit angle. An alternative flow parameter (ψ) was developed that incorporated these parameters. The required choke equation term was compared to this alternative flow parameter for compressors with a design tip flow coefficient below 0.34. It was found that there was a linear relationship between these parameters. These choke relationships were consequently quantified and incorporated into the mean line code of the 1D App. Much better choke prediction results were achieved. Initial 1D mean line results presented a mean choke prediction difference of 14.98% for the 18 test compressors, with a maximum difference of 39.88%. In the updated 1D App code the mean difference was reduced to 1.59% with a maximum difference of 4.97%.

The initial 1D code over-prediction of the impeller exit static pressure was also investigated in relation to the impeller exit slip factor and the alternative flow parameter (ψ). It was found that there was a relationship between the static pressure over-prediction and impeller exit slip factor for compressors with a tip flow coefficient above 0.34, while a relationship existed between the static pressure over-prediction and the alternative flow parameter for compressors with a design tip flow coefficient below 0.34.

The compressor performance over-prediction initially produced by the 1D code was primarily attributed to the under-prediction in diffuser skin friction losses ($\overline{\omega}_{SF}$). It was found that the inherited crossover diffuser 1D code only calculated diffuser skin friction losses in one channel in the diffuser vaned section. The 1D App code was updated to ensure skin friction losses were calculated for all the flow channels inside the diffuser vaned section.

The under-prediction in diffuser exit total temperature (T_{04}) had a marked influence on the overall compressor isentropic efficiency prediction. Deeper investigation revealed that the exit total temperature under-prediction values changed in relation to the impeller exit slip factor.

All three contributing performance prediction anomalies were quantified and incorporated in the updated 1D App code. Considerably better performance prediction results were achieved after these code modifications. Initial 1D mean line results presented a mean $PR_{TT,1-4}$ prediction difference of 9.31% for the 18 test compressors, with a maximum difference of 17.27%. In the updated 1D App code the mean difference was reduced to 1.24% with a maximum difference of 5.01%. In the case of total-to-total efficiency, the initial 1D mean line results presented a mean $\eta_{TT,1-4}$ prediction difference of 11.23% for the 18 test compressors, with a maximum difference of 15.09%. In the updated 1D App code the mean difference was reduced to 0.74% with a maximum difference of 1.57%.

6.2 Conclusion

The primary intention of this study is to develop a preliminary design tool for the purpose of designing a compressor for a MGT engine. The 1D App developed during this study provides a user-friendly, intuitive platform for this purpose. The performance analysis of 20 test compressors (18 initial and 2 final validation test compressors – see Appendix C) demonstrates the capability of the 1D App in providing good performance prediction results across a wide range of compressor designs. 1D App code modifications include better choke prediction, as well as improved overall performance prediction results. Following these code modifications, performance results are comparable to CFD results.

The 1D App allows the designer an early verdict on the feasibility of a compressor design. Once a design is selected, further design optimisation and accurate performance prediction results can be conducted by further CFD analysis and the use of optimisation techniques.

6.3 Recommendations

The compressor stall prediction models incorporated in the 1D App code is unmodified from the in-house developed 1D code. Compared to the observed CFD results, the 1D App stall prediction seems adequate, although comprehensive stall investigation was not conducted to the level that choke prediction was done. Future studies could focus in more detail on accurate stall prediction characteristics of the 1D App.

Kim *et al.* (2001) highlighted the importance of a proper compressor inlet design, which could seriously reduce the performance of a compressor due to inlet flow distortions. A future upgrade to the 1D App should investigate an inlet design code, including the option of inlet guide vanes.

The 1D App developed in this study only catered for the design of a vaned crossover diffuser. A future upgrade to the 1D App could be to include other

diffuser types, e.g. vaneless diffuser and conventional vaned diffuser with or without de-swirler vanes. Future studies could also investigate the inclusion of tandem diffuser vane arrangements in lieu of a continuous vane (crossover) arrangement. This should alleviate the typical larger boundary layers associated with longer passages.

The 1D App in its current form does not cater for any lean/rake angle distribution of the crossover diffuser blades. Previous studies have shown that slight lean in the direction of rotation, especially at the leading edge of the diffuser blade, could provide much better flow alignment with the flow pattern emerging from the impeller (Krige, 2013). A future upgrade to the 1D App could incorporate this feature.

The updates to the 1D App proposed in this study are primarily semi-empirical methods incorporated to correct for the anomalies observed. A future study could explore a physical and theoretical approach to verify the empirical methods developed in this study.

References

Aungier, R. H. (1995). Mean Streamline Aerodynamic Performance Analysis of Centrifugal Compressors. *Journal of Turbomachinery*.

Aungier, R. H. (2000). *Centrifugal Compressors A Strategy for Aerodynamic Design and Analysis* (First). New York: Asme Press.

Beér, J.,and Chigier, N. (1972). *Combustion Aerodynamics*. New York.

Bindeman, M. (2019). *Analysing the Performance of a Compressor Impeller for a Micro Gas Turbine*. University of Stellenbosch.

Boyce, M. P. (1993). Principles Of Operation And Performance Estimation Of Centrifugal Compressors. *Xxii Turbo Machinery Symposium*, vol. 22, no. 2, pp. 161–178.

Boyce, M. P. (2012). Compressor and Turbine Performance Characteristics. In *Gas Turbine Engineering Handbook* (Fourth). Oxford: Elsevier Inc.

Burger, C. (2016). *Design Procedure of a Compact Aerodynamic Crossover Diffuser for Micro Gas Turbine Application*. University of Stellenbosch.

Çevik, M. (2009). *Design and Optimization of a Mixed Flow Compressor Impeller using Robust Design Methods*. Citeseer.

Çevik, M.,and Uzol, O. (2011). Design optimization of a mixed-flow compressor impeller for a small turbojet engine. *Aircraft Engineering and Aerospace Technology*, vol. 83, no. 3, pp. 127–137.

Cumpsty, N. A. (2004). *Compressor Aerodynamics*. Krieger Publishing Company.

De Villiers, L. C. B. (2013). *Numeca Manual for the Design of a Centrifugal Compressor*.

De Villiers, L. C. B. (2014). *Design of a Centrifugal Compressor for Application in Micro Gas Turbines*. University of Stellenbosch.

De Wet, A. L. (2012). *Performance Investigation of a Turbocharger Compressor*. University of Stellenbosch.

Diener, O. H. F. (2016). *Development of a Mixed-Flow Compressor Impeller for Micro Gas Turbine Application*. University of Stellenbosch.

Dixon, S. L. (1998). *Fluid Mechanics, Thermodynamics of Turbomachinery* (Fourth). Oxford: Butterworth-Heinemann.

Dixon, S. L.,and Hall, C. A. (2014). *Fluid Mechanics and Thermodynamics of Turbomachinery* (Seventh). Oxford: Butterworth-Heinemann.

Dossena, V.,Gaetani, P.,Mora, A.,Osnaghi, C.,and Persico, G. (2012). Impeller-Vaned Diffuser Interaction in a Centrifugal Compressor at Off Design

Conditions. *Journal of Turbomachinery*, vol. 134, no. 6, pp. 061034.

Eck, B. F. (1973). *Fans: design and operation of centrifugal, axial-flow and cross-flow fans*. New York: Oxford University Press.

Giri, G.,Klimov, I. V.,Moroz, L.,Nassar, A.,and Sherbina, A. (2016). Design and analysis of a high pressure ratio mixed flow compressor stage. In *52nd AIAA/SAE/ASEE Joint Propulsion Conference, 2016*.

Giri, G.,Nassar, A.,Moroz, L.,Klimov, I. V.,and Sherbina, A. (2016). Design and analysis of a high pressure ratio mixed flow compressor stage. In *52nd AIAA/SAE/ASEE Joint Propulsion Conference, 2016*.

Goldstein, A. W. (1948). *Design and performance of experimental axial-discharge mixed-flow compressor impeller design theory*. *NACA RM E8F04*.

Halawa, T.,Gadala, M. S.,Alqaradawi, M.,and Badr, O. (2015). Optimization of the Efficiency of Stall Control Using Air Injection for Centrifugal Compressors. *Journal of Engineering for Gas Turbines and Power*, vol. 137, no. 7,.

Harris, M.,Jones, A.,and Alexander, E. (2003). Miniature Turbojet Development at Hamilton Sundstrand: The TJ-50, TJ-120 and TJ-30 Turbojets.

Herbert, M. V. (1980). *A method of performance prediction for centrifugal compressors. London, U.K., Hmso, Feb. 1980*. National Gas Turbine Establishment.

Japikse, D. (1996). *Centrifugal compressor design and performance*. Concepts ETI, Inc.

Japikse, D.,and Baines, N. C. (1997). *Introduction to turbomachinery*. Concepts ETI, Inc.

Ji, C.,Zou, J.,Ruan, X. D.,Dario, P.,and Fu, X. (2011). A new correlation for slip factor in radial and mixed-flow impellers. *Proceedings of the Institution of Mechanical Engineers, Part A: Journal of Power and Energy*.

Jie, C.,and Guoping, H. (2010). Redesign of an 11 cm-diameter Micro Diffuser. *Chinese Journal of Aeronautics*, vol. 23, no. 3, pp. 298–305. https://doi.org/10.1016/S1000-9361(09)60219-3

Kano, F.,Fukao, Y.,and Shirakami, T. (1984). Development of High Specific Speed Mixed Flow Compressors. *Turbomachinery and Pump Symposia*, pp. 139–148.

Kim, Y.,Engeda, A.,Aungier, R.,and Direnzi, G. (2001). The influence of inlet flow distortion on the performance of a centrifugal compressor and the development of an improved inlet using numerical simulations. *Proceedings of the Institution of Mechanical Engineers, Part A: Journal of Power and Energy*, vol. 215, , pp. 323–338.

Klausner, E.,and Gampe, U. (2014). Evaluation and Enhancement of a One-Dimensional Performance Analysis Method for Centrifugal Compressors. *Proceedings of ASME Turbo Expo 2014: Turbine Technical Conference and*

Exposition.

Kock, M. P. (2017). *Design of a Cross-over Diffuser for a Mixed Flow Compressor Impeller*. University of Stellenbosch.

Krain, H. (1981). A study on centrifugal impeller and diffuser flow. *Journal of Engineering for Gas Turbines and Power*, vol. 103, no. 4, pp. 688–697.

Krige, D. S. (2013). *Performance Evaluation of a Micro Gas Turbine Centrifugal Compressor Diffuser*. University of Stellenbosch.

Kröger, D. G. (2004). *Air-cooled Heat Exchanger and Cooling Towers. Thermal-flow Performance Evaluation and Design.* University of Stellenbosch.

Ling, J.,Wong, K. C.,and Armfield, S. (2007). Numerical investigation of a small gas turbine compressor. *Proceedings of the 16th Australasian Fluid Mechanics Conference (AFMC)*, pp. 961–966.

Marcellan, A.,Visser, W. P. J.,and Colonna, P. (2016). Potential of micro turbine based propulsion systems for civil UAVS: A case study. In *Proceedings of the ASME Turbo Expo.*

Musgrave, D. S.,and Plehn, N. J. (1987). Mixed-flow compressor stage design and test results with a pressure ratio of 3:1. *Journal of Turbomachinery*, vol. 109, no. October, pp. 513–519.

Numeca International. (2018a). *FINE^{TM}/Turbo 13.1 User Guide*.

Numeca International. (2018b). *IGG^{TM}/AutoGrid5^{TM} 13.1 User Guide*.

Orth, U.,Ebbing, H.,Krain, H.,Weber, A.,and Hoffmann, B. (2001). Improved compressor exit diffuser for an industrial gas turbine. In *Proceedings of the ASME Turbo Expo.*

Phillips, W. F. (2004). *Mechanics of Flight*. Wiley.

Qiu, X.,Japikse, D.,Zhao, J.,and Anderson, M. R. (2011). Analysis and validation of a unified slip factor model for impellers at design and off-design conditions. *Journal of Turbomachinery*, vol. 133, no. October, pp. 1–9.

Rajakumar, D. R.,Ramamurthy, S.,and Govardhan, M. (2015). Experimental investigations on effects of tip clearance in mixed-flow compressor performance. *Proceedings of the Institution of Mechanical Engineers, Part G: Journal of Aerospace Engineering*, vol. 229, no. 5, pp. 933–946.

Sandberg, M. R. (2016). Centrifugal Compressor Configuration, Selection and Arrangement: A User's Perspective. In *Proceedings of the Forty-Fifth Turbomachinery Symposium*.

Saravanamuttoo, H. I. H.,Rogers, G. F. C.,and Cohen, H. (2001). *Gas Turbine Theory (5th Ed.). Gas Turbine Theory (5th Ed.).* Prentice-Hall.

Schiff, J. (2013). *A preliminary design tool for radial compressors*. Lund University.

Spalart, P. R.,and Allmaras, S. R. (1992). A one-equation turbulent model for aerodynamics flows. *AIAA Paper 92 - 0439*.

Stodola, A. (1945). *Steam and gas turbines : with a supplement on the prospects of the thermal prime mover*. New York: Smith, New York.

Sundström, E.,Kerres, B.,Sanz, S.,and Mihǎescu, M. (2017). On the Assessment of Centrifugal Compressor Performance Parameters by Theoretical and Computational Models. In *Turbo Expo: Power for Land, Sea and Air*.

Trebunskikh, T.,Ivanov, A.,and Dumnov, G. (2012). Small But Mighty Powerful - Micro-turbine Jet Engine Simulation and Structural Analysis Using FloEFD^{TM} and Creo® Simulate. *Engineering Edge Volume 1 Issue 1*, pp. 28–31.

van der Merwe, B. B. (2012). *Design of a Centrifugal Compressor Impeller for Micro Gas Turbine Application*. University of Stellenbosch.

Versteeg, H. K.,and Malalasekera, W. (2007). *An Introduction to Computational Fluid Dynamics The Finite Volume Method* (Second). Harow: Pearson Education.

Verstraete, T.,Alsalihi, Z.,and Van den, R. A. (2010). Multidisciplinary optimization of a radial compressor for microgas turbine applications. *Journal of Turbomachinery*.

Von Backström, T. W. (2006). A unified correlation for slip factor in centrifugal impellers. *Journal of Turbomachinery*, vol. 128, no. January 2006,.

Wiesner, F. J. (1967). A review of slip factors for centrifugal impellers. *Journal of Engineering for Gas Turbines and Power*, vol. 89, no. 4, pp. 558–566.

Ziegler, K. U.,Gallus, H. E.,and Niehuis, R. (2003). A study on impeller-diffuser interaction - Part I: Influence on the performance. *Journal of Turbomachinery*.

APPENDIX A:
Impeller Design Calculations

A.1   Derivation of Impeller Relative Exit Blade Angle Formula

From the impeller velocity exit triangle (Figure 2.6) it follows that:

$$\frac{\Delta C_{U2}}{sin(\beta_2' - \beta_2)} = \frac{W_2}{sin(\pi + \beta_2)} \tag{A1.1}$$

Also:

$$C_{U2} = U_2 - W_2 sin\beta_2' \tag{A1.2}$$

Now substituting Equation A1.2 into Equation 2.3:

$$\sigma_s = \frac{U_2 - W_2 sin\beta_2'}{U_2 - W_2 sin\beta_2' + \Delta C_{U2}} \tag{A1.3}$$

Rewriting Equation A1.3:

$$\Delta C_{U2} = \frac{U_2 - W_2 sin\beta_2'}{\sigma_s} - U_2 + W_2 sin\beta_2' \tag{A1.4}$$

Now substituting Equation A1.4 into Equation A1.1:

$$\frac{W_2}{sin(\pi + \beta_2)} = \frac{\frac{U_2}{\sigma_s} - \frac{W_2 sin\beta_2'}{\sigma_s} - U_2 + W_2 sin\beta_2'}{sin(\beta_2' - \beta_2)} \tag{3.11}$$

A.2   Impeller Hub and Shroud Blade Angle Distribution

Aungier (1995) proposed generalised hub and shroud blade distribution equations. These are expressed as a function of the normalised meridional length (ζ) of the hub and shroud curves. The shape of the hub blade angle distribution is also heavily dependent on the rake angle parameter (K) as well as the inlet rake angle. Both these values are user defined in the 1D App under the Impeller Detail Design section.

For the hub blade angle distribution, the following set of equations are applicable:

$$\beta_h(\zeta) = \beta_{1h} + A\zeta + B\zeta^2 + C\zeta^3$$

where:

$$
\begin{aligned}
A &= -4\left(\beta_2 - 2\bar{\beta}_h + \beta_{1h}\right) \\
B &= 11\beta_2 - 16\bar{\beta}_h + 5\beta_{1h} \\
C &= -6\beta_2 + 8\bar{\beta}_h - 2\beta_{1h}
\end{aligned}
\qquad \text{(A1.5)}
$$

and:

$$\bar{\beta}_h = 90K - (1 - K)\frac{1}{2}(\beta_2 + \beta_{1h})$$

In the case of the blade angle distribution along the shroud curve:

$$\beta_s(\zeta) = \beta_{1s} + (\beta_2 - \beta_{1s})(3\zeta^2 - 2\zeta^3) \qquad \text{(A1.6)}$$

A.3 Blade Thickness Distribution

The blade thickness distribution procedure employed in the 1D App is based on the proposal by Verstraete *et al.* (2010). The distribution follows an elliptical distribution along the first section of the blade and a parabolic distribution towards the trailing edge (refer Figure 3.4). The calculations for the thickness distributions along the hub are provided below. These are used for the distributions along the shroud as well.

With $0 \leq \zeta < u_1$ (elliptical section):

$$t_{Bh}(\zeta) = 2\sqrt{\left(\frac{1}{2}t_{Bh1}\right)^2 \left(1 - \left(\frac{\zeta - u_1}{u_1}\right)^2\right)} \qquad \text{(A1.7)}$$

With $u_1 \leq \zeta \leq u_2$ (straight section):

$$t_{Bh}(\zeta) = t_{Bh1} \qquad \text{(A1.8)}$$

With $u_2 < \zeta \leq 1$ (parabolic section):

$$t_{Bh}(\zeta) = 2[a\zeta^2 + b\zeta + c]$$

where:

$$
\begin{aligned}
a &= \frac{(t_{Bh1} - t_{Bh2})}{2(-u_2^2 + 2u_2 - 1)} \\
b &= -2au_2 \\
c &= \frac{1}{2}t_{Bh1} + 2au_2 - a
\end{aligned}
\qquad \text{(A1.9)}
$$

A.4   Throat Geometry Calculations

The throat width along any blade-to-blade surface (i.e. hub) describes a 3D locus, as the line describing the width, varied in the θ, r and z directions. Aungier (2000) suggested a conformal transformation of the blade coordinates. Firstly, the r and z coordinates are transformed into a meridional coordinate (m). The (m, θ) plane are then transformed into a 2D (X, Y) plane.

$$X = \int_{m_1}^{m_i} \frac{dm}{r}$$

$$Y = \theta$$

(A1.10)

In the transformed (X, Y) plane, the throat width has a constant angle (refer Figure A.1). This angle is expressed as:

$$\frac{\partial Y}{\partial X} = \frac{r \partial \theta}{\partial m} = constant$$

(A1.11)
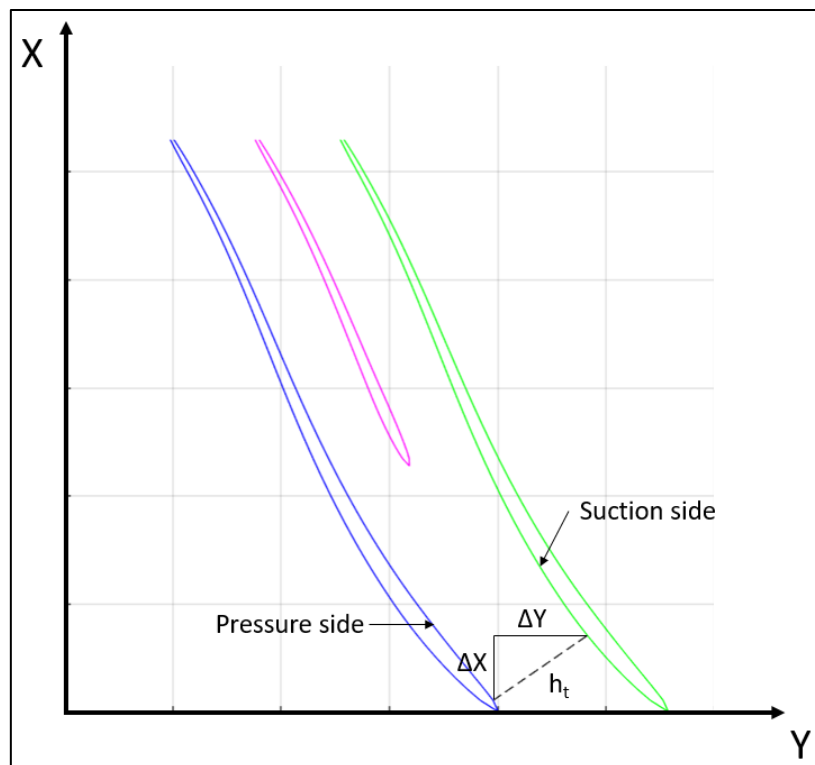
Figure A.1: Throat Width in (X, Y) Plane

The throat width is then calculated as:

$$h_{th} = \int_{m_1}^{m_i} \sqrt{1 + \left(\frac{r\partial\theta}{\partial m}\right)^2}\, dm = \sqrt{1 + \left(\frac{\Delta\theta}{X}\right)^2}\, \Delta m \qquad \text{(A1.12)}$$

where $\Delta\theta$ and Δm are determined between points on the opposing blades and X are evaluated only on the suction blade surface. Since h_{th} can theoretically be calculated between any two points on opposing blades, the 1D App calculates h_{th} for all the points on the suction side of the passage from a number of points around the initially determined (see section 3.4.3) throat position on the pressure side. This is done in an attempt to refine the throat position by searching for a minimum h_{th} value. The same procedure is repeated for a pre-defined number of stream surfaces from hub to shroud, each time calculating the minimum h_{th} for the consecutive stream surfaces. This creates a 3D throat area inside the blade-to-blade passage area. With h_{th} available for each stream surface from hub to shroud and with the gap between stream surfaces known, the throat area is determined in an incremental fashion.

APPENDIX B:
1D App Design Process Flowcharts

The flowcharts for the four primary iterative design processes used in the 1D App code are provided here. These include:

    i.   Initial impeller design process.

    ii.   Detail impeller design process.

    iii.   Diffuser curve design process.

    iv.   Diffuser detail design.

B.1 Initial Impeller Design

The routine to determine the initial impeller inlet and outlet geometry and flow conditions is executed once the Impeller 'Basic Design Parameters' tab is completed and accepted.
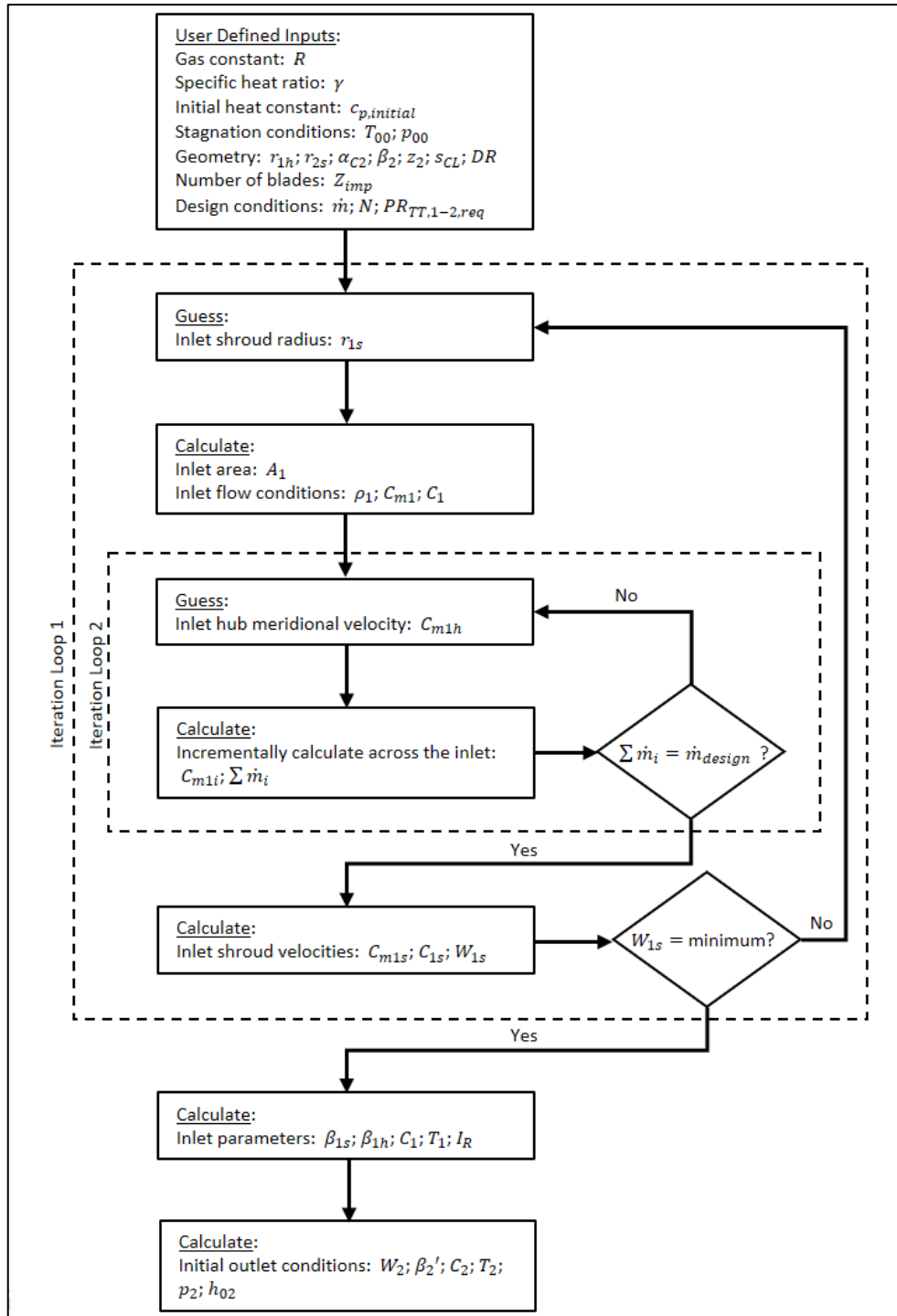
Figure B.1: Initial Impeller Design Flowchart

B.2   Detail Impeller Design

The routine to complete the detail design of the impeller is executed once the impeller 'Detail Design' tab is completed.
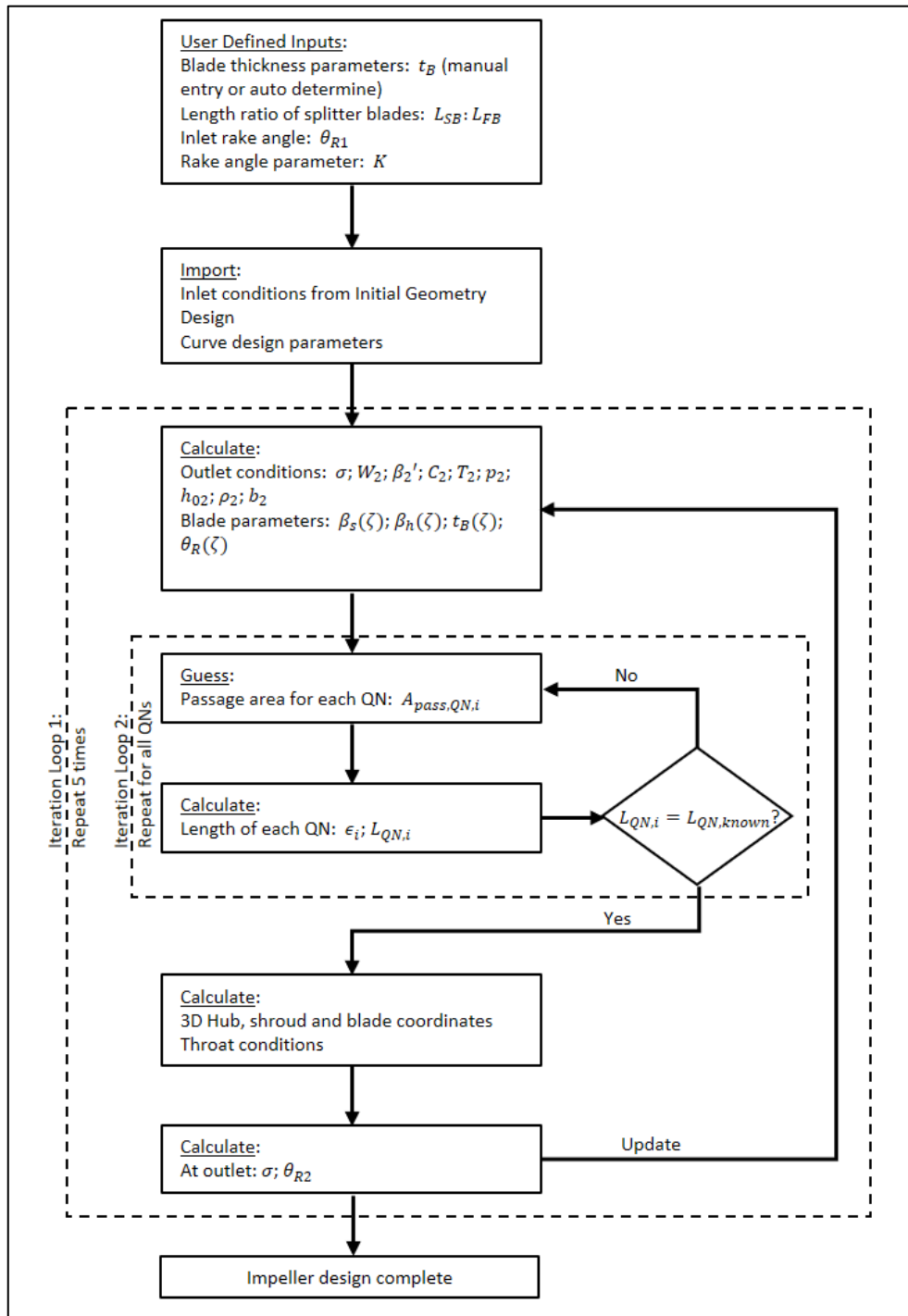
Figure B.2: Detail Impeller Design Flowchart

B.3   Diffuser Curve Design

The diffuser curve design routine, as well as the initial performance evaluation of the vaneless gap is performed on completion and acceptance of the diffuser 'Basic Design Parameters & Curve Design' tab in the 1D App.

User Defined Inputs:
Geometry: r_{4h}; r_{4s}; z_4; i_3; r_3/r_2
Bezier curve constant: BC_{CC}
Blade parameters: K_3; K_4; β_4 (manual entry or auto determine)

Import:
Impeller exit conditions from impeller design

Calculate:
Hub and shroud meridional curves

Calculate:
Vaneless gap performance and diffuser blade inlet conditions at station 3: β_3; C_3; T_3; T_{03}; p_3; p_{03}; ρ_3; h_{03}
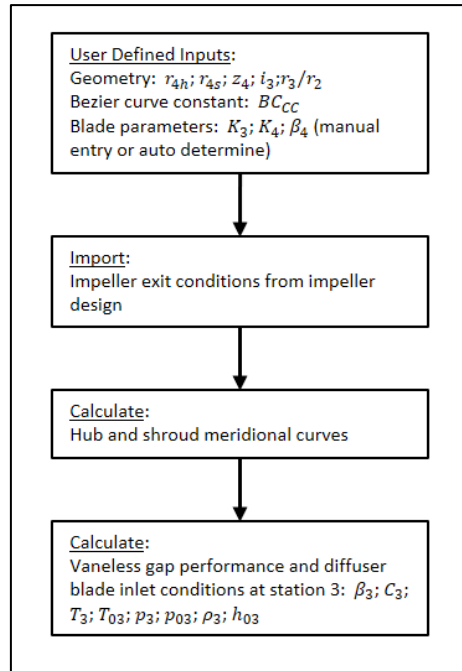
Figure B.3: Diffuser Curve Design Flowchart

B.4   Diffuser Detail Design

The routine to complete the detail design of the impeller is executed once the user completes and initiates the design process under the diffuser 'Detail Design' tab in the 1D App. The user can specify values for K_3, K_4 and/or β_4, or these values can be optimised by the routine.
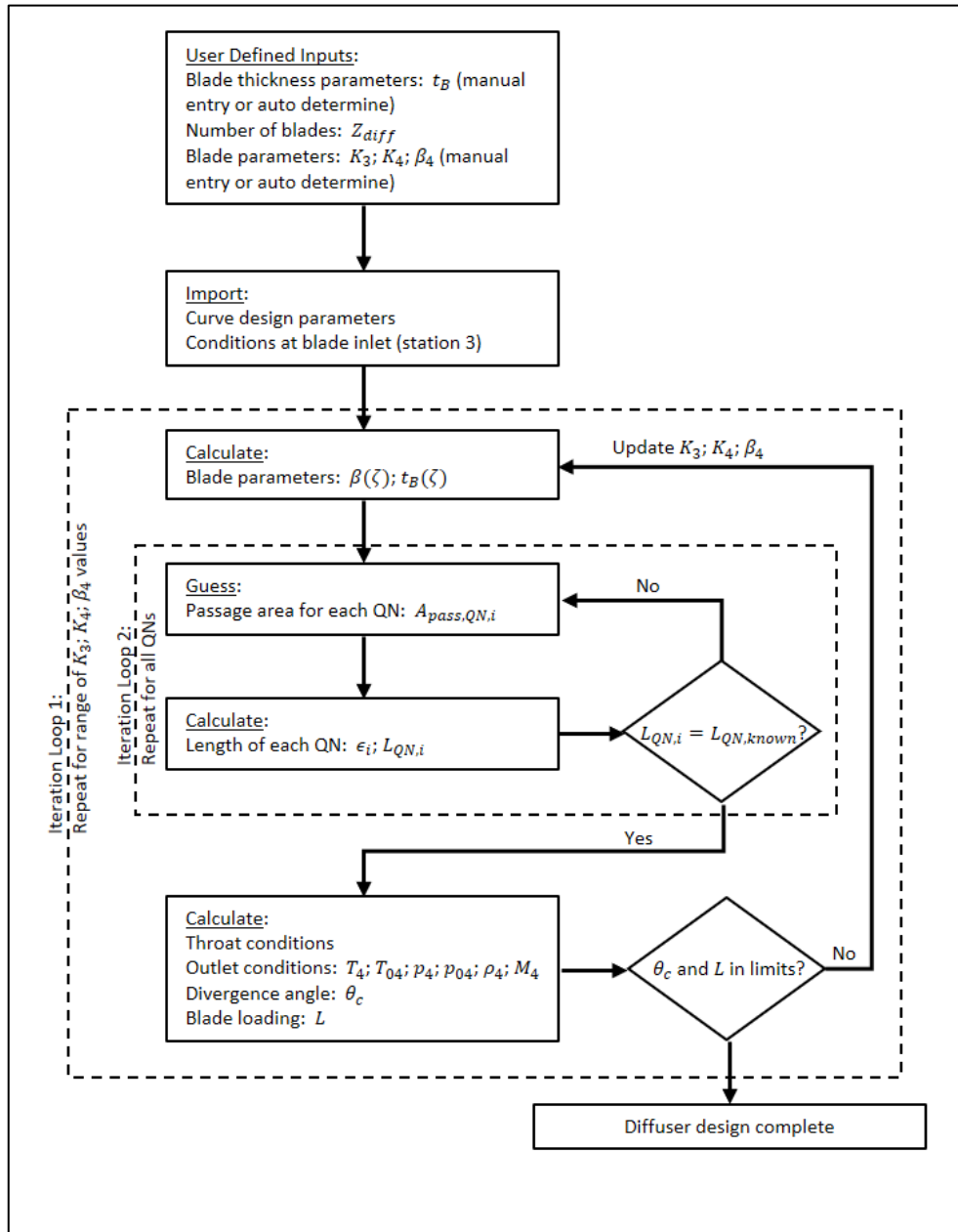
Figure B.4: Diffuser Detail Design Flowchart

APPENDIX C:
Test Compressor Details

The basic design parameters of the 18 test compressors were chosen to cover a wide range of rotational velocities, mass flows and impeller meridional exit angles (for the purpose of mixed flow configurations). Details of the 18 test compressors are provided below.

Table C.1: Test Compressor Details

#	Name	Design N [RPM]	Design $\dot{m}$ [kg/s]	ϕ_2	σ_s	Impeller Meridional Exit Angle [°]	Schematic
1	Comp1a	30000	0.8	0.2615	0.8737	90	
2	Comp1b	30000	0.8	0.2658	0.8754	80	
3	Comp1c	30000	0.8	0.2706	0.8807	70	
4	Comp2a	45000	0.5	0.2903	0.8714	90	

#	Name	Design N [RPM]	Design $\dot{m}$ [kg/s]	ϕ_2	σ_s	Impeller Meridional Exit Angle [°]	Schematic
5	Comp2b	45000	0.5	0.2984	0.8754	75	
6	Comp2c	45000	0.5	0.3014	0.8785	70	
7	Comp3a	50000	0.5	0.2675	0.8717	90	
8	Comp3b	50000	0.5	0.2772	0.874	78	
9	Comp4a	75000	0.4	0.3728	0.8572	90	
10	Comp4b	75000	0.4	0.3845	0.8598	78	
11	Comp4c	75000	0.4	0.3978	0.8691	65	

APPENDIX C. TEST COMPRESSOR DETAILS   98

#	Name	Design N [RPM]	Design $\dot{m}$ [kg/s]	ϕ_2	σ_s	Impeller Meridional Exit Angle [°]	Schematic
12	Comp5a	100000	0.3	0.3454	0.8212	90	
13	Comp5b	100000	0.3	0.3553	0.8238	80	
14	Comp5c	100000	0.3	0.3649	0.8309	70	
15	Comp6a	115000	0.25	0.3409	0.7967	90	
16	Comp6b	115000	0.25	0.3537	0.8001	78	
17	Comp6c	115000	0.25	0.361	0.807	70	
18	Comp7	121000	0.325	0.3586	0.7993	90	

#	Name	Design N [RPM]	Design $\dot{m}$ [kg/s]	ϕ_2	σ_s	Impeller Meridional Exit Angle [°]	Schematic
FT1	Comp8	60000	0.4	0.295	0.8599	80	
FT2	Comp9	90000	0.35	0.3449	0.8425	90	

APPENDIX D:
Test Compressor Performance Results

The performance prediction accuracy of the 1D App was evaluated by designing 18 test compressors using the 1D App. These test compressors covered a wide range of design velocities, mass flow rates, and meridional exit angles (mixed flow compressors). The geometry files (.geomTurbo) of these 18 test compressors were imported into Numeca/FINE™ Turbo CFD software. These results were compared to the performance prediction results obtained by the 1D App.

Initial 1D App results were unsatisfactory. After quantifying the various performance prediction anomalies, the 1D App code was updated accordingly. The overall compressor performance prediction plots (total-to-total isentropic efficiency ($\eta_{TT,1-4}$) and total-to-total pressure ratio ($PR_{TT,1-4}$)) of the initial 1D code, the CFD results and the updated 1D App code are provided here for the 18 test compressors.

After the 1D App code was updated, 2 more compressors were designed and validated using Numeca/FINE™ Turbo CFD software. The comparative performance results for these two additional compressors are also provided.
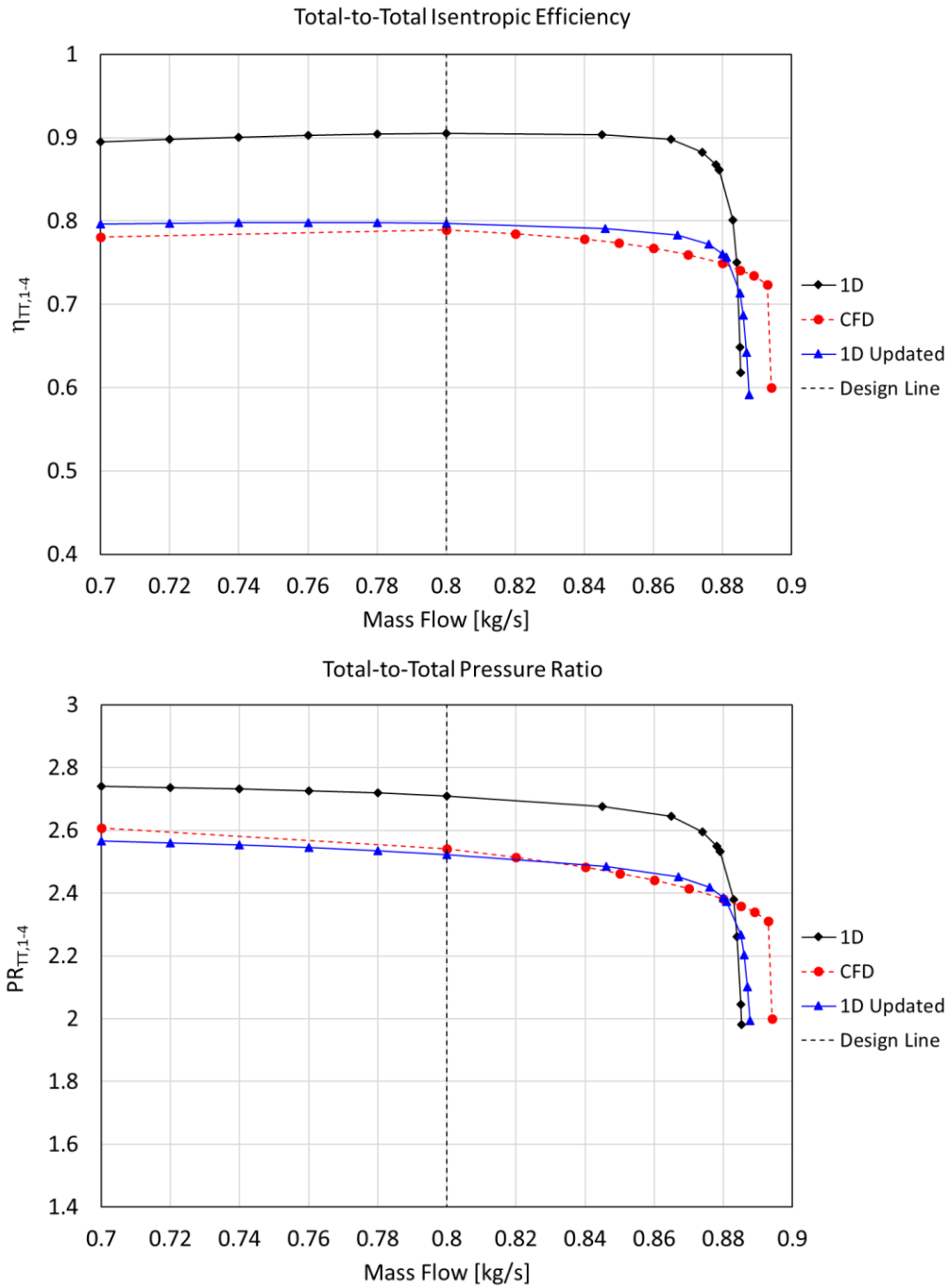
Figure D.1: Compressor 1a Performance Comparison
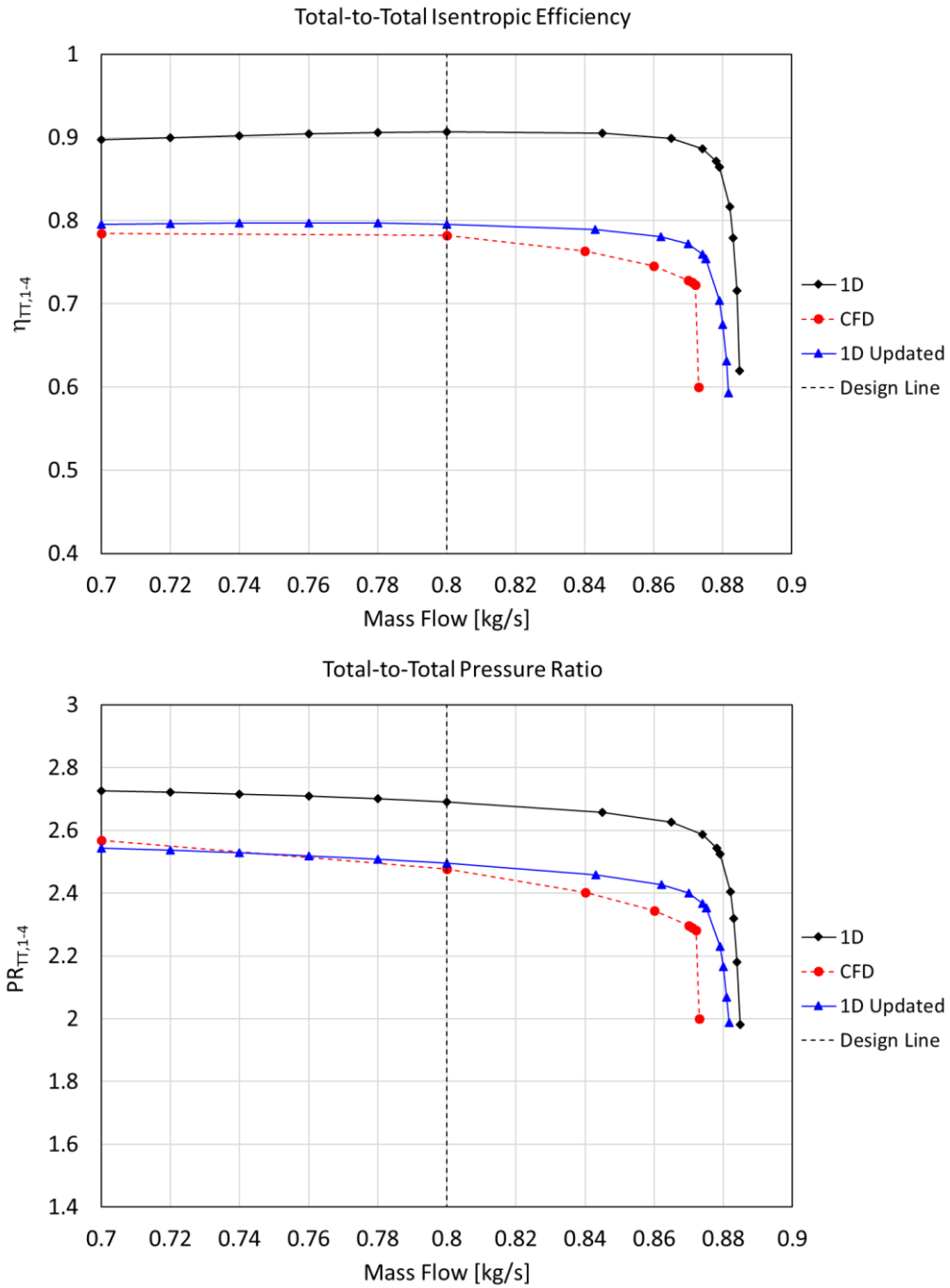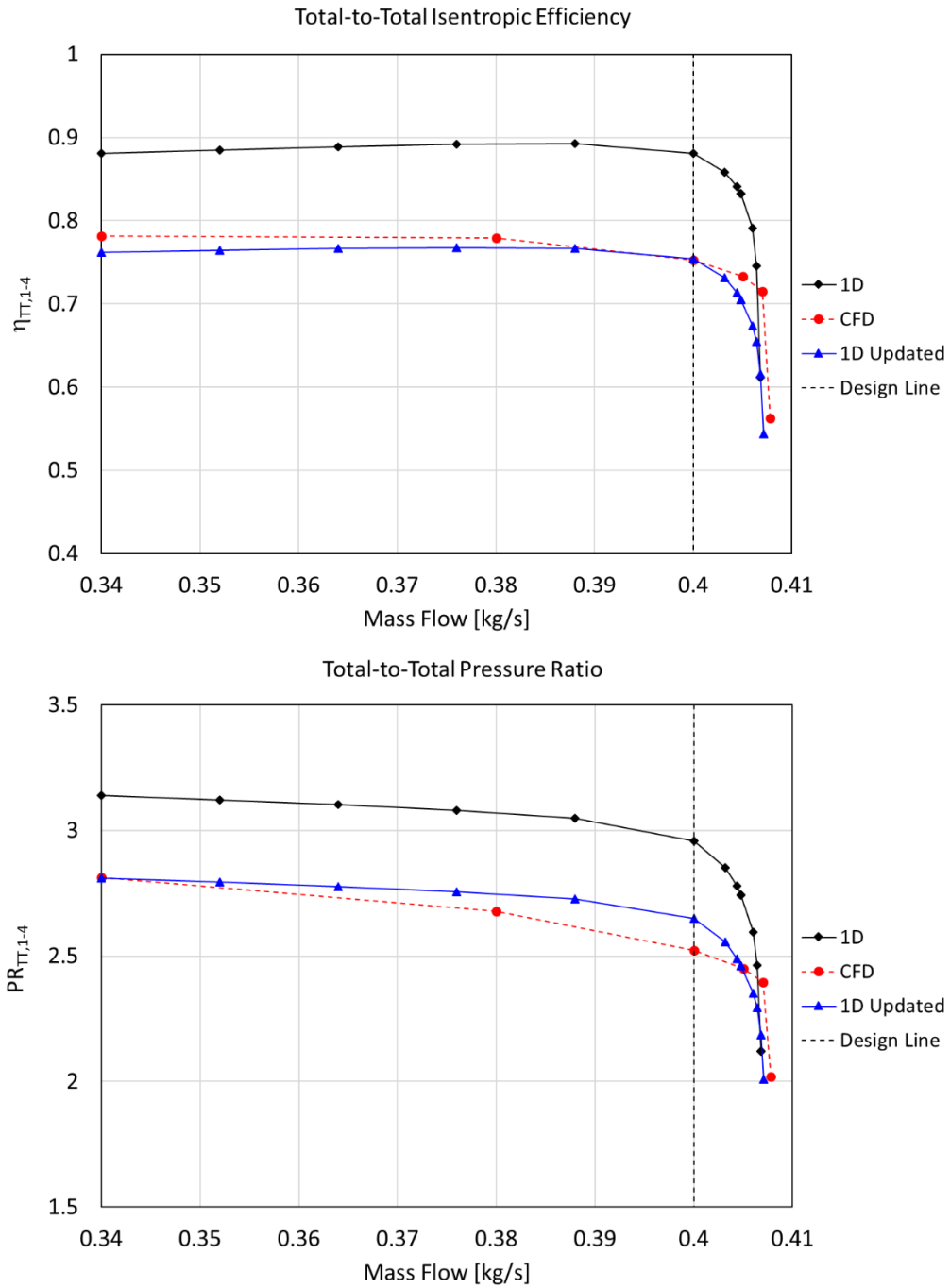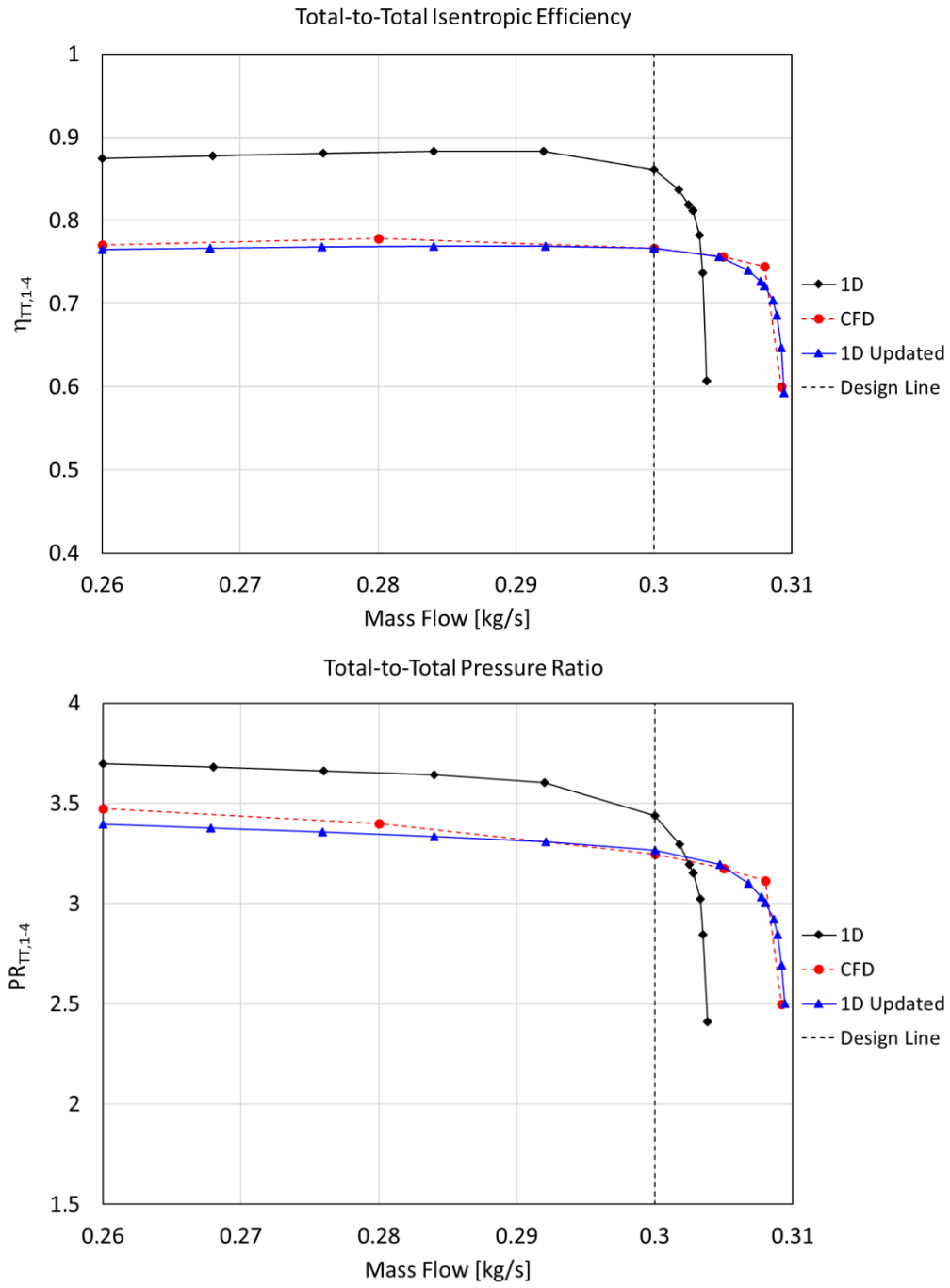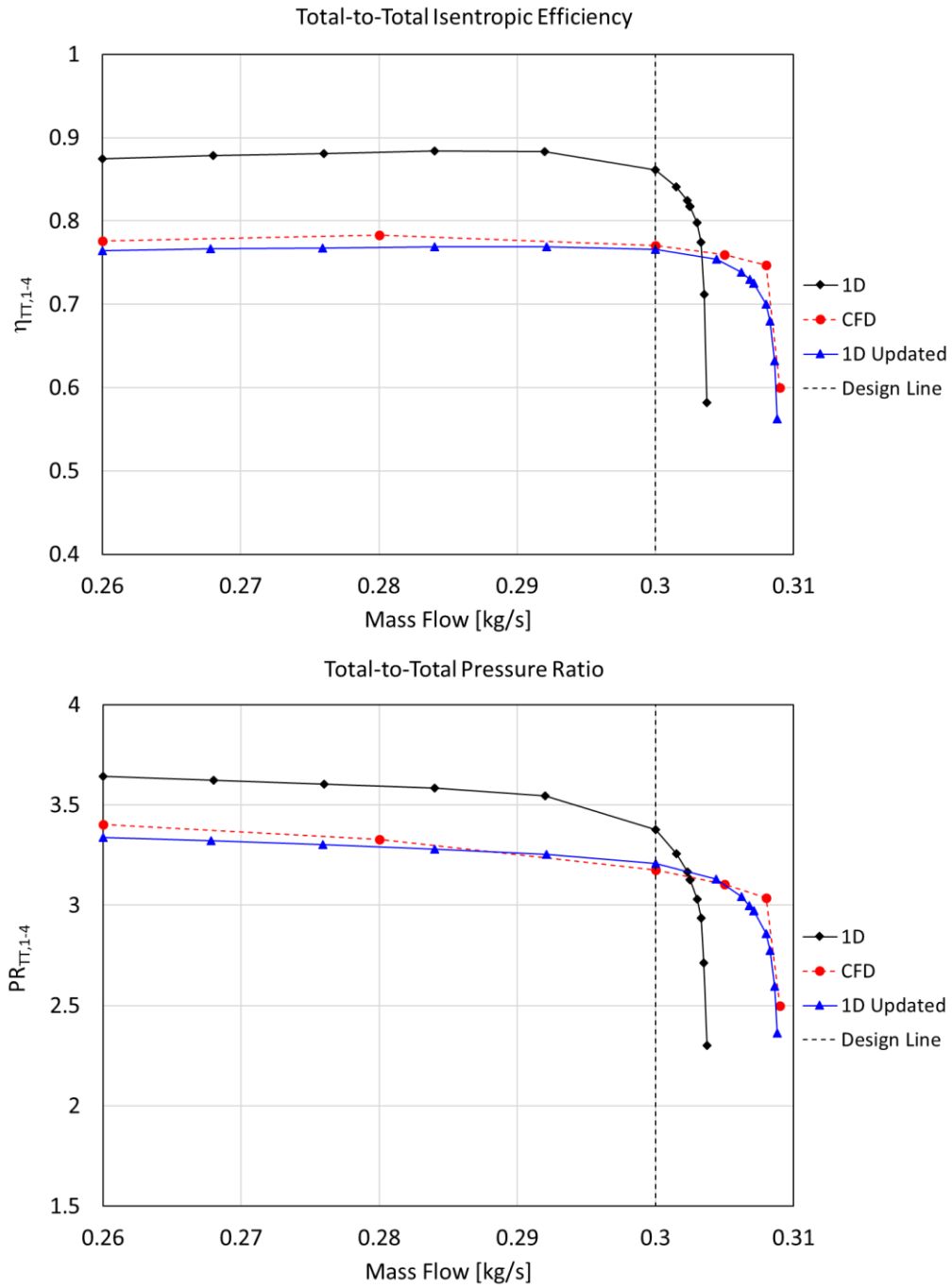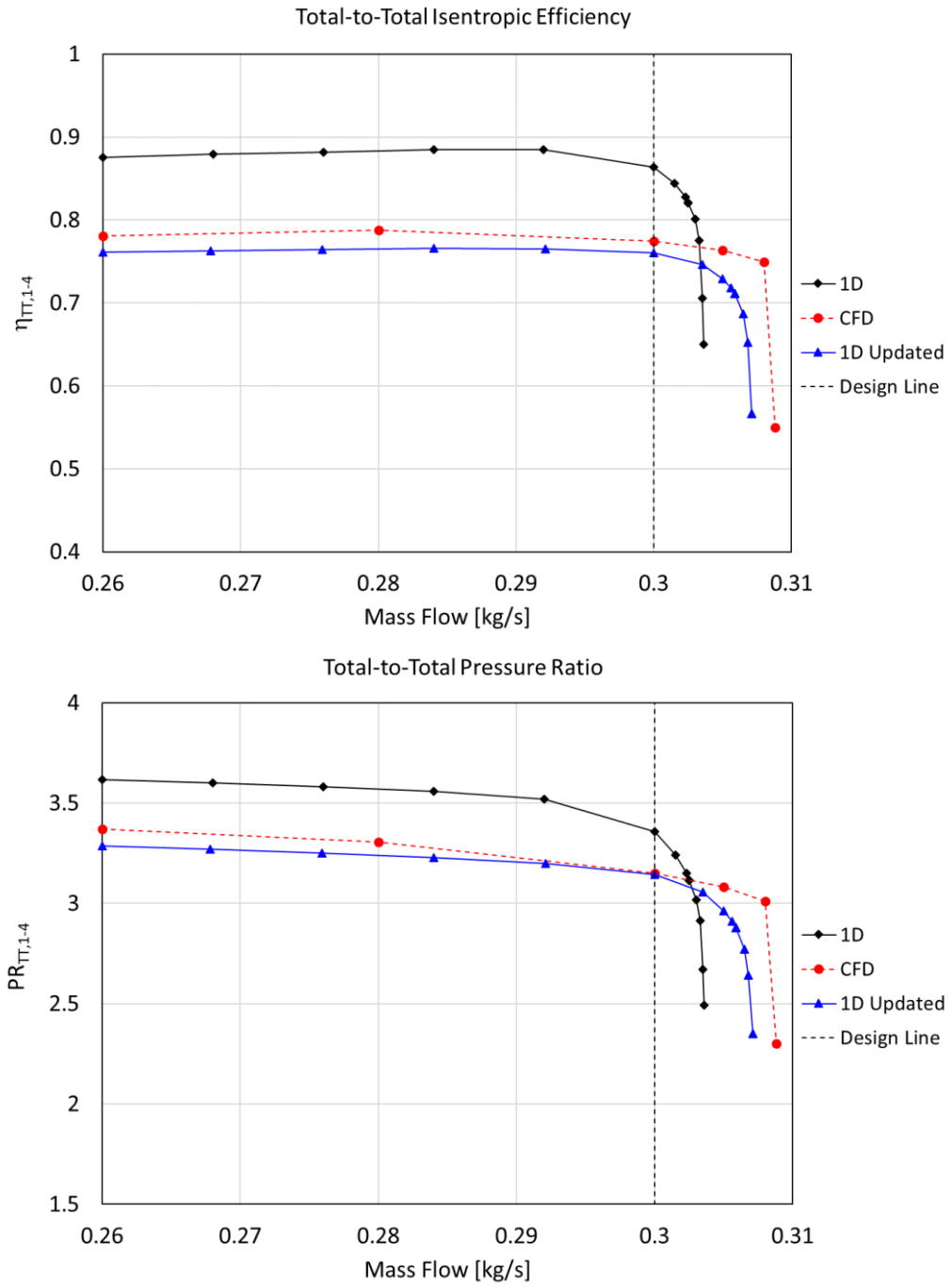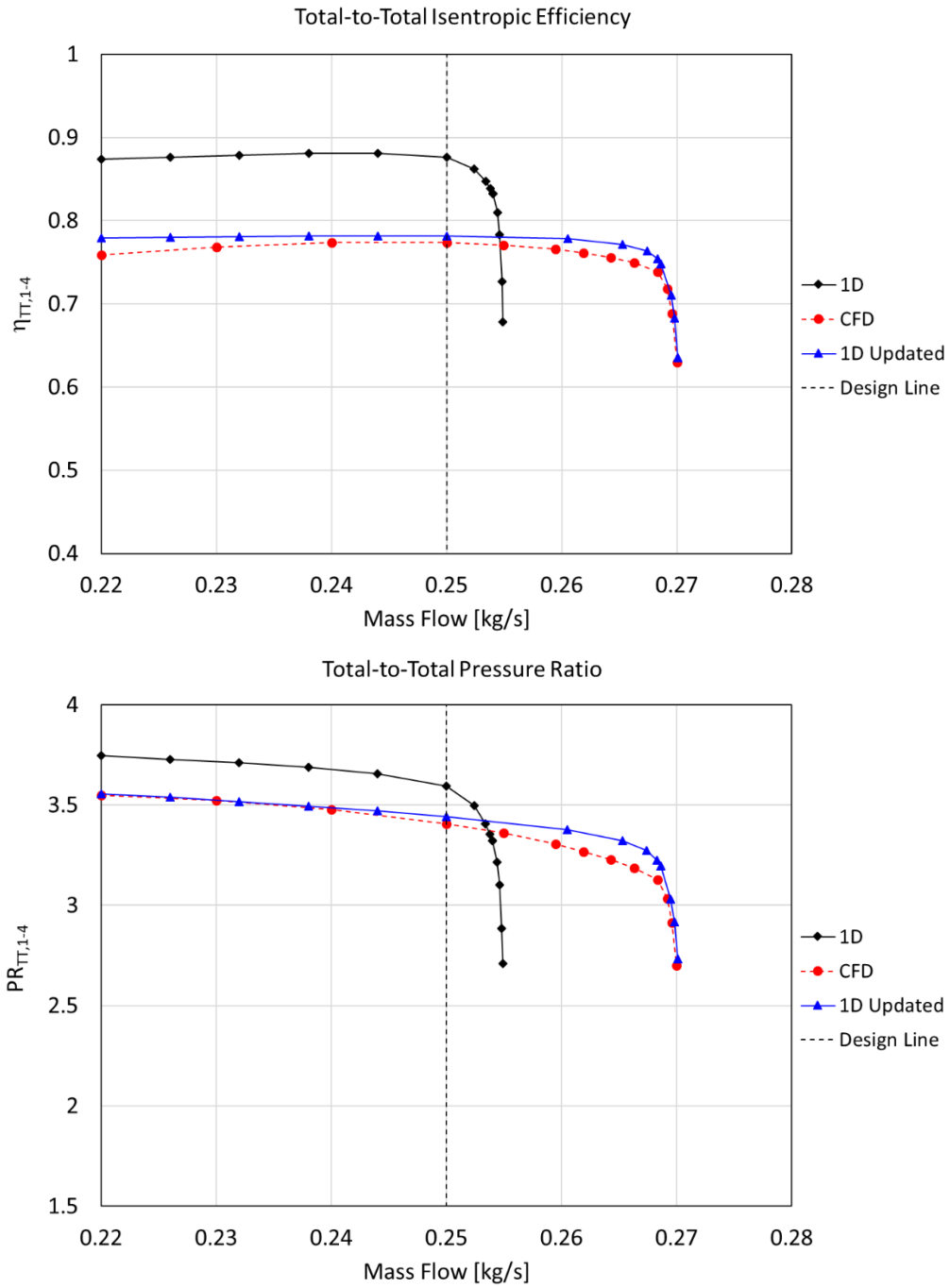
Figure D.2: Compressor 1b Performance Comparison
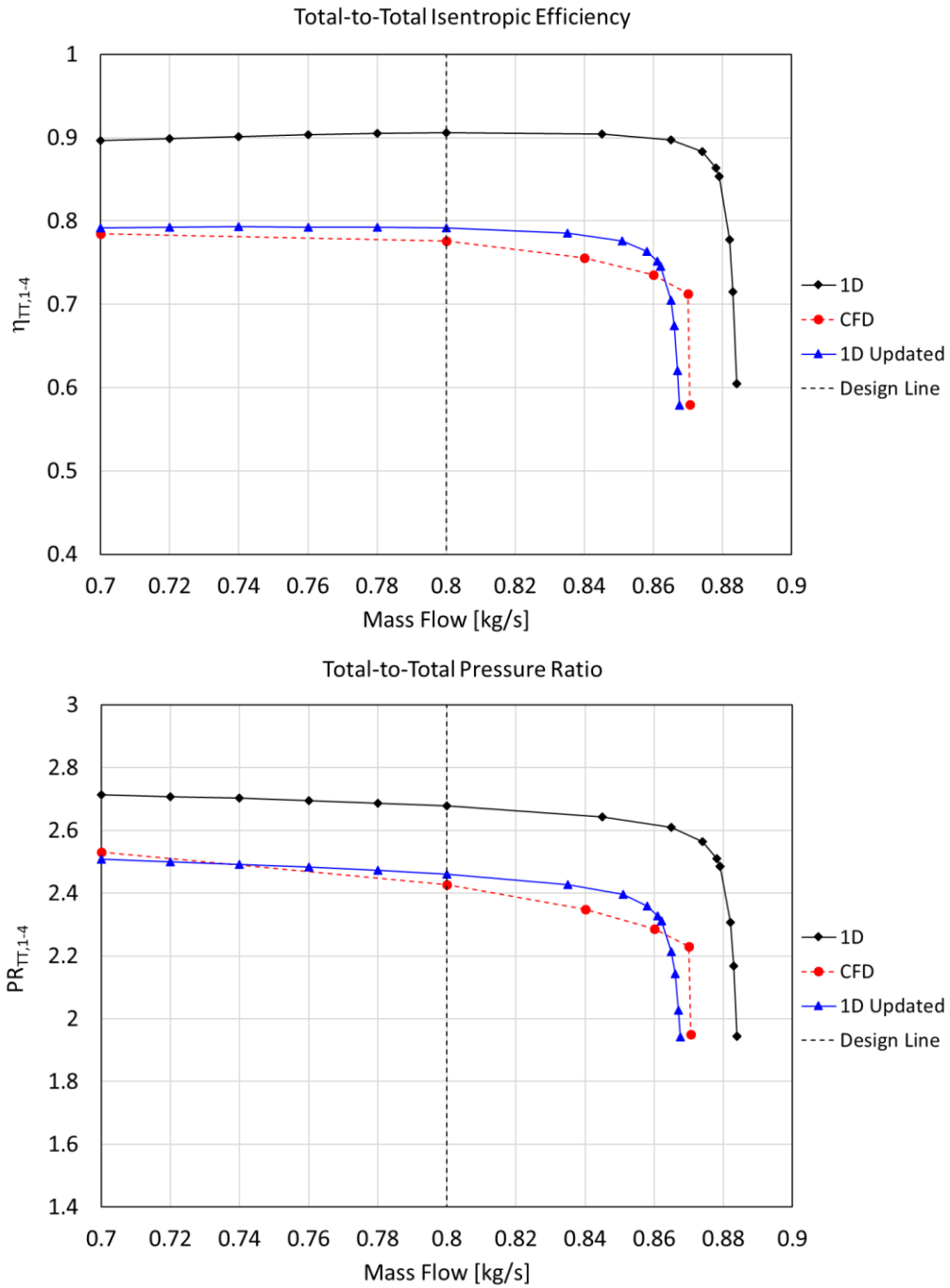
Figure D.3: Compressor 1c Performance Comparison
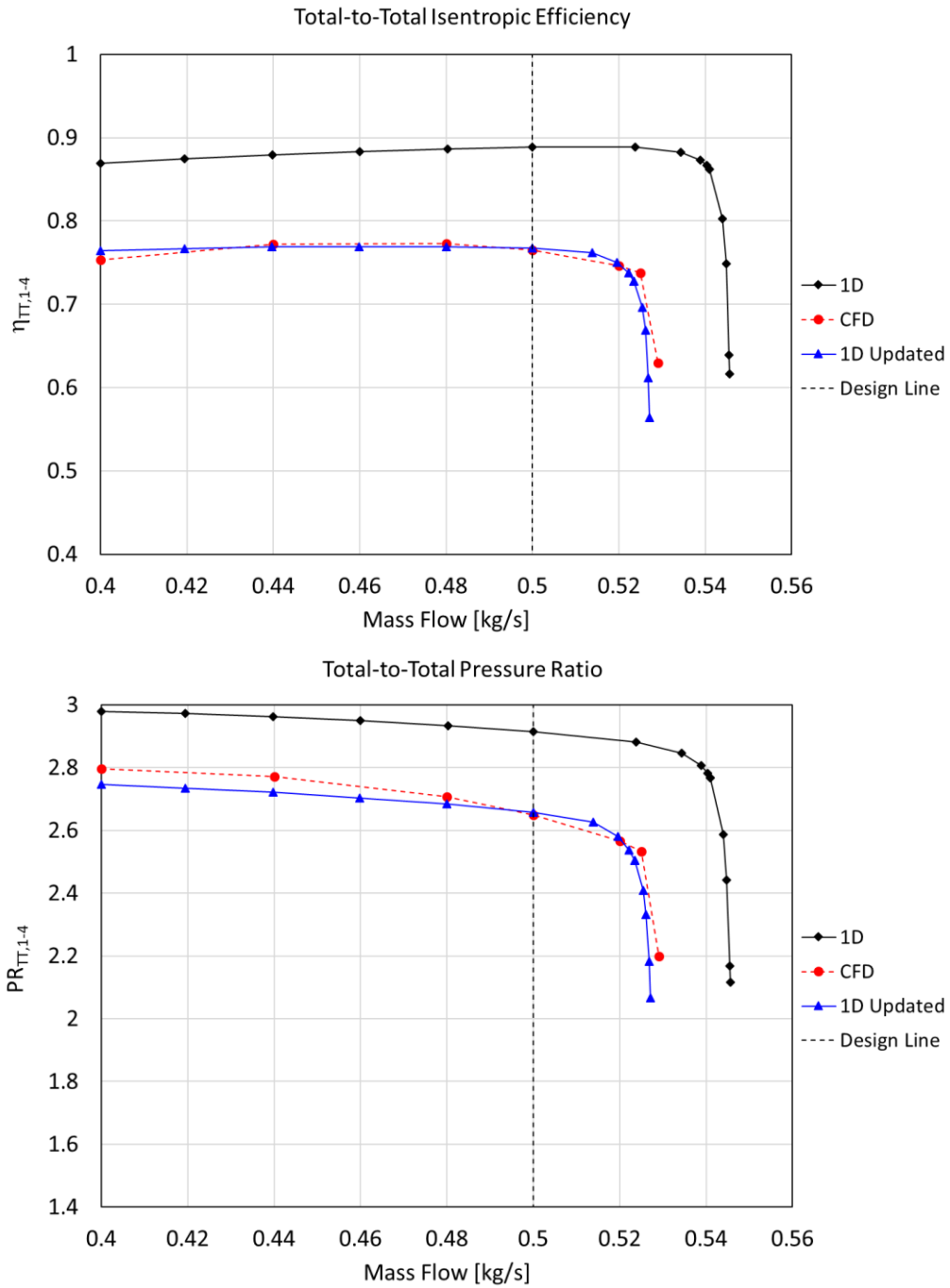
Figure D.4: Compressor 2a Performance Comparison
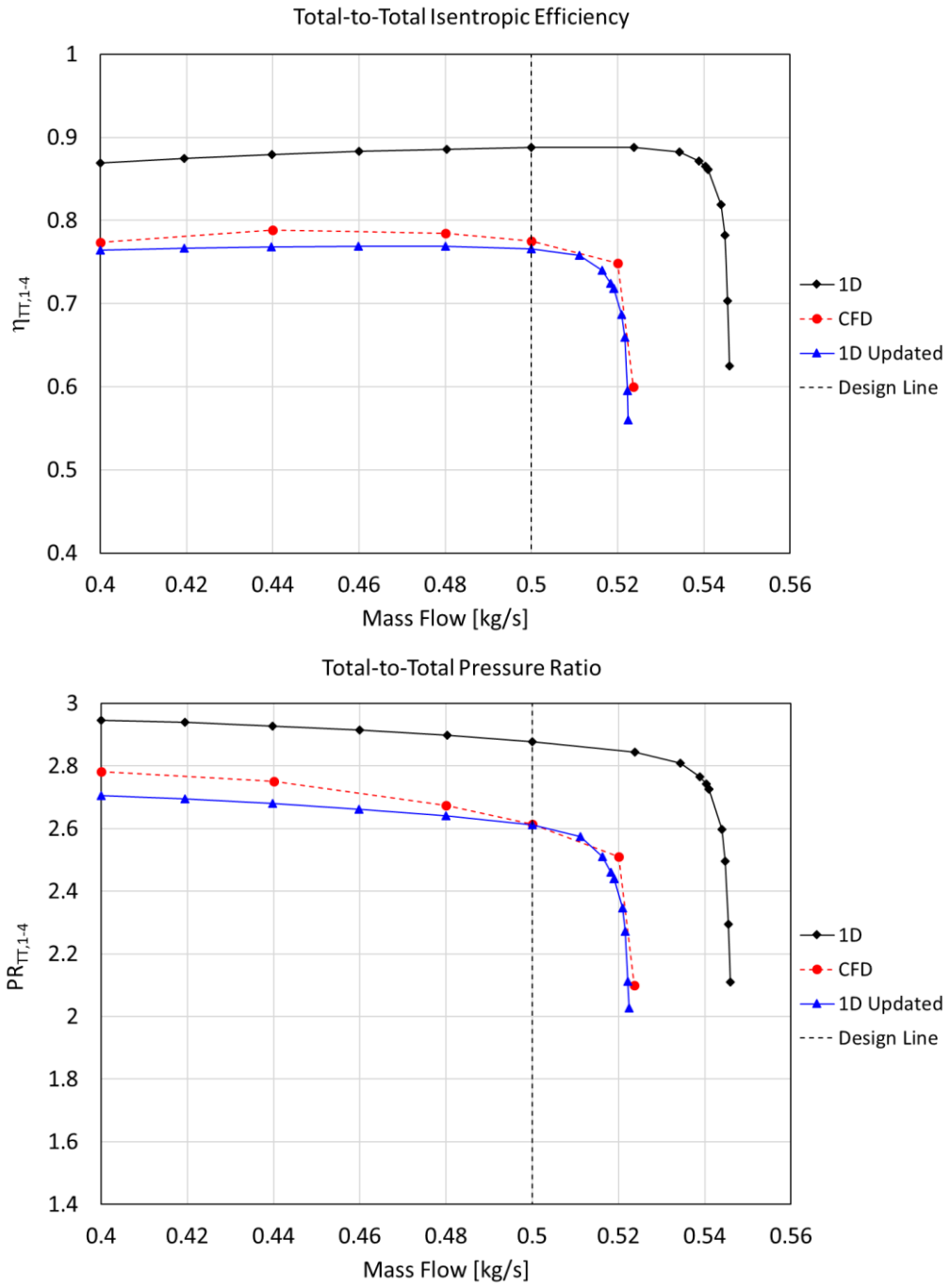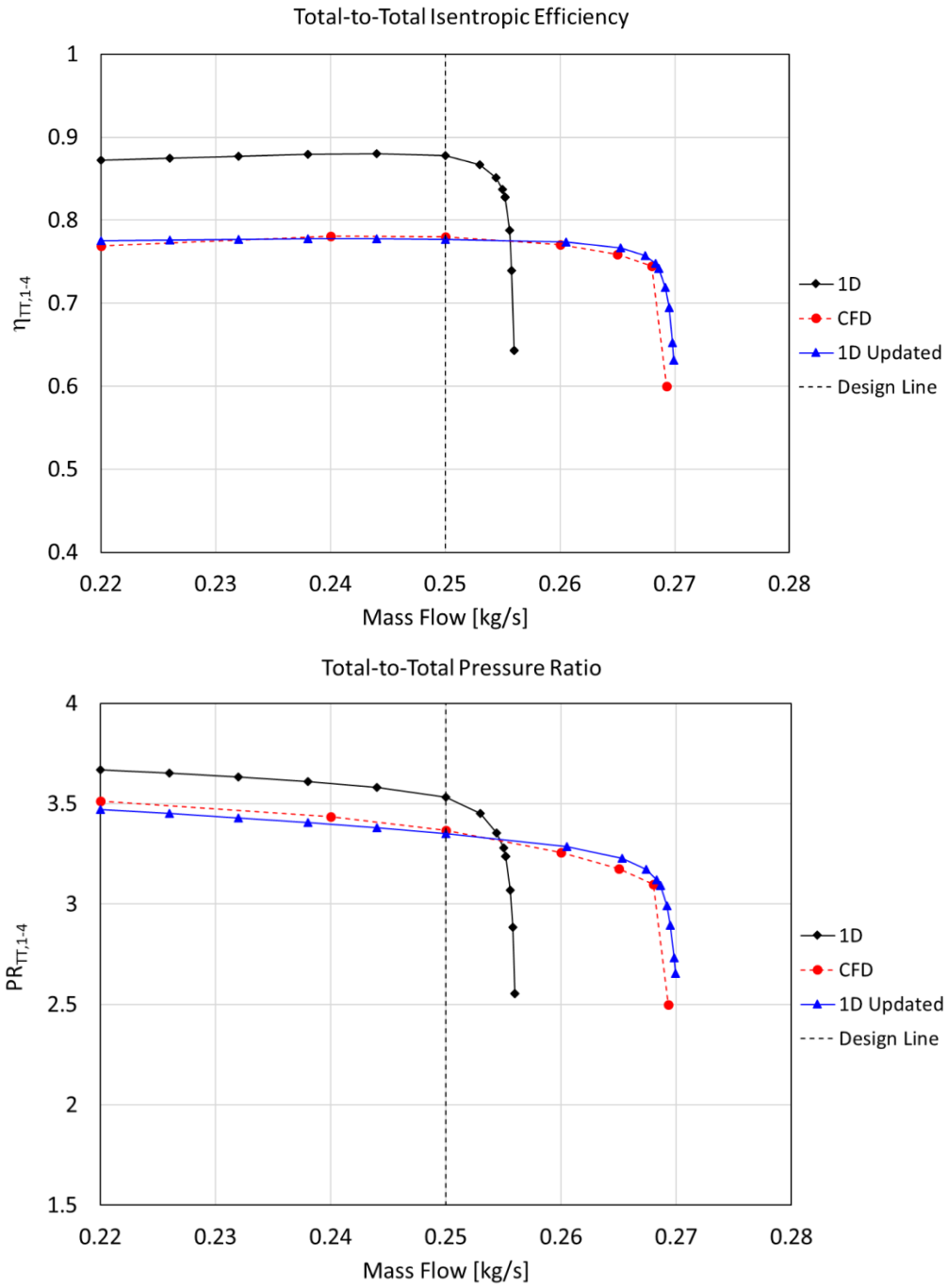
Figure D.5: Compressor 2b Performance Comparison
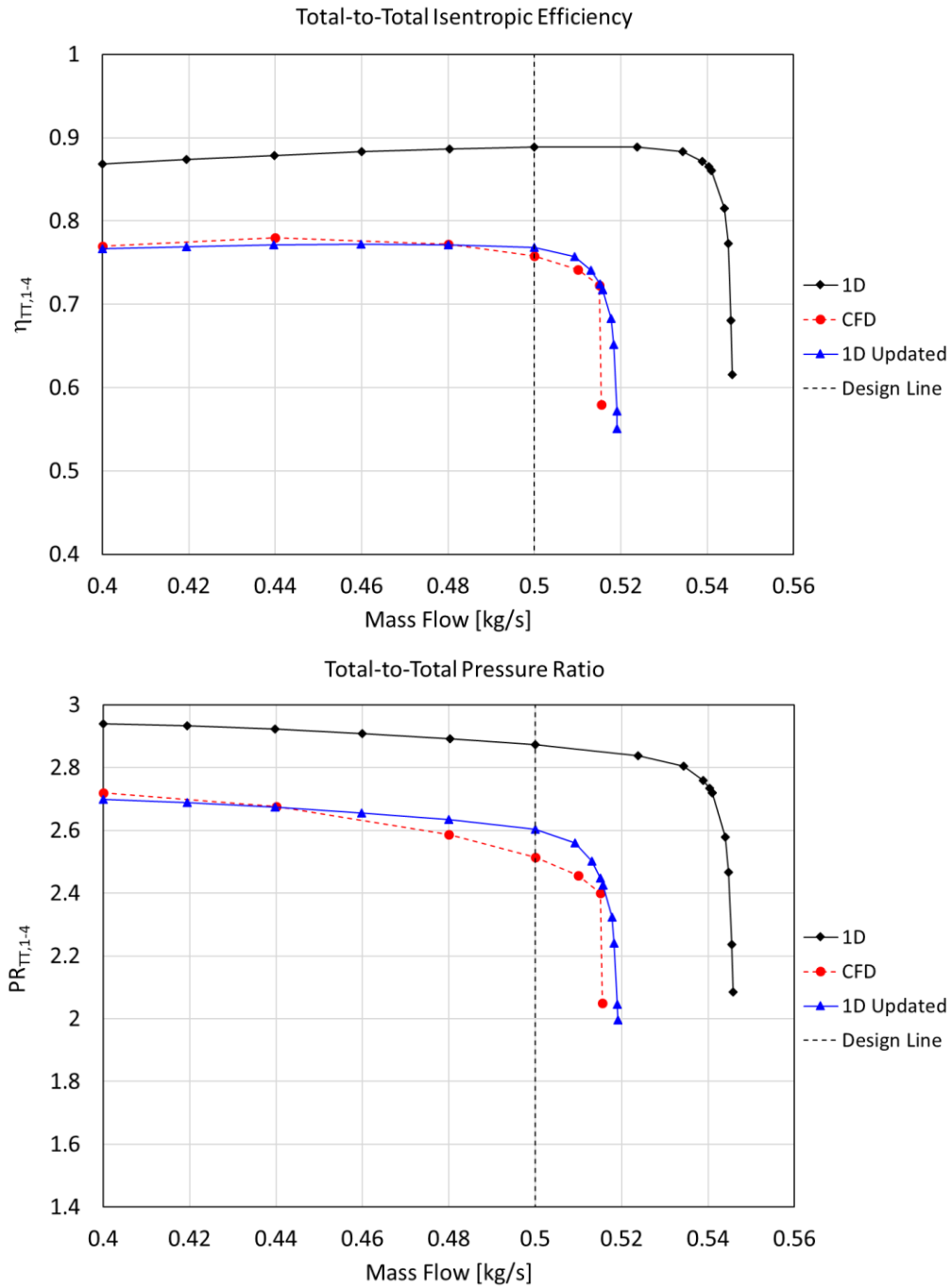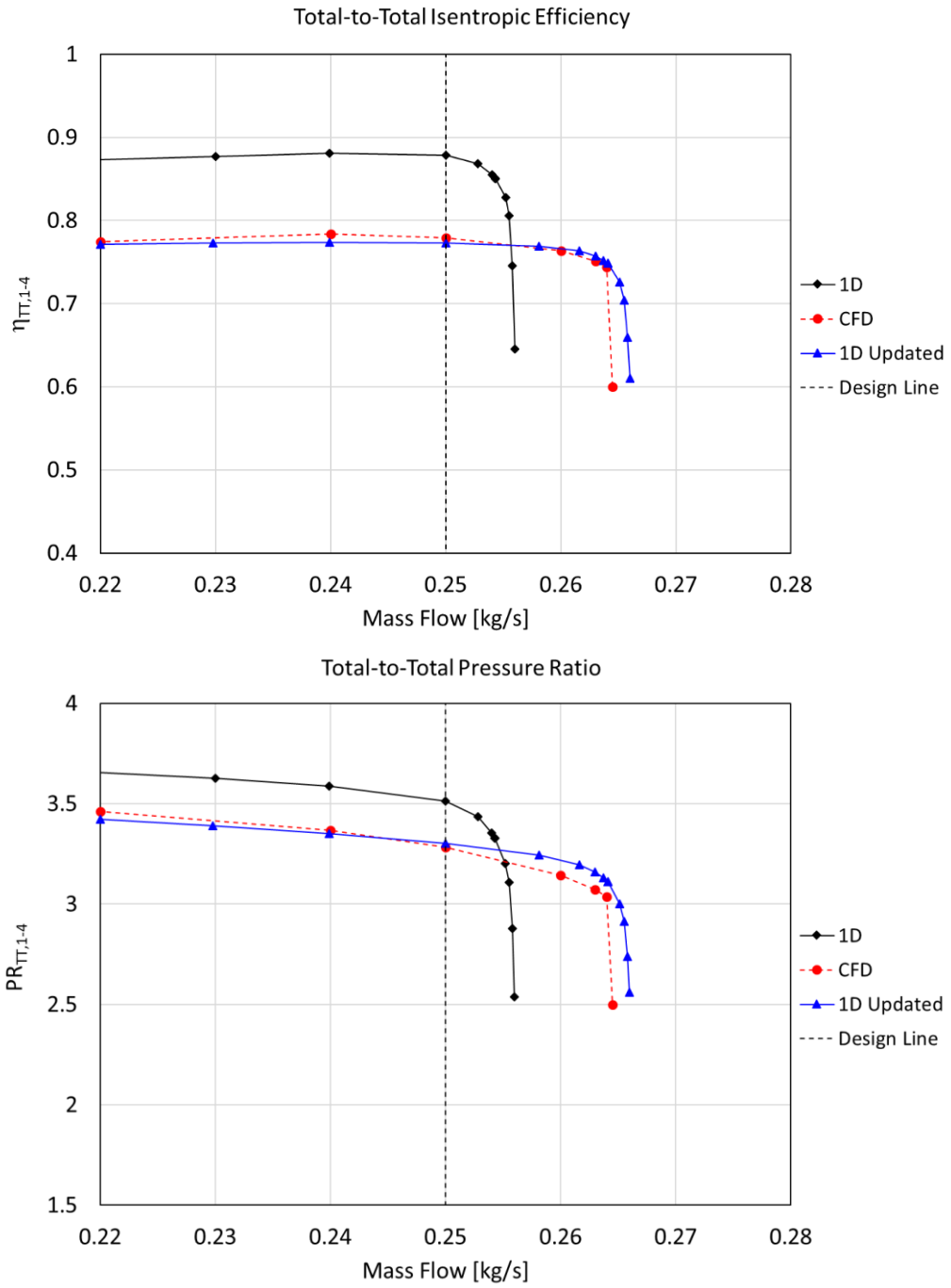
Figure D.6: Compressor 2c Performance Comparison
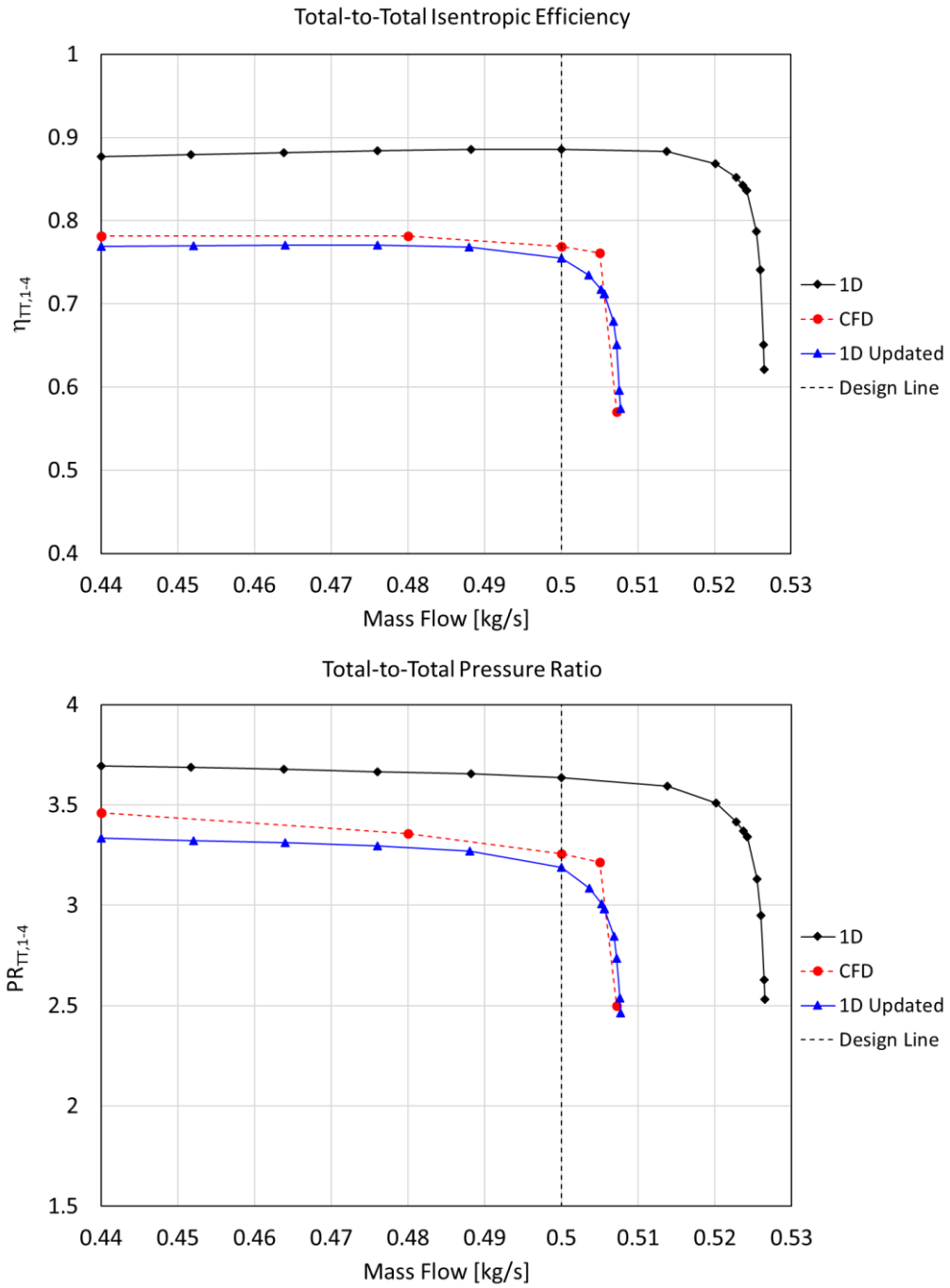
Figure D.7: Compressor 3a Performance Comparison
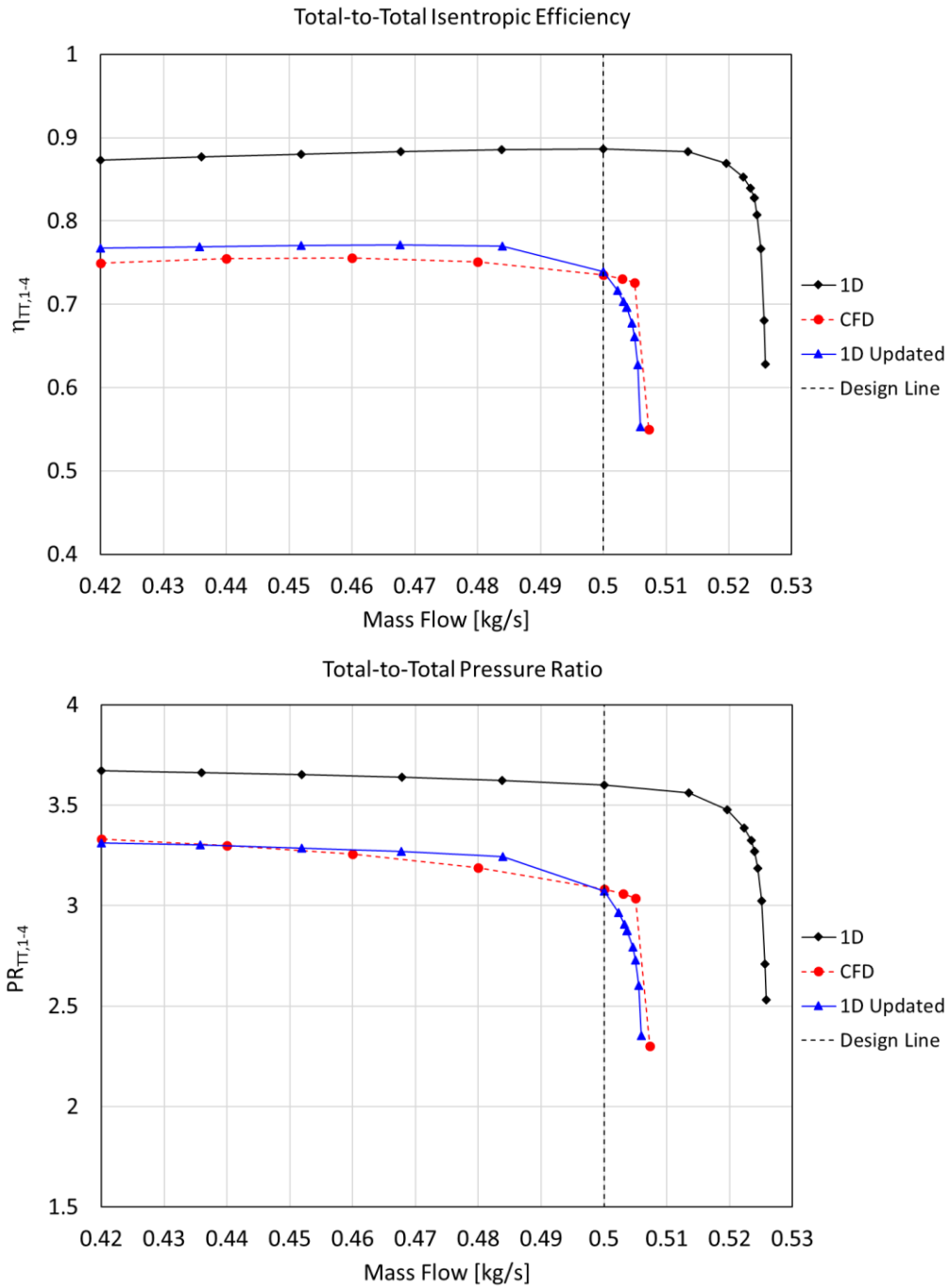
Figure D.8: Compressor 3b Performance Comparison
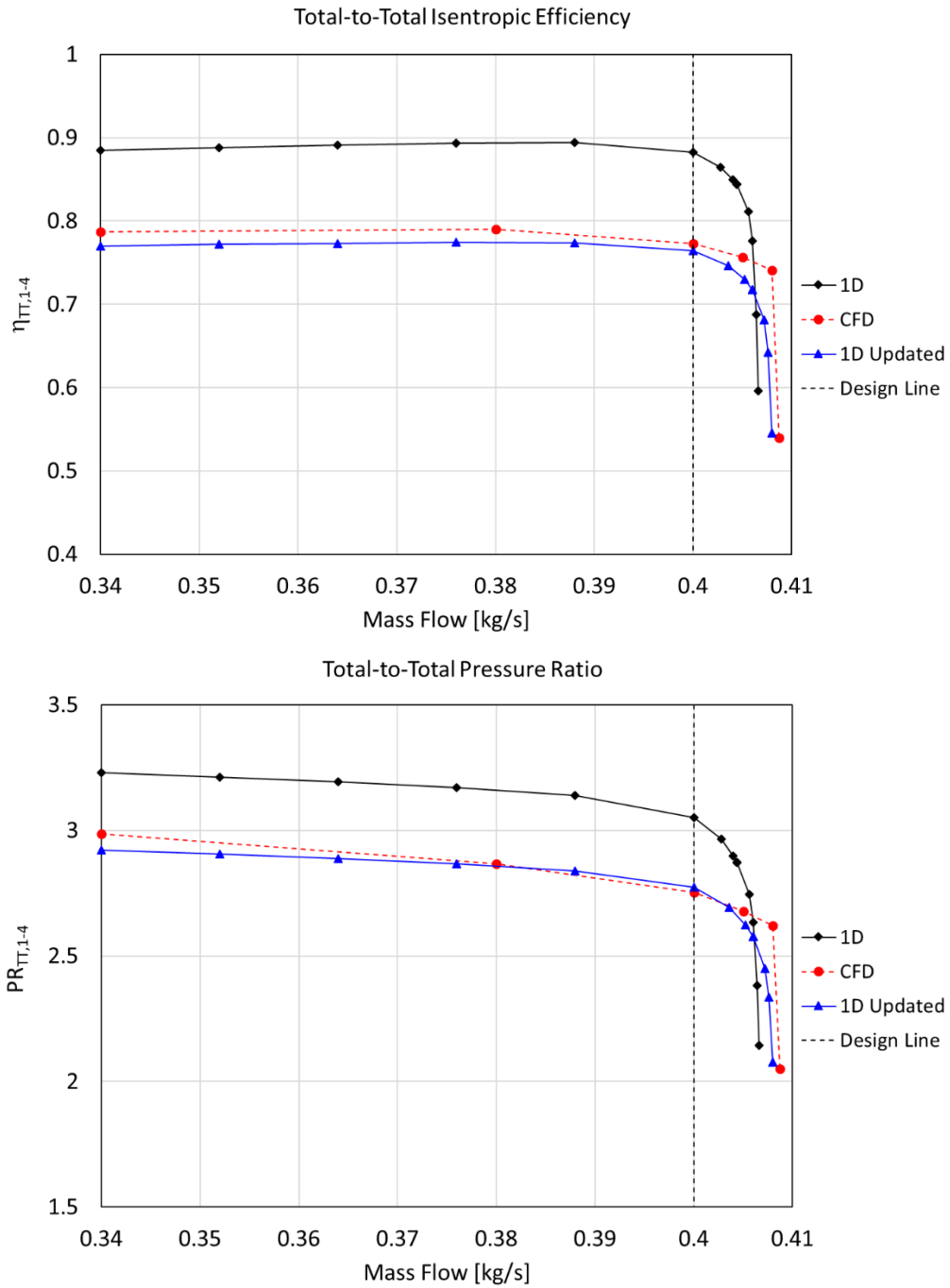
Figure D.9: Compressor 4a Performance Comparison
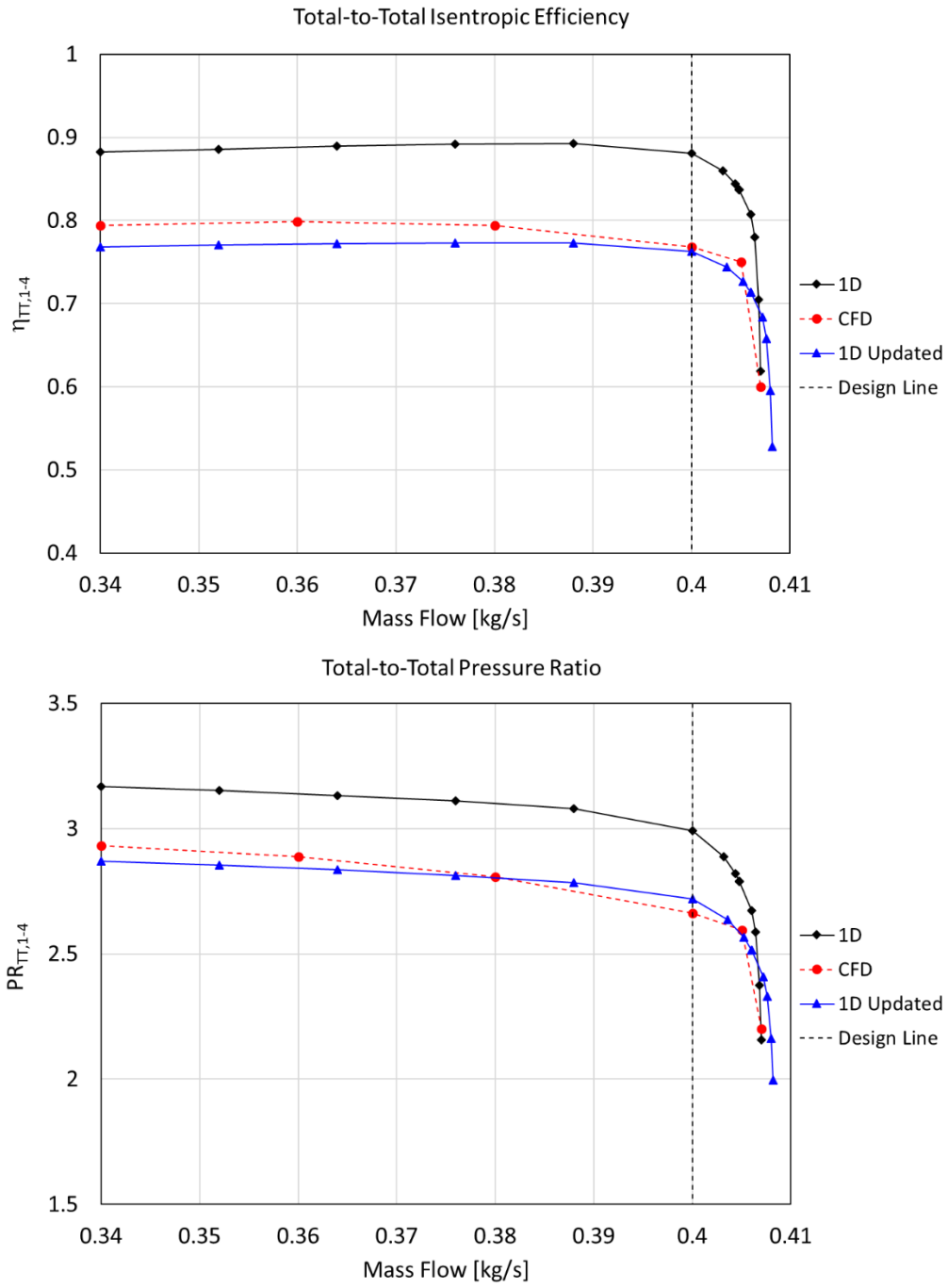
Figure D.10: Compressor 4b Performance Comparison

Figure D.11: Compressor 4c Performance Comparison

Figure D.12: Compressor 5a Performance Comparison

Figure D.13: Compressor 5b Performance Comparison

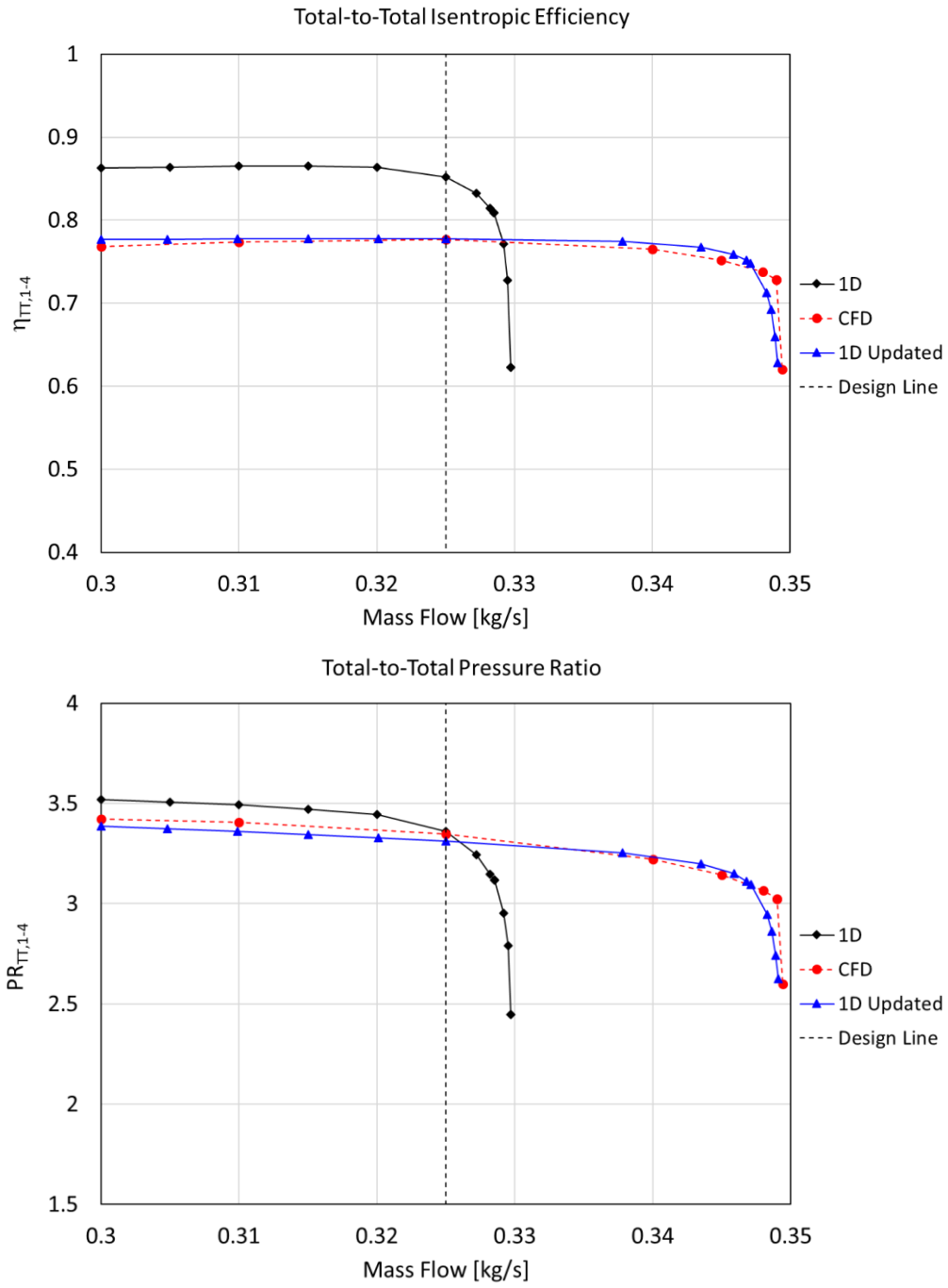Figure D.14: Compressor 5c Performance Comparison

Figure D.15: Compressor 6a Performance Comparison

Figure D.16: Compressor 6b Performance Comparison

Figure D.17: Compressor 6c Performance Comparison

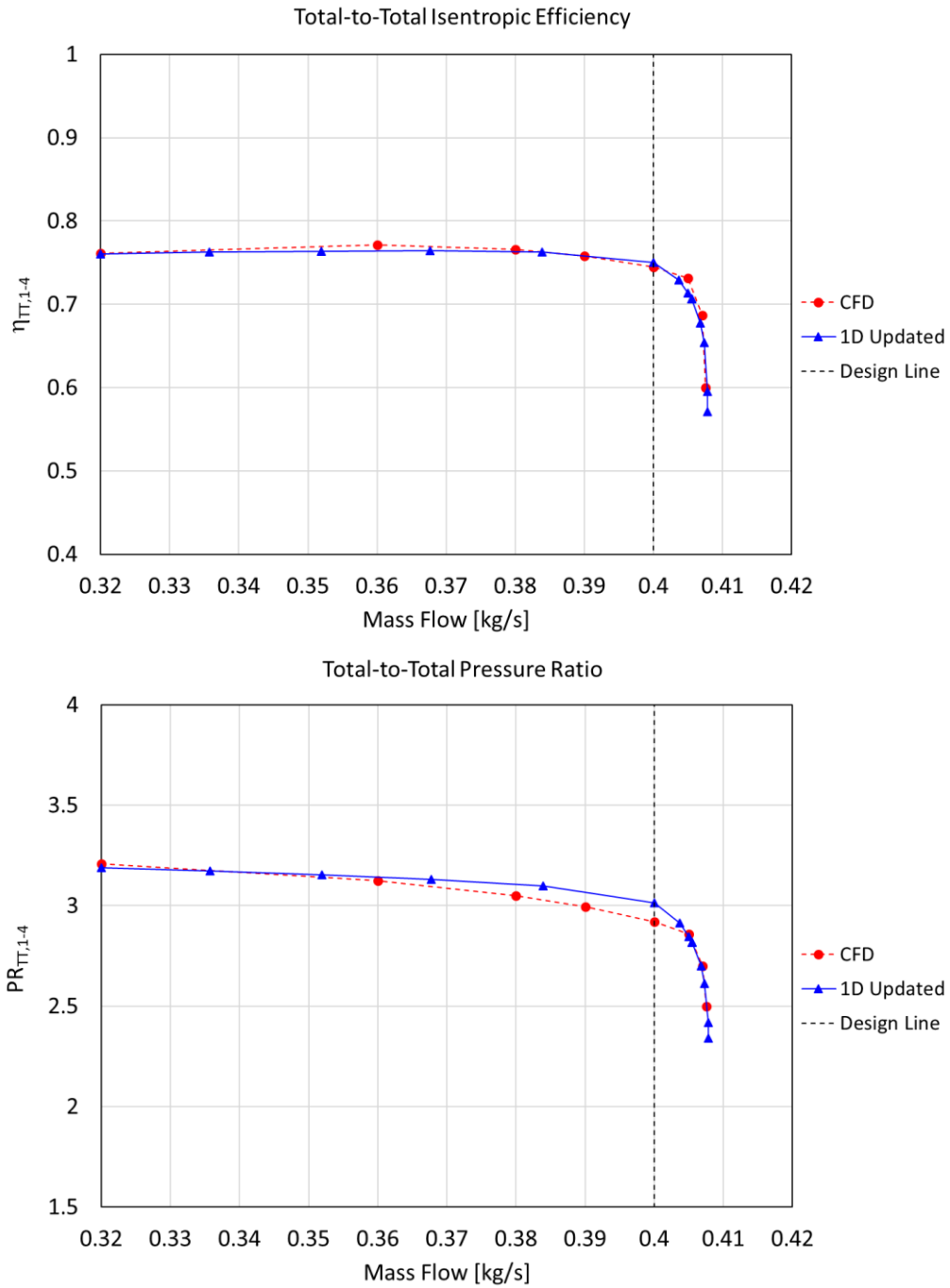Figure D.18: Compressor 7 Performance Comparison
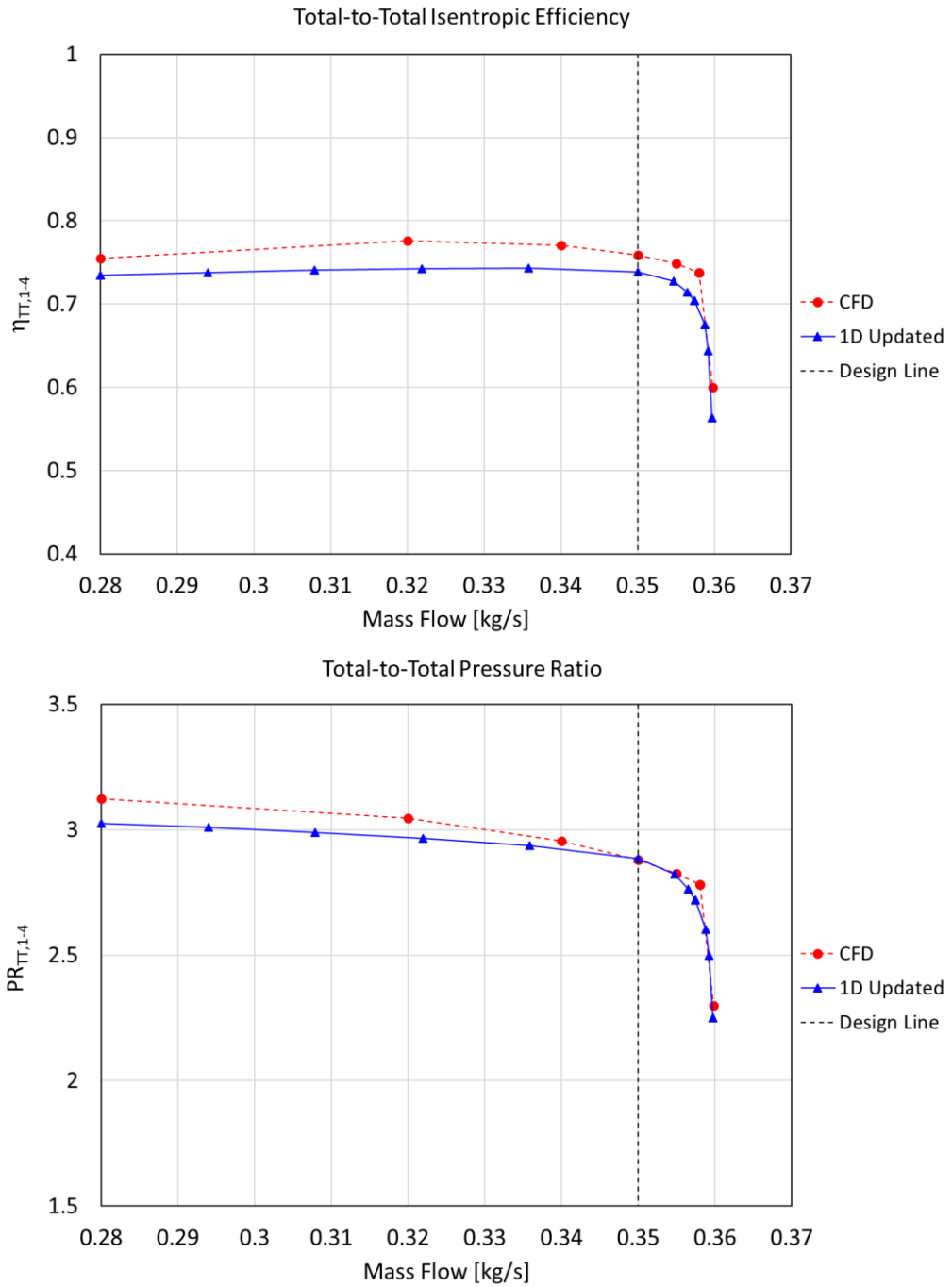
Figure D.19: Compressor 8 Performance Comparison

Figure D.20: Compressor 9 Performance Comparison